NOVEL SYNTHESIS TECHNIQUE TO CONTROL DEFECTS IN TiO2 NANORODS: ROLE OF DEFECTS ON VISIBLE LUMINESCENCE AND LIGHT HARVESTING APPLICATION

A thesis submitted towards partial fulfilment of the requirements for the degree of

Master of Technology in Nano Science & Technology

Submitted by

MONIKUNTALA BHATTACHARYA
EXAMINATION ROLL NO: M4NST19021
CLASS ROLL NO.: 001730701021

Under the guidance of

DR. CHANDAN KR. GHOSH

School of Materials Science & Nanotechnology
Jadavpur University
Course affiliated to
Faculty of Engineering and Technology
Jadavpur University
Kolkata-700032
India
2019

M.Tech. in Nano Science & Technology
Course affiliated to
Faculty of Engineering and Technology
Jadavpur University
Kolkata, India

CERTIFICATE OF RECOMMENDATION

*This is to certify that the thesis entitled “**Novel Synthesis Technique To Control Defects In TiO2 Nanorods: Role Of Defects On Visible Luminescence And Light Harvesting Application**” is a bonafide work carried out by* ***Monikuntala Bhattacharya*** *under my supervision and guidance for partial fulfilment of the requirement of* ***Master of Technology in Nano Science & Technology*** *in* ***School of Materials Science & Nanotechnology****, during the academic session* ***2017-2019****.*

DR. CHANDAN KUMAR GHOSH
Thesis Advisor,
Assistant Professor,
School of Materials Science &
Nanotechnology,
Jadavpur university,
Kolkata-700 032

DR. CHANDAN KUMAR GHOSH
Director,
School of Materials Science &
Nanotechnology,
Jadavpur university, Kolkata-700
032

DEAN -FISLM
Jadavpur
University,
Kolkata-700 032

M.Tech. in Nano Science & Technology
Course affiliated to
Faculty of Engineering and Technology
Jadavpur University
Kolkata, India

CERTIFICATE OF APPROVAL

This foregoing thesis is hereby approved as a credible study of an engineering subject carried out and presented in a manner satisfactorily to warranty its acceptance as a prerequisite to the degree for which it has been submitted. It is understood that by this approval the undersigned do not endorse or approve any statement made or opinion expressed or conclusion drawn therein but approve the thesis only for purpose for which it has been submitted.

Committee of final examination for evaluation of Thesis

1. ---
2. ---
3. --
4. --

DECLARATION OF ORIGINALITY AND COMPLIANCE OF ACADEMIC ETHICS

I hereby declare that this thesis contains literature survey and original research work by the undersigned candidate, as part of his ***Master of Technology in Nano Science & Technology*** *studies during academic session 2017-2019.*

All information in this document has been obtained and presented in accordance with academic rules and ethical conduct.

I also declare that, as required by this rules and conduct, I have fully cited and referred all material and results that are not original to this work.

NAME: MONIKUNTALA BHATTACHARYA

EXAMINATION ROLL NUMBER:
M4NST19021
CLASS ROLL NUMBER:
001730701021

THESIS TITLE: Novel Synthesis Technique to Control Defects in TiO2 Nanorods: Role of Defects on Visible Luminescence and Light Harvesting Application

SIGNATURE: ***DATE:***

Dedicated

To

My Parents

ACKNOWLEDGEMENT

The completion of any work successfully is not the credit of the sole person doing it. It requires the collective effort of a group people related to the work. In this regard, for the successful completion of my thesis work, I would like to thank the following persons.

First of all, I would like to express my sincere gratitude to my thesis supervisor Dr. Chandan Kr. Ghosh, Director, School of Materials Science & Nanotechnology, Jadavpur University, Kolkata for his constant academic and moral support, guidance and ideas without which completion of this thesis would have been impossible. His motivations and academic lessons have helped me to think dynamically about the project and has helped me to complete the project successfully.

I wish to express my heartiest gratitude to Dr. K.K. Chattopadhyay, Professor Department of physics, Jadavpur University, Kolkata for his constant support and encouragement which was indispensible for the project.

I would like to thank all the faculty members of School of Materials Science & Nanotechnology, Jadavpur University, Kolkata, for giving me academic guidance throughout my M.Tech course in different subjects, the cumulative knowledge of which has helped me to complete the thesis work more effectively.

I give my heartiest thanks to Dr. Jiten Ghosh, Senior Scientist, Central Glass and Ceramic Research Institute, Kolkata, Prof. Sujoy Baitalik and Sourav Deb, Department of Chemistry, Jadavpur University for letting me access special characterization instruments specific to my project.

Next, I wish to express my sincere thanks to Soumik Poddar and all other members of Nanoscience Lab, School of Materials Science & Nanotechnology, for their timely support and guidance without which I could not have successfully completed the thesis.

Next, I express my thanks to Mr. Pankaj Kr. Bhadra, Mr. Subhasis Dey, Mr. Sudhir Ghosh, Souvik Bhattacharya, Biswajit Das, Rituparna Chatterjee and Karamjyoti Panigrahi for carrying out the general characterization of my sample that led to the timely completion of my thesis.

Most importantly I would like to extend my sincere thanks to Sayan Dey, VLSI Lab, Department of Electronics and Electrical Communication Engineering, IIT-Kharagpur for his guidance and constant support.

Lastly, I would like to extend my thanks to all of my friends for their moral supports.

CONTENTS

Measurement of Photodiode Characteristics of TiO2-pSi Hetero Junction Fabricated on P-Si Substrate

LIST OF FIGURES

LIST OF TABLES

ABSTRACT

In this thesis, a defect induced low temperature novel synthesis procedure of titanium (II) oxide was designed. The synthesis temperature was kept constant at 180^{o}C and precursor NaCl concentration is varied from 0M to 5M to obtain hierarchical microstructure. Defect related studies such as UV-Visible Spectroscopy, PL Spectroscopy, Raman Spectroscopy, TCSPC Analysis for life time measurement has been carried out meticulously. Effect of defect on lattice parameter has been studied precisely using Rietveld refinement technique. In order to understand its practical implementation photodiode has been fabricated and the correlation between defect analysis with photodiode activity has been tried to established, which is one of its kinds. It has been found out that with increase in NaCl concentration defect level increases up to a certain extent and then started dropping. This phenomenon has not been reported earlier. Also, the effect of presence of defect structure onto the photodiode has been established and a remarkable variation in sensitivity, responsivity and diode current has been obtained. Increase in defect concentration showed enhancement of various electrical parameters obtained from photodiode characteristics. Sample with maximum defect showed almost doubling of current gain in photodiode, which is a very positive sign in terms of practical applications. From the analysis, it can be expected that, the material may be considered as a suitable material for application in the electronic field for next generation device fabrication in the field of sensor as well as energy harvester which is, at present, a major global demand.

CHAPTER 1

INTRODUCTION

1.1 INTRODUCTION TO NANOTECHNOLOGY

1.1.1 NANOTECHNOLOGY: A PREAMBLE

Nanotechnology refers to the study of the “small”, the prefix “nano” being derived from the Greek word meaning “dwarf”. It may be considered as the engineering of some functional systems at the molecular scale. As the size of any material is reduced, some peculiar change in its physical or chemical properties is observed. This change may be in terms of strength, fracture toughness, melting point, color, electrical conductivity, magnetic nature etc. In most cases, the efficiency of the properties is enhanced in the nano level when compared to the materials in bulk. It is observed that these changes bring about some spectacular new applications of the materials which are otherwise unknown when the material is in bulk state. Moreover, their efficiency in some already known application may increase at an alarming rate in nano dimensions when compared to the bulk systems. Thus, nanoscience and technology or simply nanotechnology may be described as the science that explains some abnormal variation of some already known properties for a material when its volume is reduced to an aggregation of a few atoms that opens newer dimensions of application for the material. For example, gold in its bulk state is non- reactive and so it is called noble metal. However, in the nano level, it is an excellent catalyst. Its color in the bulk state is yellow. When reduced to the nano level, its color varies from violet to red depending on the size of the nanoparticle present in the suspension. In the nano level, gold is an excellent drug carrier and it is often used as a drug delivery system in target cell treatment techniques.

(a) (b)

Figure 1.1: (a) Bulk gold (b) Gold nanoparticles of varying size

Thus, a change in size drastically increases the application efficiency of a material and hence nanotechnology opens a new dimension in the field of science and technology. Dimensionally, it deals with materials ranging size of 1 to 100 nm. This field promises to present the world and mankind with an entirely new dimension of science and technology by which many newer concepts can be realized which otherwise cannot be achieved in the bulk state. Thus, the science Nano domain is a mysterious world, where our ability of expectation faces actual challenge as in the nano regime a common material can have very uncommon property.

1.1.2 WHAT IS NANOTECHNOLOGY?

The Royal Society presented a wide description of Nanotechnology as: “Nano science is the study of phenomena and manipulation of materials, atomic, molecular and macromolecular state where properties differ significantly from those at a large scale.”[1] Nanostructures may be compared to a human hair which is ~50,000 nm thick whereas the diameters of nanostructures are ~0.3 nm for a water molecule, 1.2 nm for a single-wall carbon nano tube, and 20 nm for a small transistor. DNA molecules are 2.5 nm wide, proteins about 10 nm, and an ATPase biochemical motor about 10 nm. The word Nanoscience refers to the study, manipulation and engineering of matter, particles and structures on the nanometer scale (one millionth of a millimeter, the scale of atoms and molecules). Important properties of materials, such as the electrical, optical, thermal and mechanical properties, are determined by the way molecules and atoms assemble on the nanoscale into larger structures. Moreover, in nanometer size structures these properties are often different from on macro scale, because quantum mechanical effects become important.

Nanotechnology is the application of nanoscience leading to the use of new nanomaterials and nano size components in useful products. Nanotechnology will eventually provide us with the ability to design custom-made materials and products with new enhanced properties, new nano electronics components, new types of “smart” medicines and sensors, and even interfaces between electronics and biological systems.

A huge variety of approaches are available for synthesizing nanostructures. In the *top-down* techniques bulk material is chiseled out of or added to surfaces. Microchips or better nano chips with line widths of about 30 nm at present are the most notable examples. In contrast, *bottom-up* manufacturers“ use self-assembly processes[2] to put together larger structures – atoms or molecules or clusters of many atoms – that make ordered arrangements spontaneously.

1.1.3 HISTORY OF NANOTECHNOLOGY

The investigation of nanostructures and the development of nanoscience started around 1980 when the scanning tunneling microscope (STM) was invented[3] and the concept of nanostructured solids was suggested[4]. More than 60 years earlier R. Feynman had emphasized that “. . . there is plenty of room at the bottom . . . in the science of ultra-small structures”[5] (Fig. 1.1.a). Clearly, nanostructures were available much earlier. Albert Einstein calculated in his doctoral dissertation from the experimental diffusion data of sugar in water the size of a single sugar molecule to about 1 nm[6]. Michael Faraday remarked during a lecture on the optical properties of gold in 1857 that ". . . a mere variation in the size of the (nano) particles gave rise to a variety of resultant colors"[7]. In fact, nanostructures already existed in the early solar nebula or in the pre solar dust (4.5 billion years ago) as deduced from the detection of nanosized C60 molecules in the Allende meteorite[8]. From its early infancy the field of nanoscience has more and more grown up (Fig. 1.1.b) and enjoys worldwide scientific popularity and importance. For the characterization of this research field the notations "Nanostructured Science" or "Nanotechnology" were coined by K.E. Drexler[9]. A huge variety of approaches are available for synthesizing nanostructures. In the top-down techniques bulk material is chiseled out of or added to surfaces. Microchips or better nano chips with line widths of about 30 nm at present are the most notable examples.

In contrast, bottom-up manufacturers use self-assembly processes[10] to put together larger structures – atoms or molecules or clusters of many atoms – that make ordered arrangements spontaneously. Novel properties are inherent to nanosized systems due to a reduction in dimensionality, or when the size of nanoparticles decreases below intrinsic length scale.

Fig. 1.2 (a) R. Feynman at an American Physical Society meeting at Caltech on December 29, 1959 (b) Small things are absolutely fascinating, nano DNA robot a visionary dream.[courtesy http://www.infoniac.com]

The novel properties may be of three broad types; incremental, evolutionary or revolutionary.

- **Incremental:**

Where certain property of a material (may be physical or chemical) is enhanced in the nano regime for example, photo catalytic activity of ZnO nanoparticles is more than to bulk[11].

- **Evolutionary:**

Where it is possible to bring or rather tune a particular property by pre-determined logics for example, magnetic property tuning by noble metal attachment[12]

- **Revolutionary:**

Something that is unexpected cannot be predicted and brings up a new area of research; for example, exchange bias phenomenon[13].

1.1.4 APPLICATIONS OF NANOTECHNOLOGY

Nanoscience will become the most influential tool for the next epoch of the information age. According to Moore's law number of transistors per chip will be doubled in every 18 months (Fig. 1.2, [14,15]). From the top ten advances in materials science[16] at least five are directly related to nanoscience. Some people think that nanoscience is likely to revolutionize many areas of research activity, such as materials science, information processing, biotechnology, and medicine[17]. In chemistry nanotechnology tools such as scanning tunneling microscopy (STM) enable the study and manipulation of chemical reactions on the atomic scale, nano catalytic processes can be initiated, and the bottom-up synthesis of organic as well as inorganic supramolecular structures for, e.g., molecular devices is revitalized. In medical applications nanosized particles will play a role in diagnosis, therapy, and drug delivery. Food products from milk, cereals, or meat are based on colloidal, i.e., nanoscopic structures such as gels, emulsions, foams, or combinations thereof. As an example, electron microscopic techniques are employed in order to study liposomes as a substantial nanoscopic component of food emulsions. Much progress in nanotechnology stems from the emergence of high-resolution scanning probe microscopy tools and their many specific variants. The microscopic tools have led to a new dimension of visual technology by the aid of which even a few aggregations of atoms are clearly visible thereby determining every minute details of the particle so prepared. Thus, today, visualization of the "nano" is physically possible with the aid of the state of art microscopes and hence tailoring of the nanostructures have become easier and hence the effectiveness of the nanostructured materials is on the full bloom.

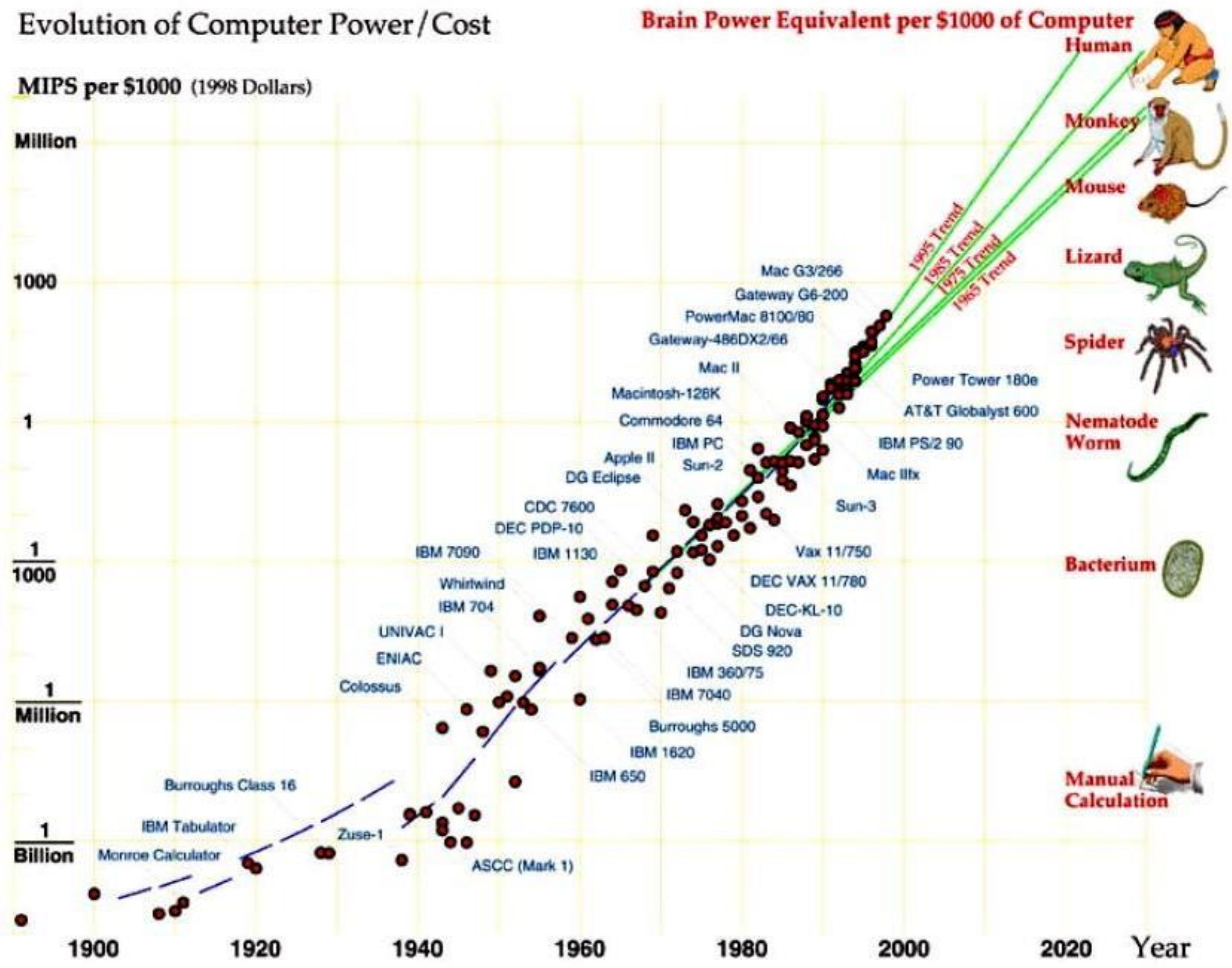

Figure 1.3 Gordon Moore postulated in 1965[13,14] that the computer powers will double every 18–24 months. This prediction is still valid nowadays. (© Courtesy community.emc.com) food emulsions. Much progress in nanotechnology stems from the emergence of high-resolution scanning probe microscopy tools and their many specific variants.

The rapid development of electron microscopy[18] and x-ray microscopy[19] also contributes to the exploration of nanotechnologies. From this brief outline it is evident that nanoscience is a most interdisciplinary approach[20-22] because all disciplines and areas converge at the nanoscale to the same basic principles and the same basic tools so that the frontiers between the disciplines even seem to disappear. It is well recognized that for the exploitation of nanoscience and nanotechnology one must understand the physics and chemistry of the nanoscale and one must learn how to make materials and functional devices[23]. This scenario centers to bring together researchers from many disciplines to provide the tools to do nanoscale research, from work to understand the economical and societal benefits and perils of this new field of development, and finally from work force, education, and training.

1.2 TRANSITION METAL OXIDES (TMO)

Transition metals are those elements in the periodic table that have unfilled d or f orbitals. Due to the presence of these unfilled orbitals, the elements possess unusual properties like luminescence, magnetic, electronic etc. Generally, oxides are gaseous or amorphous materials occurring as one of the most stable compound naturally. However, transition metal oxides are different from the conventional oxides due to their electronic and crystal structure, their bond structures and hence their properties. These materials have certain unusual and useful properties like electronic, magnetic etc.[24-26] These properties strongly depend on material defects like vacancies, dislocations, faults, grain boundaries etc. They possess excellent catalytic, magnetoresistive, photo degradation and antimicrobial activities which are dominant when reduced to nano level.[27-30] The transition metal oxides are also promising thermoelectric materials. Metal oxides show a range of electronic properties ranging from insulating to superconducting[31]. Their electronic properties can be engineered by changing their morphology, doping and stoichiometry. The phonon generation and propagation properties in many transition metal oxides are well defined and molecular engineering methods are developed for tuning them accurately. Moreover, transition metal oxides show a wide range of interesting thermal properties at cryogenic, ambient and high temperatures.[32] Many transition metal oxides offer high Seebeck coefficients, with desired thermal and electrical conductivities and heat capacities, at targeted temperatures which can be utilized for different applications[33-36]. Their abundance in nature is another important advantage for technologies to be widely adopted.[37] The transition metal oxides, when reduced to nano level, show some exceedingly enhanced properties and hence they are of great use in different fields of science and technology. The oxides can be applied to a vast range of fields having a wide range of applications replacing the conventional materials to obtain higher efficiency. For example, the oxide like ZnO, TiO_2 etc. show high antibacterial efficiency and hence is suitable for antibacterial coatings, antimicrobial drugs, coatings for surgical accessories etc. Again, oxides like NiO, CuO, VO_3 etc. show promising electrical storage capacity, magnetic property and electronic properties when reduced to nano regime. In the nano regime, different morphologies or nanostructures like rod like structure, coral, flower, spheres can be prepared. The different properties are found to change with respect to the morphologies generated. Thus, enhancement of the properties by tuning the morphology of the nanostructure is also possible. By tuning the morphology, the crystal structure of the material can also be tuned from simple cubic to inverse spinel based on the type and size of the defects formed due to the change in the morphology of the nanomaterials.

Thus, the variation and control of the properties is possible for materials in the nano regime and their enhancement leads to a new dimension of application which is at its peak versatility in case of the transition metal oxides due to their atomic and crystal structures.

1.2.1 PROPERTIES OF TMOs

TMOs show a variety of applications when reduced to the nano regime based on their different properties. As discussed above, they are known to be promising materials for a vast range of applications. A few important applications of the transition metal oxides are addressed below:

1.2.1.1 CATALYTIC PROPERTY

Catalysts may be defined as chemical species that alters the rate of a chemical reaction without changing its own state chemically or physically. It is known to enhance a chemical reaction, reduce the activation energy of formation of chemical compounds or increase the rate of a slow chemical process. As for example, organometallic complexes like Ferrocene, Nickelocene etc. are used as catalysts for the synthesis of three-dimensional carbon nanostructures. TMOs show promising catalytic application in their original form or in some complex form. These are mainly surface phenomenon and they mainly act as adsorbant surface thereby adsorbing the required chemical species or providing the surface for the reaction to occur. The catalysis may be physical, chemical, or biological. Some materials are known to degrade industrial pollutants in presence of electromagnetic radiations like ultra violet or visible light. Such type of a reaction is known as photocatalytic reaction. TMOs like ZnO, TiO_2, V_2O_5 etc. are known to be excellent photocatalysts degrading highly toxic textile industry effluents like Rhodamine-B, Congo Red etc.[38-41]

1.2.1.2 ADSORPTION PROPERTY

TMOs possess adsorption capacities when reduced to nano level due to their surface defects, porosity and vacancies generated within the nanostructure. Several oxides like NiO, Fe_2O_3, Fe_3O_4 etc. show promising adsorption capacity of heavy metals like Cr(VI) ions.[42,43] The heavy metal ions are known to cause damage and degradation to the environment. They are also known to cause fatal diseases in human beings like Itai-Itai disease for Cd(II), Minamata disease for Hg(II) and many more. Heavy metals like Cr(VI) in drinking water are responsible for accelerating tumor generation biochemical pathways within the human system thereby causing carcinogenic effects.[44] The main source of these inorganic heavy metals are the industrial effluents that are often discharged into nearby water bodies thereby causing heavy damage to the surrounding human and aquatic systems. The nanoparticles due to their porous nature and high surface area are suitable candidates for heavy metal ion removal from waste water. The nanoparticles have the potential to replace the contemporary materials like mesoporous carbon, activated charcoal etc. that are used commercially used as potential adsorbents in the purification of drinking water.

1.2.1.3 ELECTRONIC PROPERTY

The TMOs show excellent electronic properties when subjected to an electric field. Several TMOs like NiO, CuO, ZnO etc. act as semiconductors with tunable bandgaps.[45] Thus, these materials in nano dimensions i.e. may be in the form of thin films, quantum dots, nanostructures or three dimensional nanoparticles show excellent transport properties of electrons which are very useful in the fabrication of resistive switches, tunable resistors etc. Wide bandgap materials like higher oxides of nickel are promising candidates for Schottky diodes and solar cell fabrication. The oxides have also been applied for the fabrication of the dye sensitized solar cells (DSSC).[46] Nanostructures of oxides like NiO are used as capacitor plates in lithium ion batteries, gas sensors when prepared as thin films.[47-49] Thus, the oxides show promising applications in the sensing, capacitance, device fabrication, electrical transport applications etc. which are required nowadays for almost all industries as there is a rapid requirement of integrated circuits and the semiconducting industry is at its full bloom.

1.2.1.4 OPTICAL PROPERTY

TMOs like ZnO, TiO_2 etc. show excellent photoluminescence property and are potential material for fabrication of LEDs and other light emitting devices.[50] These materials have a donor or acceptor level or any impurity level at an energy gap from which if an electron jumps from conduction band to a defect level, the emitted energy falls within the visible or ultra violet range. The oxide materials when reduced to nano level consists of defect states that gives rise to fluorescence or phosphorescence depending on the position of the defect state. The defect states are created due to variation of synthesis procedure, formation of nanostructures, variation of particle size etc.

1.2.1.5 ANTIMICROBIAL PROPERTY

Several oxides show antimicrobial effects and hence they find a great variety of application in pharmaceutical, paints and chemical industries. All submerged metallic parts, water transport systems etc. are coated with antimicrobial paints consisting of oxide nanoparticles to prevent fouling of the submerged surfaces. Antimicrobial coatings are also applicable to surgical accessories to provide ultra sterilization to the surgical instruments. TMOs like ZnO, TiO_2, Ni_2O_3 etc. provide excellent antibacterial effect to both gram negative and gram positive bacterial sub colonies. Few oxides of essential metallic ions like Fe_2O_3 are found to enhance bacterial growth and hence are useful in adequate dosage in agricultural soil for the growth of soil bacteria.

1.2.1.6 MAGNETIC PROPERTY

TMOs show excellent magnetic property due to the presence of vacant d-orbitals or unpaired electrons in their d-sub shell. They may be ferromagnetic, paramagnetic, antiferromagnetic and diamagnetic base on the orientation of the electron spin. The magnetic property of the TMOs is used extensively for the design of several spintronic devices like Spin FET, Magnetic memory devices, Spin LED etc. Oxides like NiO, Fe_2O_3, CuO etc. are suitable candidates to be used as magnetic materials. Asymmetric nanostructures like coral like or flower like morphologies of different oxides show magnetic property due to the defects created and a strain generated within the structure.

1.2.1.7 BIOLOGICAL PROPERTY

Some TMOs like ZnO are known to be used for tumor cell destruction and potential drug delivery application.[51] Several magnetic nanoparticles are extensively used as biological markers, hyperthermia treatment procedures, detection and diagnosis of oncogenes and oncoproteins etc. Nanoparticles like Fe_2O_3 coated with biological polymeric macromolecules like Dextran, Chitosan etc. are known to segregate within a phagocytic cell and generate a contrast in MRI.[52] TiO_2 nanoparticles allow osseointegration of artificial medical implants and bone. TiO_2 is also used as a pigment, a thickener, and a UV absorber in cosmetic and skin care products thereby protecting skin from UV light exposure.[53] ZnO has high biocompatibility and fast electron transfer kinetics which enables the use of these materials as a biomimic membrane for immobilization and modification of biomolecules.[54]

Apart from these properties, TMOs and their nanoparticles may be used as paints, abrasives, wave filters, UV detectors, transparent conductive films, varistors, gas sensing etc. Hence, TMOs are an indispensible material in modern industry and is in use extensively in almost all manufacturing, production and maintenance industries ranging from pharmaceutical to aviation.

1.2.2 WHY TITANIUM DI-OXIDE?

Titanium (Ti) is one of the mostly available material in the earth crust (ninth). The common raw materials are rutile, ilmenite and leucoxene. Ti may have been in the oxide form of TiO, Ti_2O_3, TiO_2, Ti_3O_5, Ti_4O_7; Ti_nO_{2n-1} where, n ranges between 3– 9[55,56]. The most stable form is TiO_2 (Titanium (IV) oxide or titania) which is used in cosmetics, drugs, pigment, paper, and semiconductor[57]. The reason of application of TiO_2 as a semiconductor is due to its many advantages like low cost, wide abundancy, nontoxicity, biocompatibility, stability, proper band gap energy and photocatalytic activity[58]. After discovery of water splitting by Fujishima and Honda, TiO_2 was mostly studied for photocatalytic applications [59]. The photocatalytic ability of TiO_2 depends on its crystallinity, crystal structure, grain size, surface properties, morphology and composition[60].

1.2.3 STRUCTURAL POINT OF VIEW

TiO_2 has three main crystal structure which are anatase, rutile and brookite as seen in Figure 1.4. The structural properties of the phases calculated by Pseudopotential Hartree-Fock model and some physical propeties are tabulated in Table 1.1. It has also other synthetic forms in monoclinic, tetragonal and orthorhombic structures[61,62]. Also it has five high pressure forms which are α-PbO_2-like, baddeleyite-like, cotunnite-like, orthorhombic and cubic phase[62-64].

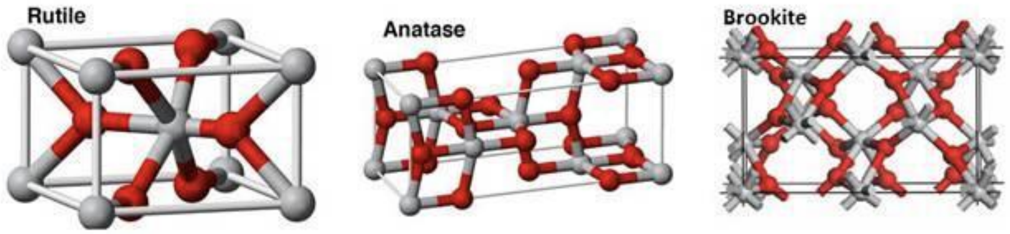

Figure 1.4 Structure of different phases of TiO_2

Property	Rutile	Anatase	Brookite
Crystal structure lattice constants (Å)	Tetragonal a=4.5936 c=2.9587	Tetragonal a=3.784 c=9.515	Orthorhombic a=9.184 b=5.447 c=5.145
Space group	$P4_2/mnm$	$I4_1/amd$	*Pbca*
Molecule/cell	2	4	8
Volume/molecule (Å^3)	31.2160	34.061	32.172
Density (g/cm^3)	4.13	3.79	3.99
Ti-O bond length (Å)	1.949(4) 1.980(2)	1.937(4) 1.965(2)	1.87~2.04

Table 1.1 Structural properties of different phases of TiO_2

Rutile is the most stable form of TiO_2. Anatase phase of TiO_2 is a metastable one, which is widely used for photocatalytic applications due to its wide band gap, surface properties, proper structure for electron diffusion. In general, majority of TiO_2 synthesis processes result in rutile formation. It is mostly used in high temperature conditions such as gas sensors. Brookite is another metastable phase of TiO_2 between anatase and rutile. It is generally ignored due to difficulty of synthesis. Ti^{+4} atoms are coordinated to six oxygen atoms to form [TiO_6] octahedra in all three forms of TiO2. Anatase phase is formed by corner sharing octahedras, rutile is formed by edge sharing of octahedras, and brookite is formed by both edge and corner sharing of octahedras [57]. Some physical property classification of anatase and rutile are shown in Table 1.2.

Property	Anatase	Rutile
Molecular Weight (g/mol)	79.88	79.88
Melting point (^{O}C)	1825	1825
Boiling point (^{O}C)	2500~3000	2500~3000
Specific gravity	3.9	4
Light absorption (nm)	<380	<415
Mohr's hardness	5.5	6.5-7.0
Refractive index	2.55	2.75
Dielectric constant	31	114

Table 1.2 Physical properties of different phases of TiO_2

1.2.4. N-TYPE BEHAVIOUR

TiO_2 could be recognized as an insulator material due to its wide band gap energy (3 eV for rutile, 3.2 eV for anatase). However, TiO_2 becomes in oxygen deficiency when it is equilibrated under low oxygen atmosphere. Thus, it becomes an n-type semiconductor with free electrons as charge carriers. The defects in oxygen deficient form could be caused by both intrinsic and extrinsic types which are controlled by experimental conditions and foreign anions and/or cations, respectively. The reduced charge regime is mainly a function of Ti^{+3} interstitials, which are compensated by electrons. The strongly reduced part is due to doubly ionized oxygen vacancies and reduced regime is dominated by ionic charge compensation. The oxidized part could be achieved by high oxygen partial pressure. All these defects have a significant importance on electrical properties of TiO_2. The valance band corresponds to O related states and the conduction band corresponds to Ti related states. Anatase possesses a narrower 3d band compared to rutile, which is the result of localization of Ti 3d states due to large Ti-Ti atomic distances in this polymorph.

1.3 SYNTHESIS PROCEDURES OF OXIDE NANOPARTICLES

Oxide nanoparticles are synthesized in several approaches. They may be chemical, biological, physical vapor deposition, chemical vapor deposition, co-precipitation, hydrothermal, solvothermal, sol-gel etc. Generally, the synthesis of oxide is a two-step process: first is the preparation of a hydroxide precursor and second is the calcination of the hydroxide precursor to form oxide at high temperatures of about 400-500^{o}C. Out of these, the most abundantly used synthesis technique for nickel oxide is the hydrothermal or solvothermal technique. This is mainly used for the generation of morphologies based on surfactants that require the effect of temperature and pressure to vary the nucleation rate. Several morphologies like rod, flower, coral, sphere, spindle shape etc. can be generated by hydrothermal approach that can be applied to several applications. Several hierarchial structures can also be generated using this approach. However, calcination in high power consuming furnace is inevitable for the synthesis of the oxide structures. This makes the oxide synthesis process costly in terms of power consumption. The process is also tedious and not environment friendly. As a result, a low temperature process of oxide preparation is an absolute necessity.

1.4 APPLICATION OF TiO_2

1. TiO_2 is also an effective opacifier in powder form, where it is employed as a pigment to provide whiteness and opacity to products such as paints, coatings, plastics, papers, inks, foods, medicines (i.e. pills and tablets) as well as most toothpastes.

2. In cosmetic and skin care products, titanium dioxide is used both as a pigment, sunscreen and a thickener because of its high refractive index (n = 2.7), its strong UV light absorbing capabilities and its resistance to discolouration under ultraviolet light.

3. Titanium dioxide, particularly in the anatase form, is a photo-catalyst under ultraviolet (UV) light. TiO2 is most efficient and environmentally benign photo-catalyst. It is a semiconductor which turns to a high energy state by receiving light energy, and releases electrons from its illuminated surface. If the energy received at this stage is high enough, electrons that are initially located in the valence band all jump up to the conduction band. The electron hole pair is generated, which generate free radicals able to undergo secondary reaction. This forms the principle of photo-catalytic activity of photo generated catalysis. The hole produced has strong oxidizing power and the electrons have strong reducing power. Due to this, it has wide applications in food testing labs, medical fields etc.

The photo-catalyst activity of a semiconductor is largely controlled by:

a) The light absorption properties like light absorption spectrum and coefficient.

b) Reduction and oxidation rates on the surface by electron and hole.

c) Electron hole recombination rate.

A large surface area with a constant surface density of absorbents leads to faster surface photo-catalysis rate. On the other hand, the surface is defective site, therefore, large the surface area, the faster the recombination. The higher the crystallinity, the fewer the bulk defects, and the higher the photo-catalytic activity is.

4. Used for Anti-fogging glasses, self-cleaning glass, anti-bacterial, anti-viral, fungicidal, anti-soiling, self-cleaning, deodorizing, air purification, water treatment, water purification.

5. Used in electronic components like capacitor

REFERENCES

1. M.C. Roco, J. Nanoparticles Res. 1999, **1**, 435.
2. J. Aizenberg et al., Nature 1999, **398**, 495.
3. G. Binnig et al., Phys. Rev. Lett., 1982, **49**, 57.
4. H. Gleiter, in Deformation of Polycrystals: Mechanisms and Microstructures, eds. N. Hansen et al. (Risø Nat. Lab., Roskilde) 1981, **15**.
5. R. Feynmann, “There is plenty of room at the bottom”, talk given on Dec. 29th 1959 at the annual meeting of the American Physical Society at the California Institute of Technology (Caltech); published in Caltech’s Engineering and Science, Feb. 1960.

6. G. Stix, Sci. Am.,, 2001, 26.

7. M. Faraday, Philos. Trans. Royal Soc., 1857, **147**, 145.
8. L. Becker et al., Nature 1999, **400**, 227.
9. K.E. Drexler, Engines of creation: The coming era of nanotechnology, (Oxford University Press, Oxford, 1986); K.E. Drexler, C. Terson, G. Pergamit, Unbounding the Future: The Nanotechnology Revolution (Morrow, New York, 1991); K.E. Drexler, Nano systems: Molecular Machinery, Manufacturing, and Computation, (Wiley, New York, 1992).
10. J. Yu et al., Environ. Sci. Technol. 2008, **42**, 4902
11. L. Zhang, Journal of Colloid and Interface Science, 2006, 297, 660.
12. W. H. Meikljohn et al., Phys. Rev. 1953, **105**,904.
13. G. Moore, Electronics 1953, **38**, 8.
14. G.E. Moore, ISSCC Dig. Tech. Pap., 2003, 20.
15. J. Wood, Materials today 11, Jan-Feb 2008, 40.

16. O. Bourgeois et al., Phys. Rev. Lett., 2005, **94**, 057007. 17. C.L. Jia, K. Urban, Science 2001 (2004), 303.

18. D. Attwood, Nature 2006, **442**, 642.

19. M. di Ventra et al. (eds.), Introduction to Nanoscale Science and Technology (Springer, New York, 2004).
20. E.L. Wolf, Nanophysics and Nanotechnology (Wiley-VCH, Weinheim, 2006)

21. G.L. Hornyak et al., Introduction to Nanoscience and Nanotechnology (Taylor and Francis Group, Boca Raton, 2009)
22. I. Thomas, P. Dehmer, MRS Bull., October 2001, 761.
23. 23. S.J. Park, J. Am. Chem. Soc. 2000, **122**, 8581.
24. J.D. Dunitz, L.E. Orgel, Journal of Physics and Chemistry of Solids**,** 1957, **3(3–4)**, 318
25. K., Ueda, H. Tabata, T. Kawai, 2001, Applied Physics Letters, **79(7)**, 988.
26. C. N. R., Rao, B. Raveau. Annual Review of Physical Chemistry, 1989, **40.1**, 291.
27. H. Hu, I.E. Wachs; J. Phys. Chem., 1995, **99 (27)**, 10911.
28. Y. Moritomo, A. Asamitsu, H. Kuwahara, Y. Tokura; Nature, 1996, **380**, 141.
29. S.Gandhi, K.Thandavan, S.Sethuraman, U.M.Krishnan;Journalof PorousMaterials, 2013, **20(5)**, 1009.
30. B. Salehi**,** S. Mehrabian**,** M. Ahmadi; Journal of Nanobiotechnology, 2014, **12**:26.
31. W.E. Pickett, Rev Mod Phys, 1989, **61**, 433.
32. J. He, Y. Liu, R. Funahashi, J. Mater Res, 2011, **26,** 1762.
33. I. Terasaki, Y. Sasago, K. Uchinokura, Phys Rev B, 1997, **56,** 12685-7.
34. K. Koumoto, I. Terasaki, R. Funahashi, MRS Bull, 2006, **31**, 206-10.
35. I. Terasaki I, M. Iwakawa, T. Nakano, A. Tsukuda, W. Kobayashi, Dalton T, 2010, **39,** 1005-11.
36. I. Terasaki, J Appl Phys, 2011, 110.
37. S. Walia, S. Balendhran, H. Nili, S. Zhuiykov, G. Rosengarten, Q. H. Wang, M. Bhaskaran, S. Sriram, M.S.Strano,K.K.Zadeh,ProgressinMaterialsScience(2013)
38. S. Chin, E. Park, M. Kim, G.N. Bae, J. Jurng, Materials letters, 2012, **75**, 57.
39. M. Batzill, Energy Environ. Sci.**,** 2011, **4**, 3275.
40. M. Ghaedi, M.N. Biyareh , S.N. Kokhdan, S. Shamsaldini, R. Sahraei, A. Daneshfar, S. Shahriyar, Materials Science and Engineering C, 2012, **32**, 725.
41. H. Lachheb, E. Puzenat, A. Houas, M. Ksibi, E. Elaloui, C. Guillard, J.M. Herrmann, Applied Catalysis B: Environmental, 2002, **39**, 75.
42. E. Liu, H. Zhao, H. Li, G. Li, Y. Liu, R. Chen, New J. Chem., 2014, **38**, 2911.
43. J. Hu, G. Chen, I. M.C. Lo, Water Research, 2005, **39,** 4528.

44. Pietruska, J.R., Liu, X., Smith, A., McNeil, K., Weston, P., Zhitkovich, A., Hurt, R., Kane, A.B., Toxicological Sciences, (2011).
45. F.J. Morin, Physical review, 1954, **93(6)**, 1999.
46. S. Feihl, R.D. Costa, S Pflock, C. Schmidt, J. Schonamsgruber, S. Backes, A. Hirsch, D.M. Guldi, RSC Advances, 2012, **2**, 11495.
47. J.L. Gunjakar, A.M. More, C.D. Lokhande, Sensors and Actuators B, 2008, 131, 356.
48. M.A. Vidales-Hurtado, A. Mendoza-Galván, Solid State Ionics, 2008, **179**, 2065.
49. A. Fihri, R. Sougrat, R.B. Rakhi, Raed Rahal, Dongkyu Cha, M.N. Hedhili, M Bouhrara, H.N. Alshareef, V. Polshettiwar, ChemSusChem 2012, **5**, 1241.
50. T. Nishide, M. Sato, H. Hara, Journal of materials science, 2000, **35.2**, 465.
51. J.W. Rasmussen, E. Martinez, P. Louka, D.G. Wingett, Expert Opin Drug Deliv. 2010, **7(9)**, 1063.
52. T. Schlorf, M. Meincke, E. Kossel, C.C. Glüer,, O. Jansen, R. Mentlein, 2010. International journal of molecular sciences, ***12*****(1)**, 12.
53. Y.W. Huang, C.H. Wu and R.S. Aronstam, Materials, 2010, **3**, 4842.
54. S.A. Kumar, S.M. Chen, Anal. Lett., 2008, **41**, 141.
55. S.-C. Chiao, B. G. Bovard, H. A. Macload, Applied Optics, 1998,**37**, 5284.
56. M. Levin, C. R. L Robbins, H. F. Mcmurdie, Phase Diagrams for Ceramists, M.K. Reser, Ed., Ohio: The American Ceramic Society, 1964.
57. H. Shi, R. Magaye, V. Castranova, J. Zhao, Part Fibre Toxicol, 2013,**10**.
58. M. Grätzel, Nature, 2001, **414**, 338.
59. A. Fujishima, K. Honda, Nature, 1972, **238,** 37.
60. M. Kurtoglu, "Effect of doping on the photocatalytic, electronic and the mechanical properties of sol-gel titanium dioxide films," Ph.D Thesis, Drexel University, 2011.
61. A. Fujishima, T. N. Rao, D. A. Tryk J. Photochem. Photobiol.C , 2000,**1**,1.
62. N. A. Dubrovinskaia, Phys. Rev. Lett., 2001,**87**, 275501.
63. L. S. Dubrovinsky, Nature, 2001,**410**, 653

64. Marchant, L. Brohan, M. Tournoux, Mater. Res. Bull., 1980,**15**, 1129.

CHAPTER 2

OBJECTIVES OF THE STUDY

The present study aims to synthesize TiO_2 rutile phase; by varying precursor concentration by one step hydrothermal synthesis.

A detailed description of the aims and objectives are listed as follows:

- Development of a single step, low temperature, fast synthesis procedure of TMO using inorganic chemical synthesis approach.
- Synthesis of flower like morphology of TiO_2 with variation of NaCl concentration at low temperature without calcination.
- Study of the defect states generated within nanoparticles and coral like nanostructures with variation of NaCl concentration.
- Study of the effect of defect state on the lattice parameter
- Fabrication and study of Photodiode characteristics formed by deposition of TiO_2 on p-Si substrate and study variation of electrical parameters with defect concentration.

CHAPTER 3

REVIEW OF LITERATURE

3.1 TITANIUM DI-OXIDE NANOSTRUCTURE

One-dimensional TiO_2 or titanate related nanomaterials with high morphological specificity, such as nanotubes, nanosheets, nanoribbons, nanowires, nanofibers and nanorods, have attracted considerable attention due to their interesting chemical and physicochemical properties. The high interest to the one-dimensional materials was initiated by first carbon nanotube discovery in the early 1990s[1] which is promising for many applications due to their excellent mechanical, optical, electrical and/or chemical properties. Nevertheless, materials other than C are much easier to synthesize due to diverse chemistry[2-4]. The 1D structures may be used in a wide range of applications such as medical purpose[5], electrochemistry[6,7], environmental purification[8,9], gas sensors[10]. A time line showing briefly the historical background of TiO_2 related nanotubular structures can be seen in Figure 3.1.

The first TiO_2-based nanotubes was reported by Hoyer in 1996[11] via an electrochemical deposition using naturally occurring porous aluminum oxide. Up to now 1D TiO_2 nanostructures were synthesized using three different methods which are chemical template synthesis[12], electrochemical anodic oxidation method[13] and alkaline hydrothermal treatment[4]. The preparation of TiO_2 1D structure by chemical templating usually involves controlled sol-gel hydrolysis of Ti compounds in the presence of templating agents followed by polymerization of TiO_2 in the self-assembled template or deposition of TiO_2 on the surface of the template[2]. The procedure ends by removing templating agent and calcination. Although the template assisted method attracted much attention in the early 2000s which makes possible to prepare numerous materials with a regular and controlled morphology by adjusting the template morphology, this method is mostly disadvantageous because of the high cost of template material separating[3,12].

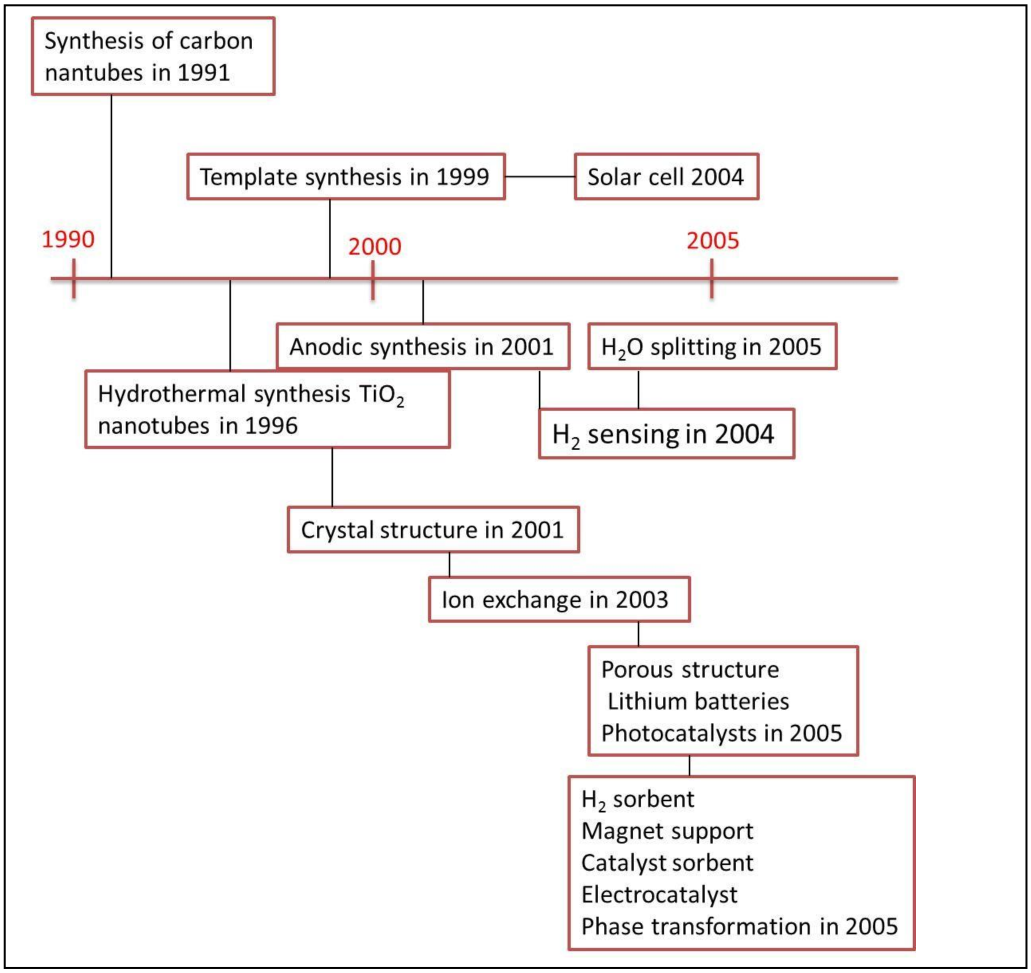

Figure 3.1 Timeline of development of TiO_2

In 2001, Grimes and co-workers[13] reported the self-organized TiO_2 nanotube arrays by direct anodization of Ti foil in a H_2O-HF solution at room temperature. The nanotubes were oriented in the same direction. The thickness of the film was only 200 nm. One end is open while the other end in contact with foil was always closed. However, nanotubes cannot be separated from each other and should be calcined for crystalline material. In 1998, Kasuga and co-workers[4] first reported a simple method for the preparation of TiO2 nanotubes by hydrothermal process using precursor TiO_2 in a strong alkaline solution (KOH or NaOH) at high temperature for a long time followed by a washing step with water or acidic solutions. In a typical process, several grams of TiO_2 can be converted to any 1D structure at temperatures in the range 110-150°C[4]. It has been shown that any TiO_2 structure (anatase, rutile, brookite, amorphous forms) can be transformed into 1D structure. There are a large number of crystal modifications after hydrothermal treatment. Several titanate structures achieved after hydrothermal treatment and/or post treatments were summarized by

Bavykin et al.[2]. These structures are given in Table 3.1.

Crystallographic phase	Symmetry	2θ (degree)					
$H_2Ti_3O_7$	Monoclinic	11		24.4	29	48.4	62
$H_2Ti_2O_4(OH)_2$	Orthorhombic	9		24.3	28	48	62
$H_2Ti_4O_9$	Monoclinic	10		24	28	48	
$H_2Ti_{2-x/4}\ _{x/4}O_4.H_2O$	Orthorhombic	9.5		24.5	28	48	62
TiO_2 B	Monoclinic		15	25	29.5	48	62
$H_2Ti_5O_{11}.H_2O$	Monoclinic	10	14			46	

Table 3.1 structure variation of different phases of TiO_2

Layered titanate nanostructures are promising not only because of the advantage of easy and cheap production, but also because of the intriguing hydrated structure and morphological changes induced by surface chemistry. However, there are several problems for determining the crystal structure of alkaline hydrothermal product. The most important problem is instability. Structure easily transforms by washing with distilled water, acidic treatment, and calcination. The other one is small crystals cause small coherent area which results in broadening of the peaks forming reflections in the XRD data. Furthermore, wrapping or spreading along a certain crystallographic axis during the formation of 1D structure, results in widening of peaks making assignment difficult. Initially, Kasuga and co-workers[4] suggested that their product is anatase. Peng and co-workers[14,15] proposed that the crystal structure of titanate nanotubes corresponded to the layered trititanic acid ($H_2Ti_3O_7$) with a monoclinic crystal structure. A schematic showing the crystal structure of monoclinic trititanic acid in a TiO_6 edge-sharing octahedron representation is shown in Figure 3.2[2]; the three different projections corresponding to crystallographic axes. A nanotubular morphology of layered trititanic acid may be formed by obtained by rolling several (100) planes around axis [010] or [001][2]. It has been proposed that rolling of the plane occurs around the [010] axis such that the axis of the nanotube is parallel to the b-axis of monoclinic $H_2Ti_3O_7$. Wu et al.[16] have proposed that rolling of the (100) plane could occur around axis [001]. In both cases, the walls of the nanotubes consist of several layers, typically separated by 0.72 nm. The structure of each layer corresponds to the structure of the (100) plane of monoclinic titanates, which is a set of closely packed TiO_6, edge-sharing octahedral.

Zhang et al. [110], based on the studies of Na content, suggested the crystal structure of $H_2Ti_2O_4(OH)_2$. It was demonstrated that bulk layered protonated titanates could be transformed to the metastable monoclinic modification of TiO_2 (TiO_2-B) under calcination[3]. This modification of TiO_2 has a lower density than anatase or rutile and has a monoclinic unit cell. The structure of TiO_2-B is characterized by a combination of edge- and corner-sharing TiO_6 octahedra forming a structure with channels in which transport and exchange of small cations can occur[2]. Indeed, washing of sodium titanate nanotubes with acid or water results in the formation of the protonated form of titanate nanotubes[2]. Following drying at increased temperatures, dehydration of solids and formation of TiO_2-B nanotubes could occur, the product having a density in the range 3.64–3.76 g cm^{-3}, which is less than the density of anatase or rutile (3.9 and 4.25 g cm^{-3}, respectively)[2]. The XRD pattern of TiO_2-B crystals, however, is a little different from that of TiO_2 nanotubes, especially at small 2θ values (Table 3.1). The calcination of titanate nanofibers results in consecutive transformation from titanate to TiO_2-B (at 400 °C), then to anatase (at 700 °C) and rutile (at 1000 °C). Nanofibrous morphology disappears at 1000 °C[61].

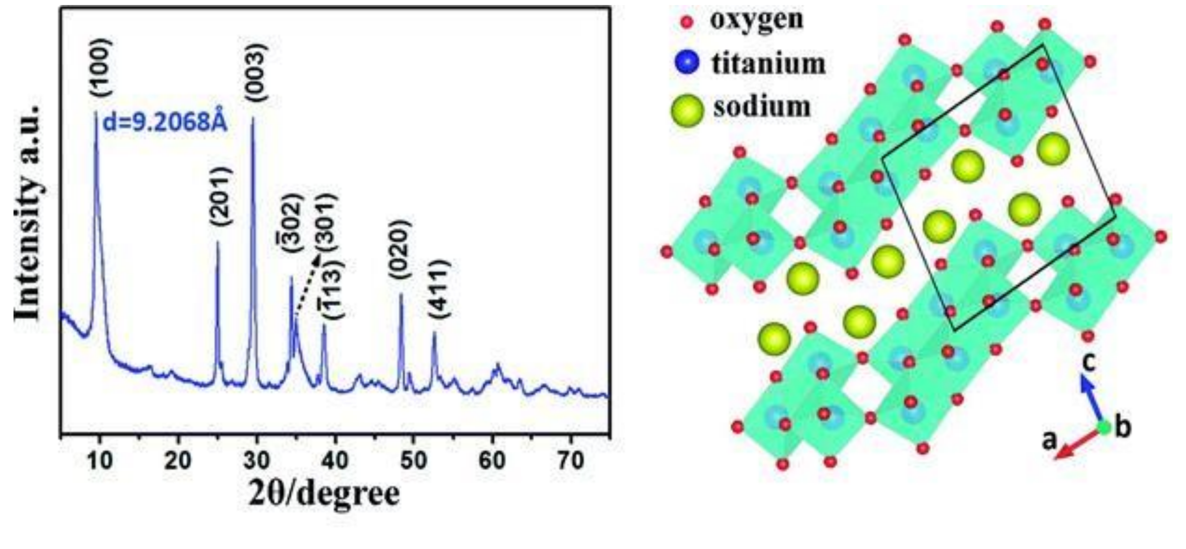

Figure 3.2 Typical XRD pattern of $Na_2Ti_3O_7$ and (b) Crystal structure of Na titanate

Since the discovery of wet chemical method, several attempts have been done to understand the mechanism of transformations. Originally, Kasuga and co-workers[4] considered that a tubular morphology is being achieved after washing of the hydrothermal product. Some of the researchers still support this proposal. However, it was demonstrated that, 1D structure is being formed during hydrothermal synthesis[18]. The long, solid, parallelepiped titanates are named nanoribbons, nanobelts, or nanofibers in the literature. These structures tend to have good crystallinity and usually the relation between the lengths of the edges corresponding to each crystallographic axis is in the order 001 >> 100 > 010[19]. The length of nanofibers (001) can be several tens of micrometers, while the width of nanofibers (001 or 010) is typically in the range 10–100 nm[2]. The aspect ratio can be as large as several thousand. Nanofibers, which are usually produced during alkaline hydrothermal reactions at high temperatures, can be found in straight as well as in curved forms[2]. Zhang et al.[20] considered that single surface layers experienced an asymmetrical chemical environment, due to the imbalance of H^+ or Na^+ ion concentration on two different sides of a nanosheet, giving rise to excess surface energy, resulting in bending. Another, the morphology of the derived titanate is also controversial as nanotube, nanoribbon, nanosheet or nanorod, all have been observed[21]. Chen et al.[14] and Morgado et al.[22] suggested that the formation of titanate tubes is independent of the original structure and particle size of the TiO_2. Zhang et al.[23] manifested that a smaller raw material generally exhibits a higher surface energy, which is favorable for the formation of nanotubes after hydrothermal treatment. On the other hand, Yuan et al.[24] found that nanofibers, rather than nanotubes, are obtained when amorphous TiO_2 or commercial $TiOSO_4$ is used as the precursor.

Titanate nanotubes are wide-band gap semiconductor materials. From studies of the optical properties of aqueous colloids of titanate nanotubes at room temperature, the band gap has been estimated to be ca. 3.87 eV[25]. The surface area and porosity of titanate nanofibers produced at temperatures higher than 170°C is much lower than that of nanotubes[19]. The 1 D architectures attracts the interest to exploit them in the wastewater treatment field[9]. However, the photocatalytic activity of titanate structures strongly depends on the nature of the pollutant, the crystallographic structure, the calcination treatment, and the presence of alkali ions (Na^+, K^+) in the structure[26]. In this respect, the photo degradation of acetone in air was successfully found to occur by Yu et al. using calcined samples of nanowires at 500°C[27], these samples showing a photocatalytic activity 1.8 times higher than Degussa P25. Turki et al.[9] reported that H- titanate calcined at 400°C formed of TiO_2 anatase nanotubes to a photocatalyst 4 times more active than P25 for the degradation of formic acid (FA). Also, they concluded that any structure involving Na was found to be inert toward the photocatalytic degradation of FA showing the role of sodium as recombination centers for photo generated electron-hole pairs. Bavykin et al.[2] reported titanate nanotubes are more suitable for adsorption of positively charged dyes in contrast to conventional TiO_2 photoanodes in DSSCs. They also mentioned the instability of titanate structures at high temperatures which is a requirement for doctor blade method. Another problem is random orientation of one-dimensional structures of the photoanode which inhibits the transport of electron to the FTO[28].Taccihini et al.[29] applied their nanotube structures synthesized by hydrothermal treatment to DSSC as nanotube, nanotube/nanoparticle, nanorod and nanorod/nanoparticle. The highest efficiency was yielded by cells consisting only nanotubular structure.

3.2HYDROTHERMAL SYNTHESIS OF TIO_2 NANOSTRUCTURES USING ACID CATALYZER

Anatase, rutile or brookite TiO2 nanocrystallites are reported to be synthesized using hydrothermal method with amorphous TiO_2, $TiCl_4$, $TiOCl_2$ aqueous solution, and titanium alkoxides via acidic hydrothermal process[30-33]. The catalyzer type, pH, dwell time and temperature are important for the final morphology and crystal structure[30,34]. Thermodynamically most stable phase of TiO_2 is rutile which can be obtained by high temperature calcination of the kinetically stable anatase phase. However, the calcination unavoidably causes sintering of the nanocrystallites. Many reports suggested that hydrothermal methods under acidic conditions were applicable for synthesis of rutile nano particles, as well as anatase and brookite nano particles. Yanagisawa and Ovenstone[35] reported that hydrothermal process using an amorphous TiO_2 suspension prepared by neutralization of $TiCl_4$ and by hydrolysis of $Ti(OC2H5)_4$ under acidic conditions using HCl (0.5M) led to the formation of a mixture of anatase, brookite, and rutile phases in nanosize. Aruna et al.[36] reported the synthesis of 20 nm rutile nanocrystallites with titanium isopropoxide in the presence of nitric acid (pH 0.5) under vigorous stirring during hydrothermal treatment. Furthermore, Yin et al.[30], reported phase-pure TiO_2 nanocrystallites with narrow particle-size distributions by hydrothermal processes starting from amorphous TiO_2. They reported that autoclaving amorphous TiO_2 in the presence of HF and HCl as cooperative catalysts led to the formation of narrow-sized anatase TiO_2, nitric acid as a cooperative catalyst with HF also gave the anatase TiO_2 with a narrow size distribution but with a rather irregular crystalline surface, while amorphous TiO_2 was converted to phase-pure rutile TiO_2 nanocrystallites by autoclaving in the presence of citric and nitric acids. Andersson et al.[37] treated microemulsions with different acid catalyzers which are HCl and HNO_3 and concluded that if hydrochloric acid was used, the rutile structure formed, and if nitric acid was used, anatase formation occurred. Nian and Teng[38], synthesized anatase nanorods using HNO_3 aqua solution of $H_2Ti_2O_5.H_2O$ nanotubes as precursor of hydrothermal process. Dai et al.[39] obtained pure anatase nanoparticles in the lower HCl concentration (0.1-1 M) and 8 M HCl, a mixture of rutile and anatase in the 2 M to 7 M acidic concentration using cetyltrimethylammonium bromide surfactant agent (Hex-ncTiO_2/CTAB). Zhou et al.[40] synthesized rutile nanostructures with different morphologies by changing the acid molarity of hydrothermal precursor solution containing tetrabutyl titanate. HCl molarity varied between 1 and 10, aggregations, microspheres, nanoflowers, nanotrees, and nanobelts were formed.

Wilson et al.[41] reported anatase and brookite binary phase resulted in HNO3 assisted microwave hydrothermal process. Also, they concluded that microwave limits Oswald ripening which provides nanoparticles with small diameters. Wang et al.[42] prepared solutions by hydrolysis precipitation with a water:alkoxide ratio of 165. After recovery and drying, these samples were hydrothermally aged at 180 °C in an acid-free solution for 1 day, 1 M HNO_3 solution for 1 day, 1.5 M HNO_3 solution for 1 day, and 1 N HNO_3 solution for 7 days which were resulted in anatase, anatase-rutile, rutile-anatase and rutile formation, respectively. Dai et al.[43] demonstrated that well-defined anatase TiO_2 nanocrystals with exposed {001} facets could be synthesized in high yields by controlling the hydrolysis rate of the sol-gel precursor and acid assisted hydrothermal treatment. Authors mentioned the importance of pH value of the medium used for hydrothermal treatment which played an important role in controlling the morphology of the obtained TiO_2 nanocrystals. Grimes and co-workers reported the hydrothermal/solvothermal synthesis of rutile TiO_2 nanorods of 10−35 nm diameter from a toluene/HCl (10 M) mixture using a sol−gel-derived TiO_2 seed layer on F-SnO_2 (FTO)[44]. Liu and Aydil firstly reported growth of TiO2 rutile nanorods on the surface of FTO glass with hydrothermal method with 1:1 volume of HCl and water facilitating the lattice mismatch between FTO and TiO_2[45]. Hosono et al.[46] discussed the recrystallization process i.e. dissolve and grow process of TiO_2 nanostructures by hydrothermal process. The hydrolysis reaction in strong acidic media can be explained as follows[46]:

$$2Ti + 6\,HCl \rightarrow 2TiCl_3 + 3\,H_2\,(g)$$
$$Ti^{3+} + H_2O \rightarrow TiOH^{2+} + H^+$$
$$TiOH^{2+} + O_2^- \rightarrow Ti(IV) - \text{Oxo species-}\ O_2^- \rightarrow TiO_2$$

Erdogan et al.[47] synthesized rutile TiO_2 nanoflowers using TTIP precursor, strong HNO_3 catalyzer and covering the hydrothermal vessel by titanate structures at relatively lower temperatures.

Both anatase and rutile can grow from the [TiO_6] octahedra, and the phase formation proceeds by the structural rearrangement of the octahedral. As anatase structure involves more Ti atoms, in the presence of NO_3^- ions which has higher affinity to Ti atoms, anatase formation is reported more favorable[48]. Anatase formation under strong acidic hydrothermal conditions may be explained by dissolution and recrystallization and/or insitu transformation[49]. An alternative interpretation of the Ostwald Step Rule has that the first phase to form will be the one possessing the least surface energy with respect to the reactant[50]. Although rutile is the most stable phase, anatase formation may be favored in hydrothermal system due to less surface energy of this polymorph compared to rutile[51]. It was observed that high pH favors anatase, low pH favors rutile, while intermediate pH and reactant concentration stabilize the brookite phase[52]. The three kinds of phase-pure TiO_2 exhibit their distinctive crystal shapes: rounded nanocrystals for anatase, nanoplates for brookite, and nanorods for rutile[53]. Brookite structure has both shared edges and corners and is midway between those of anatase and rutile in terms of the shared edges (four for anatase, three for brookite, and two for rutile)[52]. This might be the reason why brookite needs intermediate pH to stabilize. Pottier et al.[54] suggested that the Cl^- ions in the reaction system template the growth of brookite structure.

Some of the brookite research with hydrothermal process claims that basic media is important for brookite formation[55] such as Keesmann[56] was the one who firstly synthesized pure brookite by hydrothermal treatment of amorphous TiO_2 obtained by hydrolysis of titanium tetraisopropoxide or alkaline titanates, in the presence of a solution of NaOH containing 3–25 atoms, % of Na with respect to total amount of Ti and Na. Na^+ ions were claimed to stabilize the lattice of brookite but Schwarzmann and Ognibeni[57] synthesized well crystallized brookite by hydrothermal treatment of TiO_2 and H_2O between 100 and 300°C in the absence of Na^+ ions. Additionally, brookite was obtained by milling anatase-phase powders. Wakamatsu et al.[58] synthesized almost single phase brookite after 54 ks and 72 ks ball milling of anatase under the condition of medium intensity. Brookite nanoflowers consisting of single crystalline nanorods were prepared by hydrothermal treatment of a solution containing titanium butoxide. Single-phase brookite was extracted from the suspension by centrifugal separation. It is worth noting that the final products of several syntheses reported in the literature are not really single phase brookite since they contain traces of anatase or rutile, as clearly evidenced by the XRD patterns[59]. The existence of brookite in the resultant powders is readily discernible from its (121) diffraction located at 30.81° (2θ) in the XRD pattern, where no overlapping of this peak with any one from anatase or rutile occurs. To claim phase-pure brookite, however, attentions should be paid to the brookite (121) and (120) peaks, as the strongest diffraction from anatase ((101), d=0.352 nm), if there is any, overlaps with the strongest diffraction from brookite ((120), d=0.351), and this may alter the apparent Ibrookite (121) /Ibrookite (120) intensity ratio. Ideal brookite has a Ibrookite (121) / Ibrookite (120) ratio of 0.9 (JCPDS: 21-1276)[55].

3.3PHOTODIODE CHARACTERISTICS OF OXIDE NANOPARTICLES

Titanium dioxide is a semiconducting material having bandgap ~3.0 eV, for rutile phase. In nano level, TiO_2 behaves as an n type or p type material based on the type of defect present within the structure. A non- stoichiometric combination of titanium and oxygen results in the formation of a wide bandgap material, as shown in figure 3.3. Wide bandgap materials are capable of forming photodiodes. With incorporation of defect state TiO_2 behaves like a n-type semiconductor, which when deposited onto p-Si substrate is capable of forming bulk heterojunction photodiode. Parameters such as sensitivity, responsivity, diode current are the properties expected to reveal from the photocurrent measurement.[60]

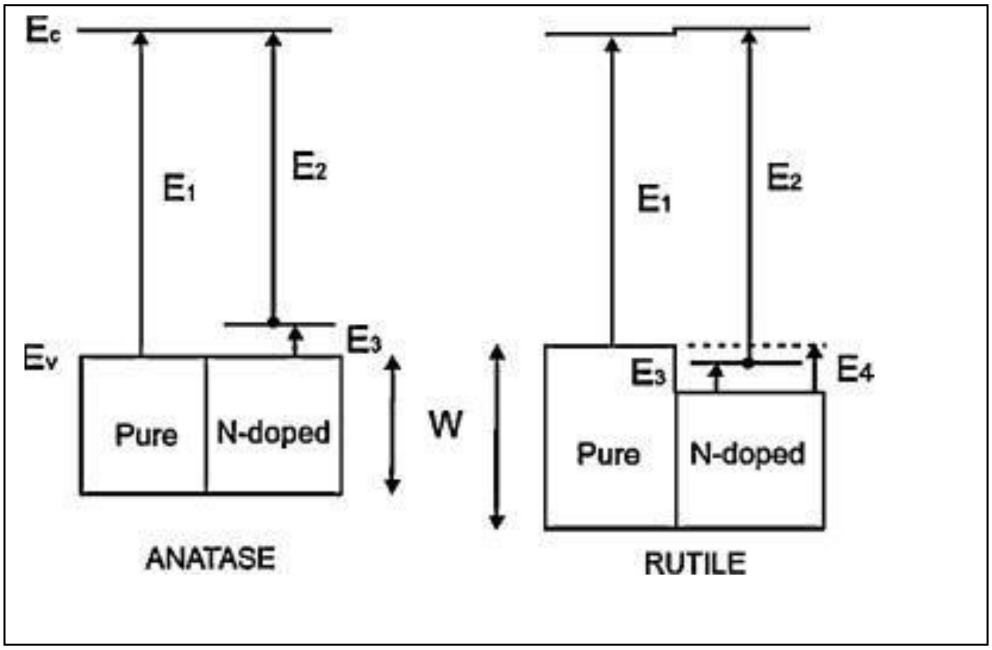

Figure 3.3 Bandstructure of anatase and rutile TiO_2

REFERENCES

1. S. Iijima, "Helical microtubules of graphitic carbon," *Nature*, vol. 354, p. 56, 1991

2 D. V. Bavykin, J. M. Friedrich, F. C. Walsh, "Protonated titanates and TiO_2 nanostructured materials: Synthesis, properties, and applications," *Adv. Mater.*, p. 2807, 2006.

3 D. V. Bavykin, F. C. Walsh, Titanate and Titania Nanotubes: Synthesis, Properties and Applications, Cambridge: Royal Society of Chemisty, 2010.

4 T. Kasuga, M. Hiramatsu, A. Hoson, T. Sekino, K. Niihara, "Formation of titanium oxide nanotube," *Langmuir*, vol. 14, p. 3160, 1998.

5 J. Boudon, A. L. Papa, J. Paris, N. Millot, "Titanate nanotubes as a versatile platform for nanomedicine," in *Nanomedicine*, One Central Press (OCP), A. Seifalian, A. De Mel, D. M. Kalaskar Ed., p. 403, 2014.

6 L. Zhang, Q. Zhang, J. Li, "Layered titanate nanosheets intercalated with myoglobin for direct electrochemistry," *Advanced Functional Materials*, vol. 17, p. 1958, 2007.

7 J. Li, Z. Tang, Z. Zhang, "Pseudocapacitive characteristic of lithium ion storage in hydrogen titanate nanotubes," *Chemical Physics Letters*, vol. 418, 506, 2006.

8 Q. X. Deng, C. Z. Huang, W. Xie, H. C. Xu, M. D. Wei, "Synthesis and application of titanate nanotubes," *Applied Mechanics and Materials*, no. 331, p. 400, 2013.

9 A. Turki, H. Kochkar, C. Guillard, G. Berhault, A. Ghorbel, "Effect of Na content and thermal treatment of titanate nanotubes on the photocatalytic degradation of formic acid," *Applied Catalysis B: Environmental*, vol. 139,401, 2013.

10 G. H. Jain, L. A. Patil. P. P. Patil, U. P. Mulik, K. R. Patil, "Studies on gas sensing performance of pure and modified barium strontium titanate thick film resistors," *Mater Sci*, vol. 30, p. 9, 2007.

11 P. Hoyer, "Formation of a titanium dioxide nanotube array," *Langmuir*, vol. 12, p. 1411, 1996.

12 J. C. Hulteen, C. R. Martin, "A general template-based method for the preparation of nanomaterials," *J. Mater. Chem.*, vol. 7, p. 1075, 1997.

13 D. Gong, C. A. Grimes, O. K. Varghese, W. Hu, R. S. Singh, Z. Chen, E. C. Dickey, "Titanium oxide nanotube arrays prepared by anodic oxidation," *Journal of Materials Research*, vol. 16, p. 3331, 2001.

14 Q. Chen, G. Du, S. Zhang, L. M. Peng, "The structure of trititanate nanotubes," *Acta Crystallogr.*, vol. 58, p. 587, 2002.

15 G. H. Du, Q. Chen, R. C. Che, Z. Y. Yuan, L.-M. Peng "Preparation and structure analysis of titanium oxide nanotubes," *Appl. Phys. Lett.*, vol. 79, p. 3702, 2001.

16 D. Wu, J. Liu, X. Zhao, A. Li, Y. Chen, N. Ming, "Sequence of events for the formation of titanate nanotubes, nanofibers, nanowires, and nanobelts," *Chem. Mater.*, vol. 18, p. 547, 2006.

17 M. Zhang, Z. Jin, J. Zhang, X. Guo, J. Yang, W. Li, X. Wang, Z. Zhang, "Effect of annealing temperature on morphology, structure and photocatalytic behavior of nanotubed $H_2Ti_2O_4(OH)_2$," *Journal of Molecular Catalysis A: Chemical*, vol. 217, p. 203, 2004

18 D. V. Bavykin, V. N. Parmon, A. A. Lapkin, F. C. Walsh, "The effect of hydrothermal conditions on the mesoporous structure of TiO_2 nanotubes," *J. Mater. Chem.*, vol. 14, p. 3370, 2004.

19 W. Zhou, H. Liu, R. I. Boughton, G. Du, J. Lin, J. Wang, D. Liu, "One-dimensional single-crystalline Ti–O based nanostructures: properties, synthesis, modifications and applications," *J. Mater. Chem.*, vol. 20, p. 5993, 2010.

20 S. Zhang, L. M. Peng, Q. Chen, G. H. Du, G. Dawson, W. Z. Zhou, "Formation mechanism of $H_2Ti_3O_7$ nanotubes," *Phys. Rev. Lett.*, vol. 91, No: 25, 2003.

21 H.-H. Ou, S.-L. Lo, "Review of titania nanotubes synthesized via the hydrothermal treatment: Fabrication, modification, and application," *Separation and Purification Technology*, vol. 58, p. 179, 2007.

22 E. Morgado Jr., M. A. S. de Abreu, O. R. C. Pravia, B. A. Marinkovic, P. M. Jardim, F. C. Rizzo, A. S. Araújo, "A study on the structure and thermal stability of titanate nanotubes as a function of sodium content," *olid State Sciences*, vol. 8, p. 888, 2006.

23 Q. Zhang, L. Gao, J. Sun, and S. Zheng, "Preparation of long TiO_2 nanotubes from ultrafine rutile nanocrystals," *Chem. Lett.*, vol. 31, p. 226, 2002.

24 Z.-Y. Yuan, B.-L. Su, "Titanium oxide nanotubes, nanofibers and nano-wires," *Colloids Surf. A*, vol. 5241, p. 173, 2004.

25 D. V. Bavykin, S. N. Gordeev, A. V. Moskalenko, A. A. Lapkin, F. C. Walsh, "Apparent two-dimensional behavior of TiO_2 nanotubes revealed by light absorption and luminescence," *J. Phys. Chem.*, vol. 109, p. 8565, 2005.

26 S. Ribbens, I. Caretti, E. Beyers, S. Zamani, E.Vinck, S. Van Doorslaer, P. Cool, "Unraveling the photocatalytic activity of multiwalled hydrogen trititanate and mixed-phase anatase/trititanate nanotubes: A combined catalytic and EPR Study," *J. Phys. Chem. C*, vol. 115, p. 2302, 2011.

27 H. Yu, J. Yu, B. Cheng, "Photocatalytic activity of the calcined H-titanate nanowires for photocatalytic oxidation of acetone in air," *Chemosphere*, vol. 66, p. 2050, 2007.

28 J. Qu, C. Lai, "One-dimensional TiO_2 nanostructures as photoanodes for dye-sensitized solar cells," *Journal of Nanomaterials*, vol. 2013, 762730 2013.

29 . Tacchini, A. Ansón-Casaos, Y. Yu, M.T. Martínez, M. Lira-Cantu, "Hydrothermal synthesis of 1D TiO_2 nanostructures for dye sensitized solar cells," *Materials Science and Engineering B*, vol. 177, p. 19, 2012.

30 H. Yin, Y. Wada, T. Kitamura, S. Kambe, S. Murasawa, H. Mori, T. Sakata, S. Yanagida, "Hydrothermal synthesis of nanosized anatase and rutile TiO_2 using amorphous phase TiO_2," *J. Mater. Chem.*, vol. 11, p. 1694, 2001.

31 Z. R. Ismagilov, L. T. Tsikoza, N. V. Shikina, V. F. Zarytova, V. V. Zinoviev, N. Zagrebelnyi, "Synthesis and stabilization of nano-sized titanium dioxide," *Russian Chemical Reviews*, vol. 78, p. 873, 2009.

32 M. Cerna, C. Guillard, E. Puzenat, M. Vesely, P. Dzik, "Hydrothermal synthesis of TiO_2: influence of process

conditions on photocatalytic activity," *International Journal of Chemical and Environmental Engineering*, vol. 2, 2011.

33 T.-D. N. Phan, H. D. Pham, T. V. Cuong, E. J. Kim, S. Kim, E. W. Shin, "A simple hydrothermal preparation of TiO_2 nanomaterials using concentrated hydrochloric acid," *Journal of Crystal Growth*, vol. 312, p. 79, 2009.

34 M. Ahmadi, M. R. Ghasemi, H. H. Rafsanjani, "Study of different parameters in TiO_2 nanoparticles formation," *Journal of Materials Science and Engineering*, vol. 5, p. 87, 2011.

35 J. Ovenstone, K.Yanagisawa, "Crystallization of anatase from amorphous titania using the hydrothermal technique: Effects of starting material and temperature," *J. Phys. Chem. B*, vol. 103, p. 7781, 1999.

36 S. T. Aruna, S. Tirosh, A. Zaban, "Nanosize rutile titania particle synthesis via a hydrothermal method without mineralizers," *J. Mater. Chem.*, vol. 10, p. 2388, 2000.

37 M. Andersson, L. Österlund, S. Ljungström, A. Palmqvist, "Preparation of nanosize anatase and rutile TiO_2 by hydrothermal treatment of microemulsions and their activity for photocatalytic wet oxidation of phenol," *J. Phys. Chem. B*, vol. 106, p. 10674, 2002.

38 J. N. Nian, H. Teng, "Hydrothermal synthesis of single-crystalline anatase TiO_2 nanorods with nanotubes as the precursor," *J Phys Chem B*, vol. 110, p. 4193, 2006.

39 S. Dai, Y. Wu, T. Sakai, Z. Du, H. Sakai, M. Abe, "Preparation of highly crystalline TiO_2 nanostructures by acid-assisted hydrothermal treatment of hexagonal-structured nanocrystalline titania/cetyltrimethyammonium bromide nanoskeleton," *Nanoscale Res Lett.* , vol. 5, p. 1829, 2010.

40 W. Zhou, X. Liu, J. Cui, D. Liu, J. Li, H. Jiang, J. Wang, H. Liu, "Control synthesis of rutile TiO_2 microspheres, nanoflowers, nanotrees and nanobelts via acid-hydrothermal method and their optical properties," *CrystEngComm*, vol. 13, p. 4557, 2011.

41 G. J. Wilson, G. D. Will, R. L. Frost, S. A. Montgomery, "Efficient microwave hydrothermal preparation of nanocrystalline anatase TiO_2 colloids," *J. Mater. Chem.*, vol. 12, p. 1787, 2002.

42 H. Wang, P. Liu, X. Cheng, P. Liu, L. Zheng, "Effect of surfactants on synthesis of TiO_2 nano-particles by homogeneous precipitation method," *Powder Technology*, vol. 188, p. 52, 2008.

43 Y. Dai, C. M. Cobley, J. Zeng, Y. Sun, Y. Xia, "Synthesis of anatase TiO_2 nanocrystals with exposed {001} facets," *Nano Lett.*, vol. 9, p. 2455, 2009.

44 X. Feng, K. Shankar, O. K. Varghese, M. Paulose, T. J. Latempa, C. A. Grimes, "Vertically aligned single crystal TiO_2 nanowire arrays grown directly on transparent conducting oxide coated glass: synthesis details and applications," *Nano Lett.* , vol. 8, p. 3781, 2008.

45 B. Liu, E. S. Aydil, "Growth of oriented single-crystalline rutile TiO_2 nanorods on transparent conducting substrates for dye-sensitized solar cells," *J. Am. Chem. Soc.*, vol. 131, p. 3985, 2009.

46 E. Hosono, S. Fujihara, K. Kakiuchi, H. Imai, "Growth of submicrometer-scale rectangular parallelepiped rutile TiO_2 films in aqueous $TiCl_3$ Solutions under hydrothermal conditions," *Am. Chem. Soc.* , vol. 126, p. 7790, 2004.

47 N. Erdogan, J. Park, A. Ozturk, "Hydrothermal synthesis of 3D TiO_2 nanostructures using nitric acid: Characterization and evolution mechanism," *Ceram. Int.*, vol. 42, p. 5985, 2016.

48 S. M. Klein, J. H. Choi, "Synthesis of rutile titania powders: agglomeration, dissolution, and reprecipitation phenomena," *J. Mater. Res.*, vol. 18, p. 1457, 2003.

49 A. Matthews, "The crystallization of anatase and rutile from amorphous titanium dioxide under hydrothermal condition," *American Mineralogist,* vol. 61, p. 419, 1976.

50 U. Diebold, "The surface science of titanium dioxide," *Surface Science Reports,* vol. 48, p. 53, 2003

51 S. M. Gupta, M. Tripathi "A review of TiO_2 nanoparticles," *Chinese Sci Bull,* vol. 56, p. 1639, 2011

52 S. G. Kumar, K. S. R. K. Rao, "Polymorphic phase transition among the titania crystal structures in solution based approach: From precursor chemistry to nucleation process," *Nanoscale*, vol. 6, p. 11574, 2014.

53 J.-G. Li, T. Ishigaki, X. Sun, "Anatase, brookite, and rutile nanocrystals via redox reactions under mild hydrothermal conditions: phase-selective synthesis and physicochemical properties," *J. Phys. Chem. C,* vol. 111, p. 4969, 2007.

54 A. Pottier, C. Chanéac, E. Tronc, L. Mazerolles, J.-P. Jolivet, "Synthesis of brookite TiO_2 nanoparticles by thermolysis of $TiCl_4$ in strongly acidic aqueous media," *J. Mater. Chem.*, vol. 11, p. 1116, 2001

55 A. Di Paola, M. Bellardita, L. Palmisano, "Brookite, the least known TiO_2 photocatalyst," *Catalysts,* vol. 3, p. 36, 2013

56 I. Keesmann, "Zur hydrothermalen synthese von brookit," *Z. Anorg. Allg. Chem.*, vol. 346, p. 30, 1966.

57 E. Schwarzmann, K.-H. Ognibeni, "Notizen: Hydrothermale synthese von brookit TiO_2 / hydrothermal synthesis of brookite TiO_2," *Z. Naturforsch B,* vol. 29, p. 435, 1974.

58 *Soc. Powder Powder Metall.*, vol. 48, p. 950, 2001.

59 K. Tomita, V. Petrykin, M. Kobayashi, M. Shiro, M. Yoshimura, M. kakihana, "Water-soluble titanium complex for the selective synthesis of nanocrystalline brookite, rutile, and anatase by a hydrothermal method," *Angew. Chem. Int.,* vol. 45, p. 2378, 2006

60 A. M. Selmana,Z. Hassana, M. Hushama, N. M. Ahmeda,"A high-sensitivity, fast-response, rapid-recovery p–n heterojunctionphotodiode based on rutile TiO2nanorod array on p-Si(1 1 1)",*Applied Surface Science*,vol.305,p.445,2014.

61 S. Pavasupree, Y. Suzuki, S. Pivsa-Art, S. Yoshikawa, "Synthesis and characterization of nanoporous, nanorods, nanowires metal oxides," *Science and Technology of Advanced Materials,* vol. 6, p. 224, 2005

62 T. Wakamatsu, T. Fujiwara, K. N. Ishira, P. H. Shingu, "Formation of brookite-type TiO_2 titania by mechanical alloying,".

CHAPTER 4

CHARACTERIZATION TOOLS AND TECHNIQUES

LIST OF BASIC CHARACTERIZATION TOOLS AND TECHNIQUES:

4.1 X-RAY DIFFRACTION

4.2 FIELD EMISSION SCANNING ELECTRON MICROSCOPE (FESEM)

4.3 HIGH RESOLUTION TRANSMISSION ELECTRON MICROSCOPE (HRTEM)

4.4 FOURIER TRANSFORM INFRARED SPECTROSCOPY (FTIR)

4.5 UV/VISIBLE SPECTROPHOTOMETER

4.6 SPECTROFLUOROMETER−PL (PHOTOLUMINESCENCE)

4.7 RAMAN SPECTROSCOPY

4.1 X-RAY DIFFRACTION

X ray diffraction (XRD) is a characterization technique that is used to study the crystal structure and atomic arrangement of a sample. It is a rapid analytical technique required for phase detection and unit cell specifications in case of a crystalline material.[1] The atomic planes of a crystal cause an incident beam of X-rays to interfere with one another as they leave the crystal. The phenomenon is called X-ray diffraction. X-ray diffractometers consist of three basic elements: an X-ray tube (for X-ray production), a sample holder, and an X-ray detector.

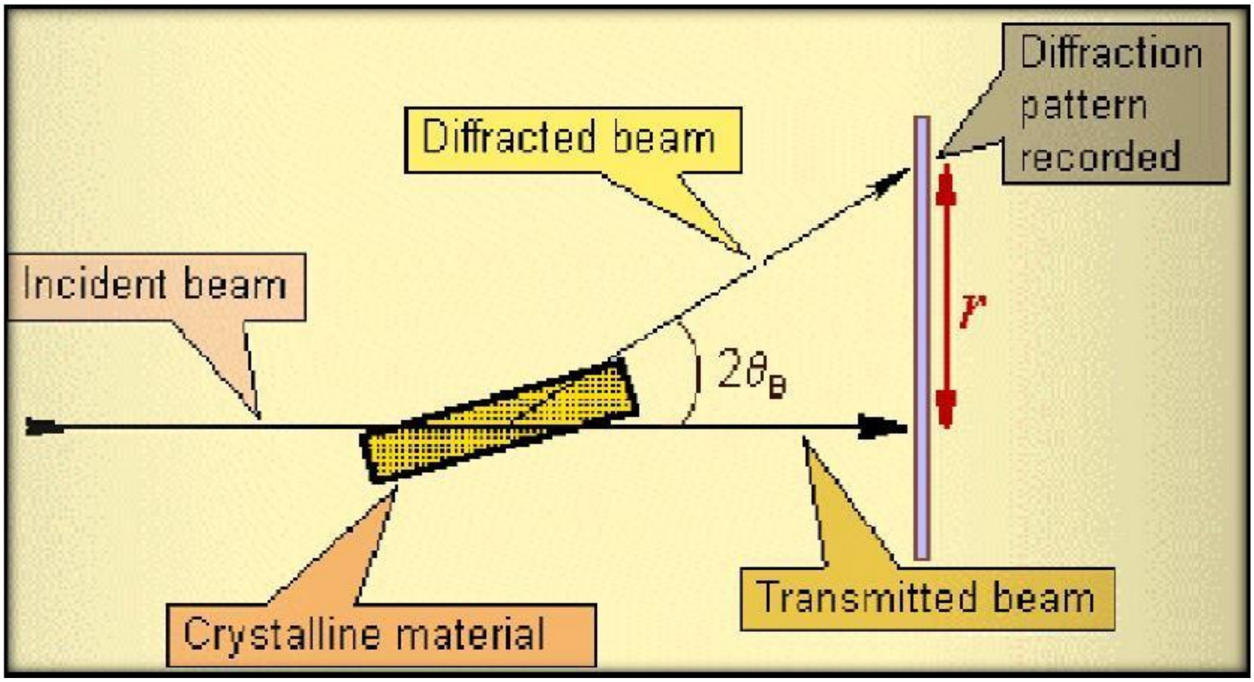

Figure 4.1: Schematic diagram of X-Ray Diffraction analysis technique

4.1.1 PRODUCTION OF X-RAY

X-rays are produced whenever high-speed electrons collide with a metal target. A source of electrons–hot Tungsten filament, a high accelerating voltage between the cathode (W) and the anode and a metal target, Cu, Al, Mo, Mg. The anode is a water-cooled block of Copper (Cu) containing desired target metal. When a highly energetic electron is incident

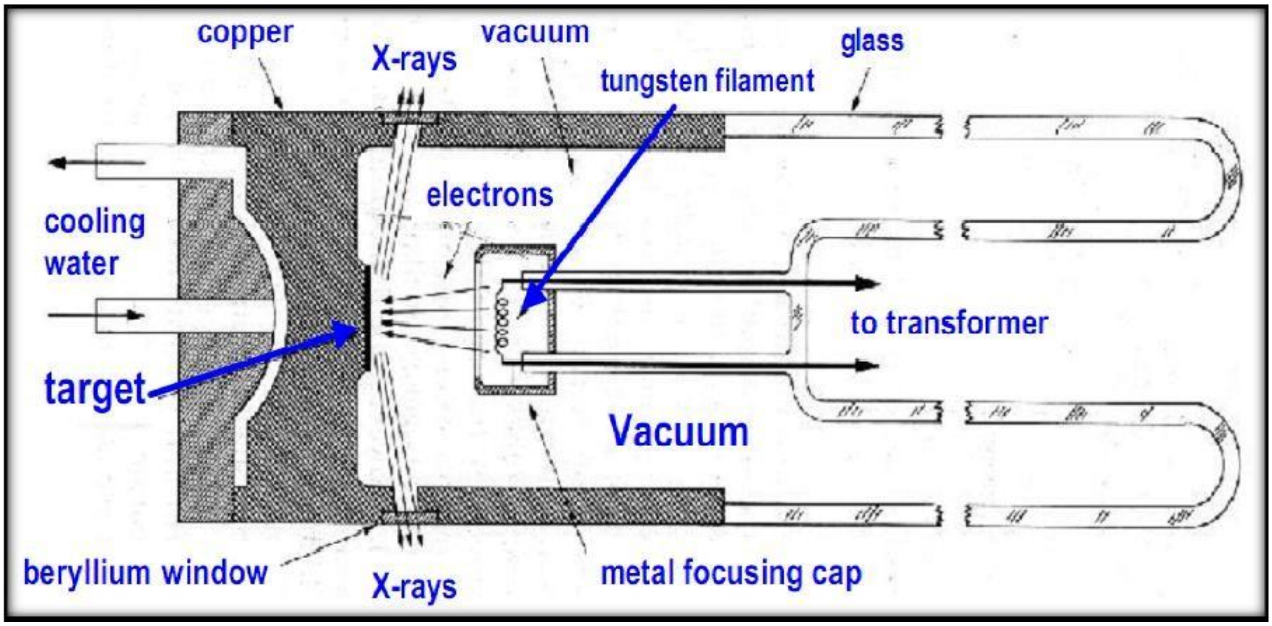

Figure 4.2: Schematic diagram of X-Ray Diffractometer setup (T.S. of Sealed off filament X-Ray tube)

X-rays are generated in a cathode ray tube by heating a filament to produce electrons, accelerating the electrons toward a target by applying a voltage, and bombarding the target material with electrons. When electrons have sufficient energy to dislodge inner shell electrons of the target material, characteristic X-ray spectra are produced. When a target is bombarded by highly energetic electron, two cases may occur: first case may be the electron may energize an inner shell electron to jump to its higher state. When it moves back to its original position, it releases energy in the form of electromagnetic radiation known as continuous X-ray. Secondly, it may so happen that sufficient collision energy is provided by the bombarding electron such that it knocks out an inner electron from the target material. In such a case, a higher energy electron fills the vacant space thereby releasing the energy in the form of electromagnetic radiation. This is known as characteristic X-ray. A schematic diagram of both the X- rays is illustrated below:

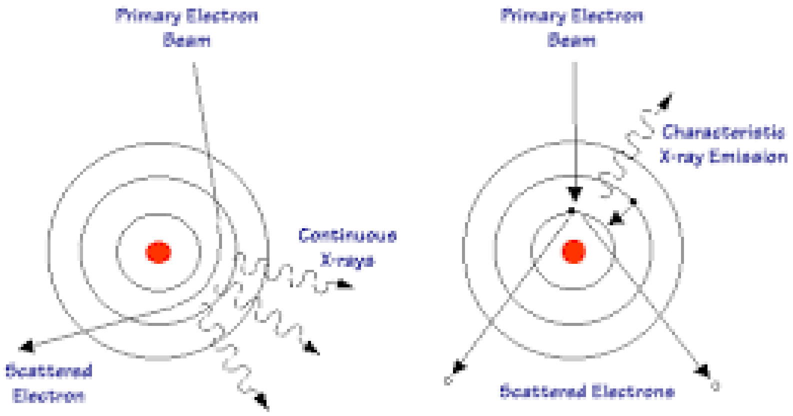

Figure 4.3: Formation of characteristic and continuous X-rays

4.1.2 IMPORTANCE OF XRD

Basically, XRD has several important uses to understand the phase, microstructure and atomic planar arrangement of an unknown crystal structure. These are as follows:

- Measure the average spacings between layers or rows of atoms
- Determine the orientation of a single crystal or grain
- Find the crystal structure of an unknown material
- Measure the size, shape and internal stress of small crystalline regions

4.1.3 DETERMINATION OF INTERPLANAR SPACING

The interplanar spacing ‘d’ is the fundamental parameter required to identify the crystal structure and phase of the sample under investigation. Diffraction occurs only when Bragg’s Law is satisfied Condition for constructive interference (X-rays) from planes with spacing d. The inter planer spacing calculated from **Bragg’s Law**. Bragg’s Law states that constructive interference takes place when $2d\sin\theta$ is an integral multiple of the wavelength of the incident electromagnetic radiation. Mathematically,

$\mathbf{2d_{hkl}\sin\theta = n\lambda}$, where ‘θ’ is the diffraction angle, ‘d’ is the interplanar spacing and ‘λ’ is the wavelength of the incident electromagnetic radiation.

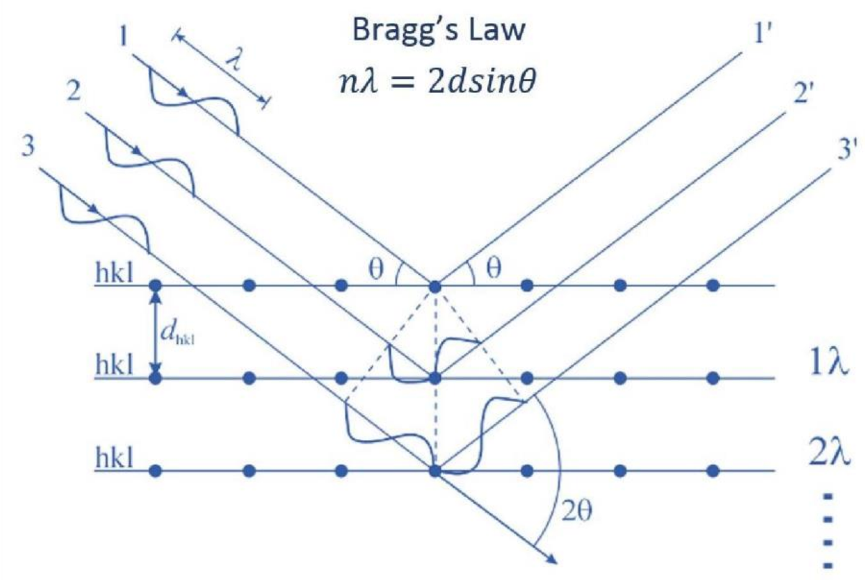

Figure 4.4: Schematic diagram of Bragg's Law

4.1.4 DETERMINATION OF LATTICE PARAMETER

A unit cell may be considered as the smallest building block of a crystal structure. A crystal consists of a periodic arrangement of the unit cell into a lattice. The unit cell can contain a single atom or atoms in a fixed arrangement. Crystals consist of planes of atoms that are spaced a distance d apart, but can be resolved into many atomic planes, each with a different d-spacing. a, b and c (length) and a, b and g angles between a, b and c are lattice constants or parameters which can be determined by XRD.

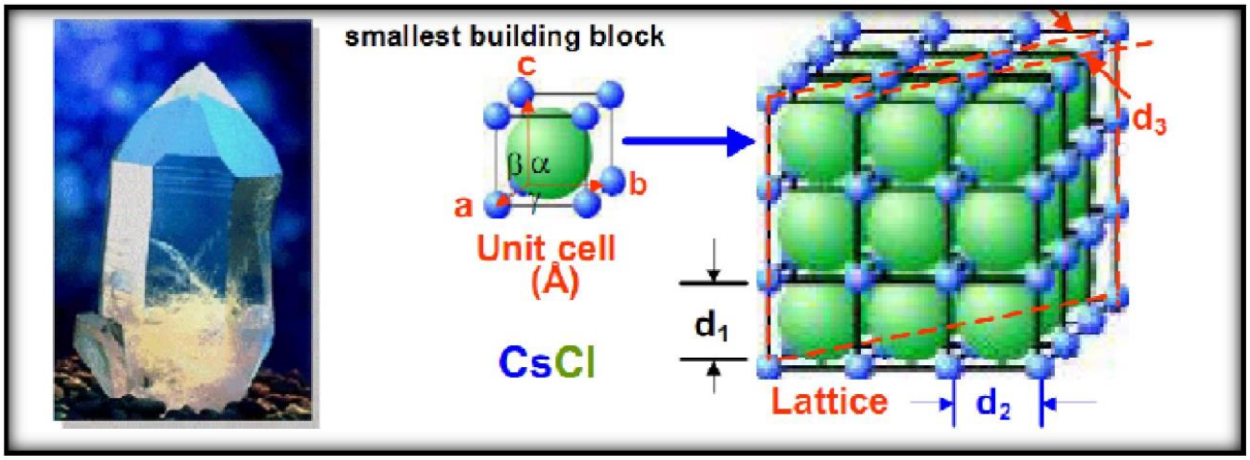

Figure 4.5: A unit cell and an aggregation of unit cells to form a crystal representing a crystallographic structure

Miller indices are the reciprocals of the fractional intercepts which the plane makes with the crystallographic axes.

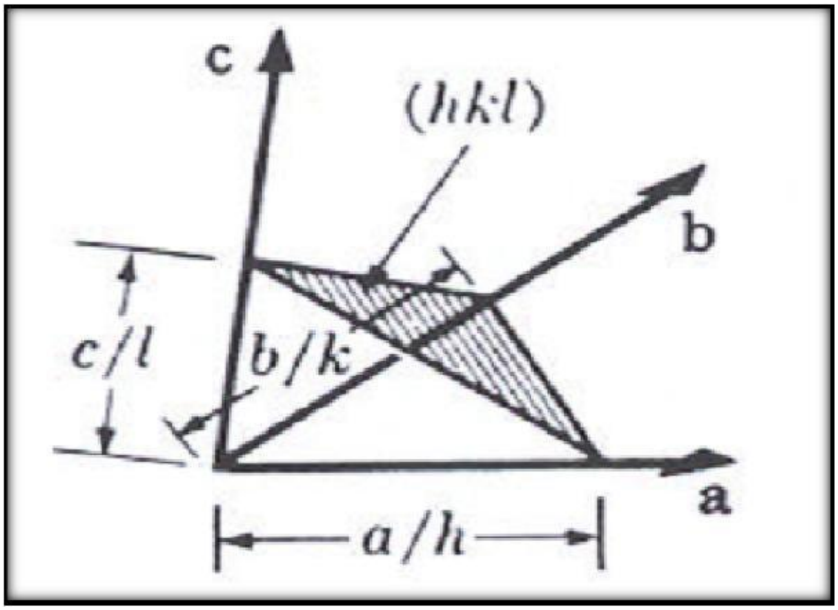

Figure 4.6: Cubic system for determination of the Miller indices

For a cubic system, the lattice parameters can be calculated using the following relation: For (h,k,l) plane:

$$\frac{1}{d^2_{h,k,S}} = \frac{(h^2 + k^2 + l^2)}{a^2} \qquad (4.1)$$

where, ‘d_{hkl}’ is the inter planer distance, ‘a’ is the lattice parameter, ‘h’, ‘k’, ‘l’ is known as Miller indices.

4.1.5 DETERMINATION OF PARTICLE SIZE OR GRAIN SIZE

X-ray diffraction technique is most utilized in determining the crystallite size or particle size based on the peaks obtained corresponding to the sample. This is calculated using the Scherrer’s formula.[1]

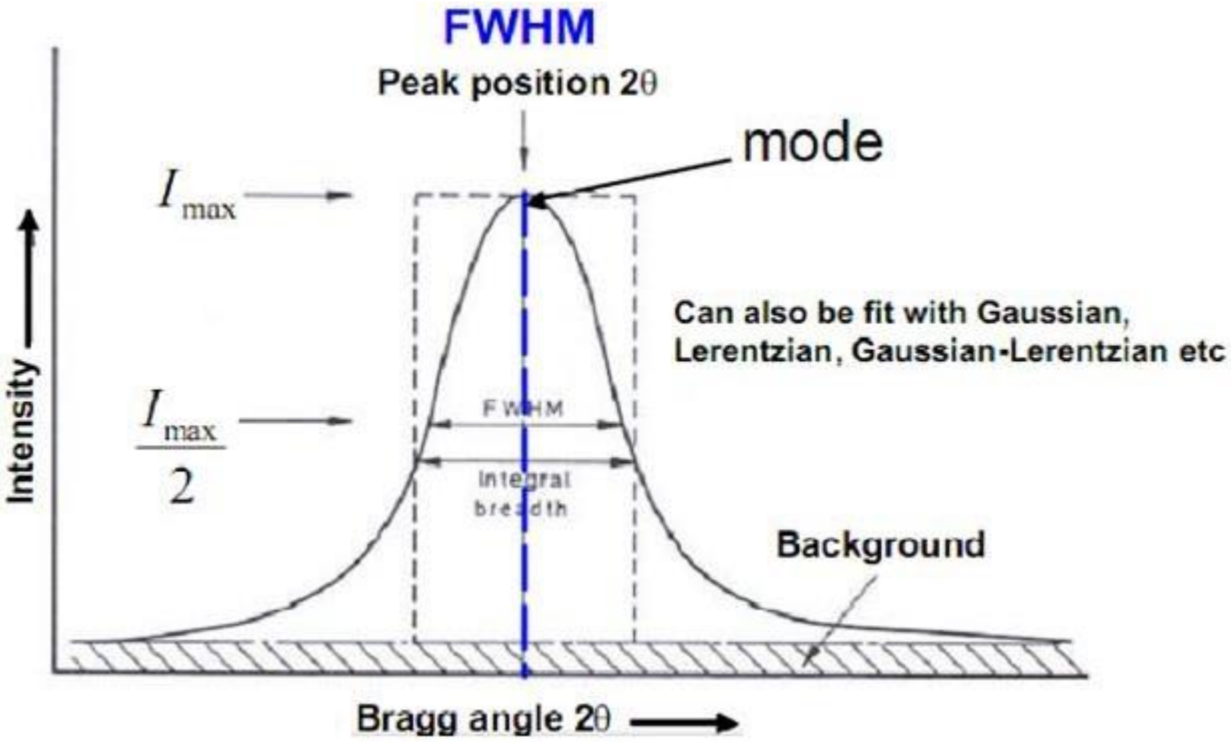

Figure 4.7: XRD Peak showing the measurement of FWHM for the calculation of particle size

The mean crystalline sizes of the powders are calculated using Scherrer's formula

$$D = 0.9\lambda / \beta \, \mathrm{Cos}\theta \qquad (4.2)$$

Where 'D' is the average crystallite size, λ =1.541˚A (X-ray wavelength**),** $\beta = (B^2\text{-}b^2)$, 'B' being the width of the diffraction peak at half maximum for the diffraction angle 2θ, b is calculated from the peak width of single crystal silicon wafer. Using this formula, the average crystallite size is calculated.

4.1.6 PHASE IDENTIFICATION

The phase identification is one of the most important analysis of the X-ray diffractogram. It is used to identify the phase, the crystal structure, the d-values etc. for in depth analysis of the material under observation.

Figure 4.8: Rigaku Ultima III, X-Ray Diffractometer

4.2 FIELD EMISSION SCANNING ELECTRON MICROSCOPE (FESEM)

An FESEM is microscope instead of light it works with electrons, liberated by a field emission source commonly known as a cold cathode. It is basically a low voltage device working on Field emission rather than Thermionic emission.

4.2.1 PRINCIPLE OF SCANNING ELECTRON MICROSCOPY

Under vacuum, electrons generated either by a low voltage source (cold cathode) or Field Emission Source in case of FESEM or a thermionic source in case of a SEM, are accelerated in a field gradient. The beam passes through Electromagnetic Lenses, focusing onto the specimen. As result of this bombardment different types of electrons are emitted from the specimen. A detector catches the secondary electrons and an image of the sample surface is constructed by comparing the intensity of these secondary electrons to the scanning primary electron beam. Finally the image is displayed on a monitor. A FESEM is used to visualize very small topographic details on the surface or entire or fractioned objects. Researchers in biology[2], chemistry and physics apply this technique to observe structures that may be as small as 1 nanometer (= billion of a millimeter). The FESEM may be employed for example to study organelles and DNA material in cells, synthetic polymers, and coatings on microchips.

4.2.2 PREPARATION OF THE SAMPLE

In order to be observed under a Scanning Electron Microscope, objects are first made conductive. This is done by coating them with an extremely thin layer (1.5 - 3.0 nm) of gold or gold palladium. Further on, objects must be able to sustain the high vacuum and should not alter the vacuum, for example by losing water molecules or gasses. Metals, polymers and crystals are usually little problematic and keep their structure in the SEM. Biological material, however, requires a prefixation, e.g. with cold slush nitrogen (cryo-fixation) or with chemical compounds. This particular microscope is foreseen of a special cryo-unit where frozen objects can be fractured and coated for direct observation in the FESEM. Chemically fixed material needs first to be washed and dried below the critical point to avoid damage of the fine structures due to surface tension. Coating is then performed in a separate device.

4.2.3 SOURCE OF ELECTRONS

In standard electron microscopes electrons are mostly generated by heating a tungsten filament by means of a current to a temperature of about 2800°C. Sometimes electrons are produced by a crystal of Lanthanum hexaboride (LaB_6) that is mounted on a tungsten filament. This modification results in a higher electron density in the beam *81* and a better resolution than with the conventional device. In a field emission (FE) scanning electron microscope no heating but a so-called "cold" source is employed. An extremely thin and sharp tungsten needle (tip diameter 10^{-7} –10^{-8} m) functions as a cathode in front of a primary and secondary anode. The voltage between cathode and anode is in the order of magnitude of 0.5 to 30 KV. Because the electron beam produced by the FE source is about 1000 times smaller than in a standard microscope, the image quality is markedly better. As field emission necessitates an extreme Vacuum (10-8 Torr) in the column of the microscope, a device is present that regularly decontaminates the electron source by a current flash. In contrast to a conventional tungsten filament, a FE tip last theoretically for a lifetime, provided the vacuum is maintained stable.[3] The figure below shows a schematic diagram of FESEM.

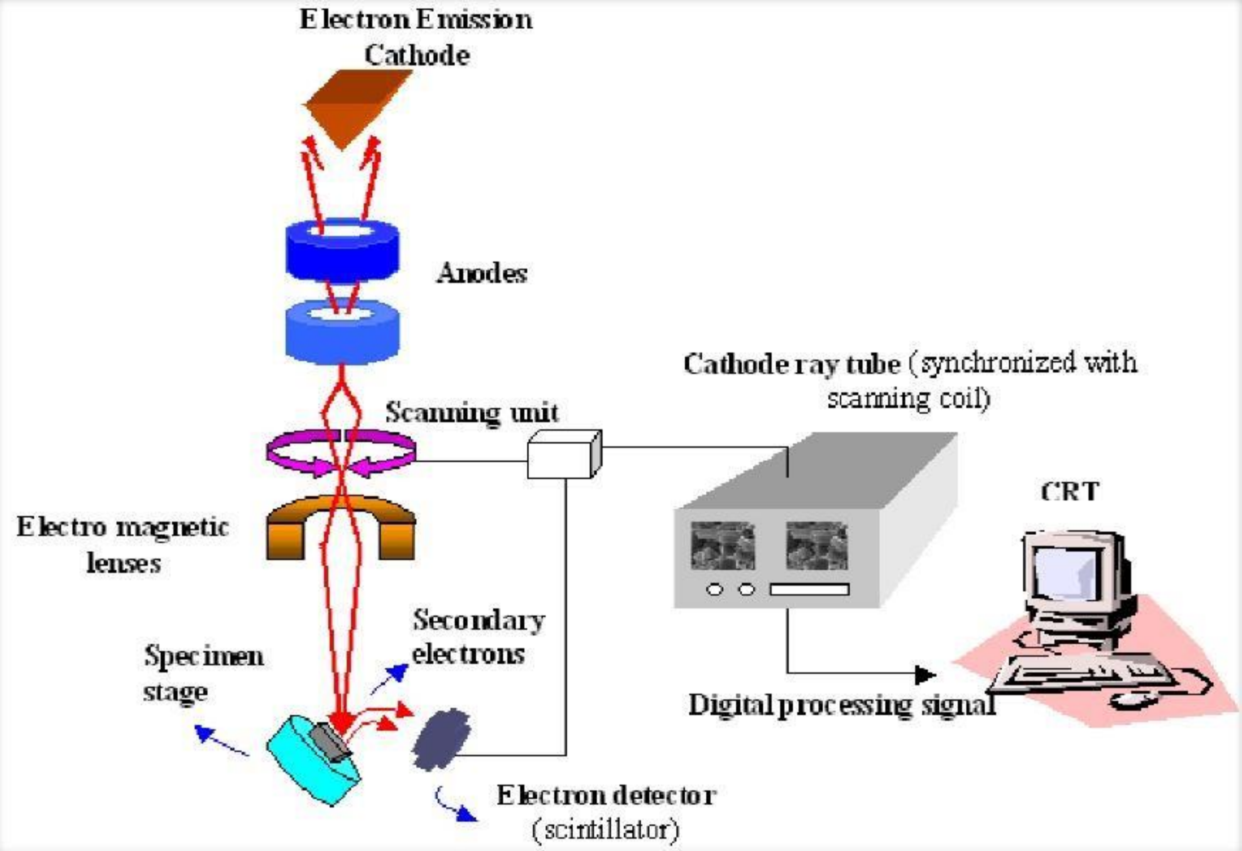

Figure 4.9: Schematic diagram of a Scanning Electron Microscopy setup

4.2.4 COLUMN WITH LENSES AND APERTURES

The electron beam is focused by the electro-magnetic lenses (condenser lens, scan coils, stigmator coils and objective lens) and the apertures in the column to a tiny sharp spot.

4.2.4.1 CONDENSER LENS

The current in the condenser determines the diameter of the beam: a low current result in a small diameter, a higher current in a larger beam. A narrow beam has the advantage that the resolution is better, but the disadvantage that the signal to noise ratio is worse. The situation is reversed when the beam has a large diameter. The condenser lens consists mostly out of two parts.

4.2.4.2 SCAN COILS

The scan coils deflect the electron beam over the object according to a zig-zag pattern. The formation of the image on the monitor occurs in synchrony with this scan movement. The scan velocity determines the refreshing rate on the screen and the amount of noise in the image (rapid scan = rapid refreshing = low signal = much noise; see SCANMODE in the virtual FESEM). The smaller the scanned region on the object, the larger the magnification becomes at a constant window size. Scan coils often consist of upper and lower coils, which prevent the formation of a circular shadow at low magnification.

4.2.4.3 THE OBJECTIVE LENS

The objective lens is the lowest lens in the column. The objective focuses the electron beam on the object (see FOCUS in the virtual FESEM). At a short working distance (= object in a higher position, that is closer to the objective lens) the objective lens needs to apply a greater force to deflect the electron beam. The shortest working distance produces the smallest beam diameter, the best resolution, but also the poorest depth of field. (The depth of field indicates which range in vertical direction in the object can still be visualized sharply).

4.2.4.4 THE STIGMATOR COILS

The stigmator coils are utilized to correct irregularities in the x and y deflection of the beam and hence to obtain a perfectly round-shaped beam. When the beam is not circular, but ellipsoidal, the image looks blurred and stretched (see ALIGN X Y in the virtual FESEM).

4.2.4.5 OBJECT CHAMBER

After the object has been covered by a conductive layer (see preparation) it is mounted on a special holder. The object is inserted through an exchange chamber into the high vacuum part of the microscope and anchored on a moveable stage. In the virtual FESEM the object can be moved in horizontal and vertical direction on the screen by operating the arrows in the POSITION box. In the real microscope the object can be repositioned in the chamber by means of a joy stick that steers in left right axis, or forward and backward. In addition, the object can be tilted (e.g. for stereo views), rotated and moved in Z direction (= closer or further away to the Objective lens). The “secondary electron emission” detector (scintillator) is located at the rear of the object holder in the chamber.

4.2.4.6 FORMATION OF THE IMAGE

When the primary probe bombards the object, secondary electrons are emitted from the object surface with a certain velocity that is determined by the levels and angles at the surface of the object. The secondary electrons, which are attracted by the Corona, strike the scintillator (fluorescing mirror) that produces photons. The location and intensity of illumination of the mirror vary depending on the properties of the secondary electrons. The signal produced by the scintillator is amplified and transduced to a video signal that is fed to a cathode ray tube in synchrony with the scan movement of the electron beam. The contrast in the ‘real time’ image that appears on the screen reflects the structure on the surface of the object. Parallel to the analog image, a digital image is generated which can be further processed.

Figure 4.10: Field Emission Scanning Electron Microscopy setup

4.3 HIGH RESOLUTION TRANSMISSION ELECTRON MICROSCOPE (HRTEM)

Transmission electron microscopy (TEM) is a microscopy technique whereby a beam of electrons is transmitted through an ultra thin specimen, interacting with the specimen as it passes through. An image is formed from the interaction of the electrons transmitted through the specimen; the image is magnified and focused onto an imaging device, such as a fluorescent screen, on a layer of photographic film, or to be detected by a sensor such as a CCD camera. TEMs are capable of imaging at a significantly higher resolution than light microscopes, owing to the small de Broglie wavelength of electrons.[4]

4.3.1 WORKING PRINCIPLE

The "Virtual Source" at the top represents the **electron gun**, producing a stream of monochromatic electrons. This stream is focused to a small, thin, coherent beam by the use of condenser lenses 1 and 2. The first **lens** (usually controlled by the "spot size knob") largely determines the "spot size"; the general size range of the final spot that strikes the sample. The second lens (usually controlled by the "intensity or brightness knob" actually changes the size of the spot on the sample; changing it from a wide dispersed spot to a pinpoint beam. The beam is restricted by the condenser **aperture** (usually user selectable), knocking out high angle electrons (those far from the optic axis, the dotted line down the center). The beam strikes the specimen and parts of it are transmitted. This transmitted portion is focused by the objective lens into an image. Optional Objective and Selected Area metal **apertures** can restrict the beam; the Objective aperture enhancing contrast by blocking out high-angle diffracted electrons, the Selected Area aperture enabling the user to examine the periodic diffraction of electrons by ordered arrangements of atoms in the sample. The image is passed down the column through the intermediate and projector lenses, being enlarged all the way. The image strikes the phosphor image screen and light is generated, allowing the user to see the image. The figure below shows a basic schematic diagram of a TEM.

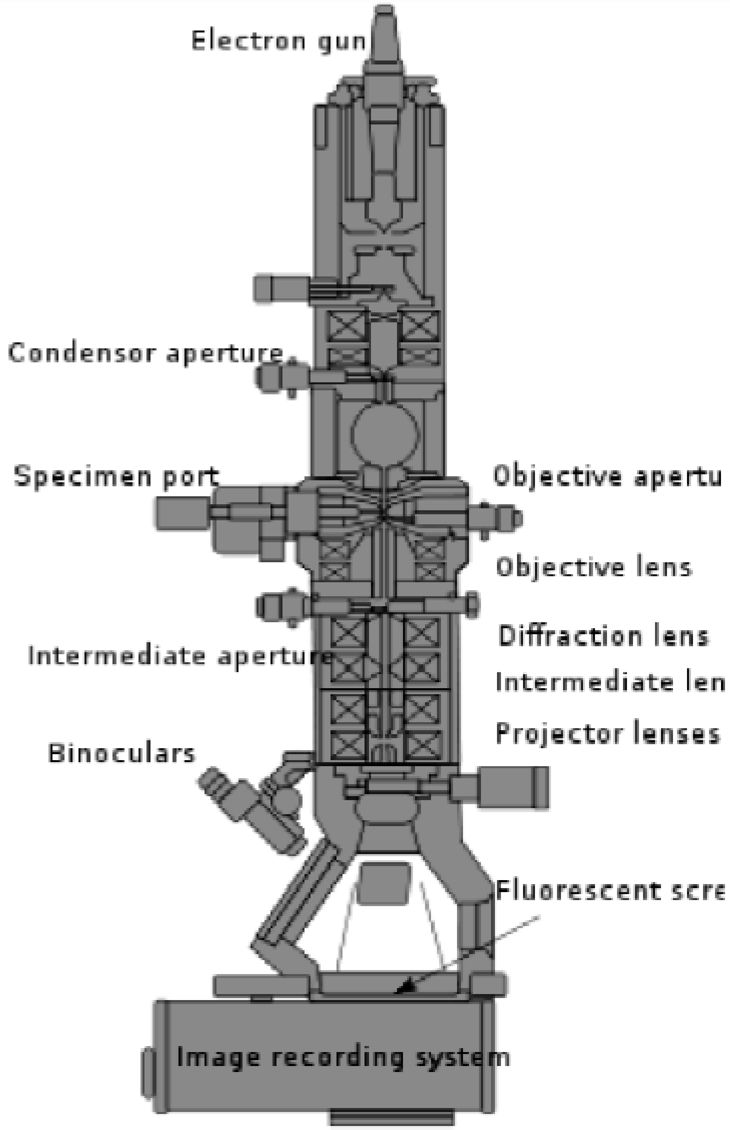

Figure 4.11: Schematic diagram of a TEM setup

4.3.2 LIMITATIONS ON SAMPLES

Sample preparation for TEM generally requires more time and experience than for most other characterization techniques. A TEM specimen must be approximately 1000 A_o or less in thickness in the area of interest. The entire specimen must fit into a 3 mm diameter cup and be less than about 100 microns in thickness. A thin, disc shaped sample with a hole in the middle, the edges of the hole being thin enough for TEM viewing, is typical. The initial disk is usually formed by cutting and grinding from bulk or thin film/substrate material, and the final thinning done by ion milling. Other specimen preparation possibilities include direct deposition onto a TEM-thin substrate (Si_3N_4, carbon); direct dispersion of powders on such a substrate; grinding and polishing using special devices like tripod; chemical etching and electro-polishing; and lithographic patterning of walls and pillars for cross-section viewing. A focused ion beam (FIB) may be used to make cross-sections.

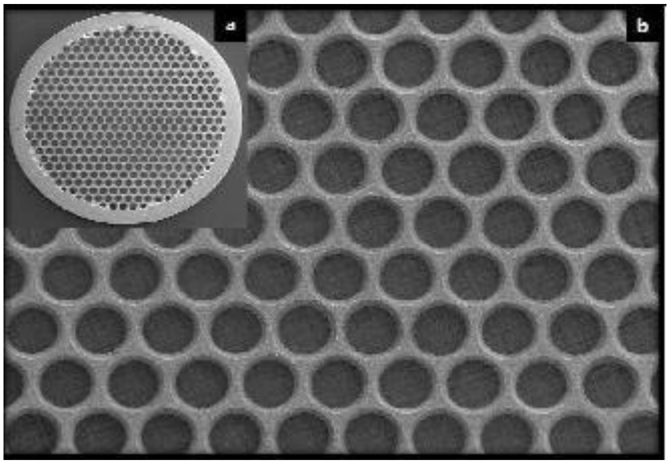

Figure 4.12: SEM image of the copper grid used for TEM sample preparation

4.3.3 APPLICATIONS OF TEM

4.3.3.1 STUDY OF MORPHOLOGY

The size, shape and arrangement of the particles which make up the specimen as well as their relationship to each other on a scale of atomic diameters can be studied, identified and visualized from a TEM micrograph.

4.3.3.2 CRYSTALLOGRAPHIC INFORMATION

The arrangement of atoms in the specimen and their degree of order, detection of atomic scale defects in areas a few nanometers in diameter. The lattice image of a sample can be obtained that shows the periodic arrangement of atoms in the 3-D space. The d- spacing can also be calculated from the lattice image of the samples.

4.3.3.3 COMPOSITIONAL INFORMATION

The elements and compounds, the sample is composed of and their relative ratios, in areas of a few nanometers in diameter can be studied using the EDAX attachment of TEM.

Figure 4.13: Transmission Electron Microscopy unit

4.4 FOURIER TRANSFORM INFRARED SPECTROSCOPY (FTIR)

Fourier Transform Infrared Spectroscopy (FTIR) is a technique which is used to analyze the chemical composition of any chemical species viz; organic chemicals, polymers, paints, coatings, adhesives, lubricants, semiconductor materials, coolants, gases, biological samples, inorganics and minerals. FTIR can be used to analyze a wide range of materials in bulk or thin films, liquids, solids, pastes, powders, fibers, and other forms. FTIR analysis can give not only qualitative (identification) analysis of materials, but with relevant standards, can be used for quantitative (amount) analysis. FTIR can be used to analyze samples up to ~11 millimeters in diameter, and either measure in bulk or the top ~1 micrometer layer. An FTIR Spectrometer is an instrument which acquires broadband NIR to FIR spectra. Unlike a dispersive instrument, i.e. grating monochromator or spectrograph, a FT-IR Spectrometer collects all wavelengths simultaneously. An FT-IR (Fourier Transform Infra-Red) is a method of obtaining infrared spectra by first collecting an interferogram of a sample signal using an interferometer, and then performing a Fourier Transform (FT) on the interferogram to obtain the spectrum. An FTIR Spectrometer collects and digitizes the interferogram, performs the FT function, and displays the spectrum.[5]

4.4.1 PRINCIPLE OF OPERATION

An FTIR is typically based on a Michelson Interferometer the interferometer consists of a beam splitter, a fixed mirror, and a mirror that translates back and forth, very precisely. The beam splitter is made of a special material that transmits half of the radiation striking it and reflects the other half. Radiation from the source strikes the beam splitter and separates into two beams. One beam is transmitted through the beam splitter to the fixed mirror and the second is reflected off the beam splitter to the moving mirror. The fixed and moving mirrors reflect the radiation back to the beam splitter. Again, half of this reflected radiation is transmitted and half is reflected at the beam splitter, resulting in one beam passing to the detector and the second back to the source. The schematic diagram of FTIR spectrometer is shown in the figure below.

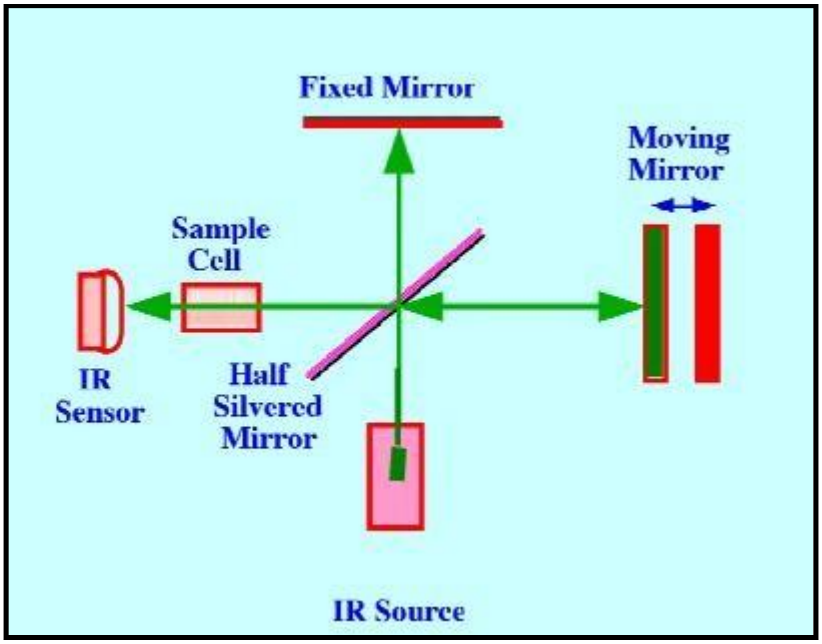

Figure 4.14: Schematic diagram of FTIR setup

A beam of infrared light (wavelength ~ 0.7-500 μm) is focused on the sample using all reflective optics. Depending on the sample composition, differing amounts of light are absorbed a different wavelengths. This pattern of light absorption is unique for almost every organic compound (except optical isomers) and many inorganic compounds. From the pattern of light absorbed, identification of the composition (qualitative analysis) can be made. With additional control over the sample thickness or sampling depth, the intensity of the individual absorbing components can be used to perform quantitative analysis (amount of each compound present). User-provided reference samples aid in positive substance identification and compositional verification. FTIR can be used to identify chemicals from spills, paints, polymers, coatings, drugs, and contaminants. FTIR is perhaps the most powerful tool for identifying types of chemical bonds (functional groups). The wavelength of light absorbed is characteristic of the chemical bond as can be seen in this annotated spectrum. A Shimadzu IR Prestige- 21 FTIR spectrometer is used to record the spectra in the mid IR region, (i.e. 400 – 4000 cm^{-1}) as shown in figure below.

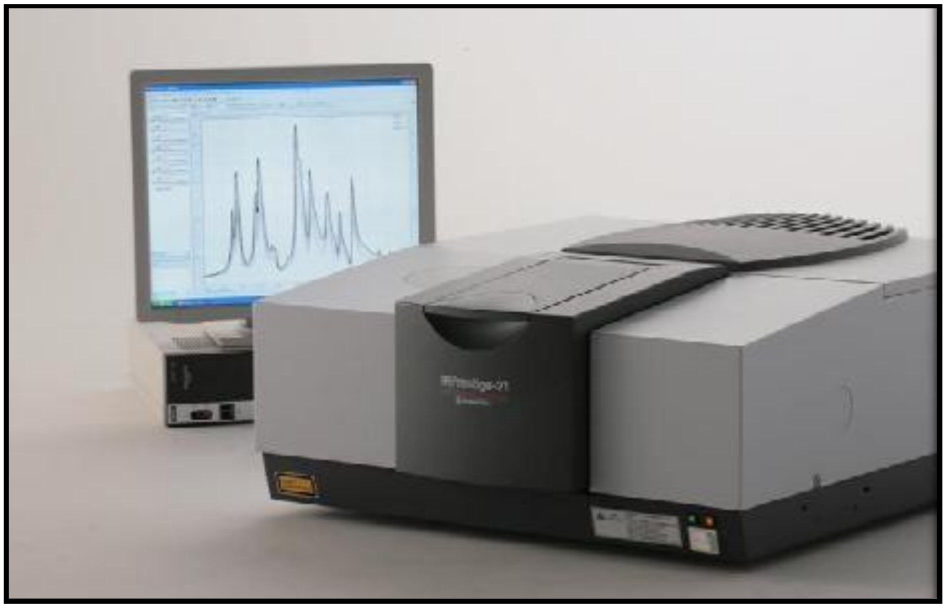

Figure 4.15: FTIR Setup

4.5 UV/VISIBLE SPECTROPHOTOMETER

Ultraviolet-visible spectroscopy or ultraviolet-visible spectrophotometry (UV/VIS) involves the spectroscopy of photons and spectrophotometry. It uses light in the visible and adjacent near ultraviolet (UV). In this region of energy space molecules undergo electronic transitions. Many molecules absorb ultraviolet or visible light. UV/Vis spectroscopy is mainly used in analytical chemistry for the quantitative determination of different analytes, such as transition metal ions, highly conjugated organic compounds, and biological macromolecules. It is also used in determination of bacterial cell concentration in a culture medium.[6]

Beer-Lambert law states that absorbance of a solution increases as attenuation of the beam increases. Absorbance is directly proportional to the path length ‘b’ and the concentration ‘c’ of the absorbing species.

$$A(\text{Absorbance}) = s\,b\,c \qquad (4.1)$$

where, ‘ε’ it the proportionality constant. Different molecules absorb radiation at different wavelengths. An absorption spectrum will show a number of absorption bands corresponding to structural groups within the molecule. For example, the absorption that is observed in the UV region for the carbonyl group in acetone is of the same wavelength as the absorption from the carbonyl group in diethyl ketone. Ultraviolet and visible radiations interact with matter which causes electronic transition of electrons from the ground state to excited state. The ultraviolet region falls in the range between 190-380nm whereas the visible region falls between 380-750nm. The amount of radiation absorbed may be measured in a number of ways:

Transmittance (T) = P/P_0,

% Transmittance (%T) = 100 T,

Absorbance (A) = $\log_{10}$

P/P_0 or, it can be written

as:

$A = \log_{10} 1/T$ (4.2)

or, $A = \log_{10} 100/ \%T$

or, $A = 2 – \log_{10} \%T$; (4.3)

The equation 4.3, $A = 2 – \log_{10} \%T$; allows us to easily calculate absorbance from percentage transmittance data. The relationship between absorbance and transmittance is illustrated in the following diagram:

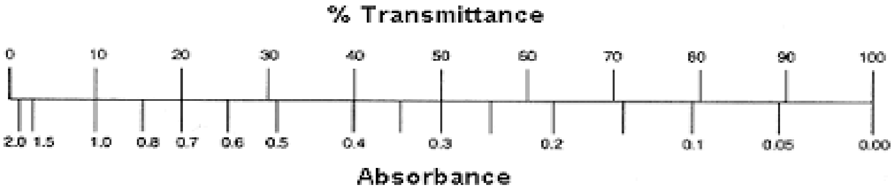

Figure 4.16: Relation between absorbance and % transmittance

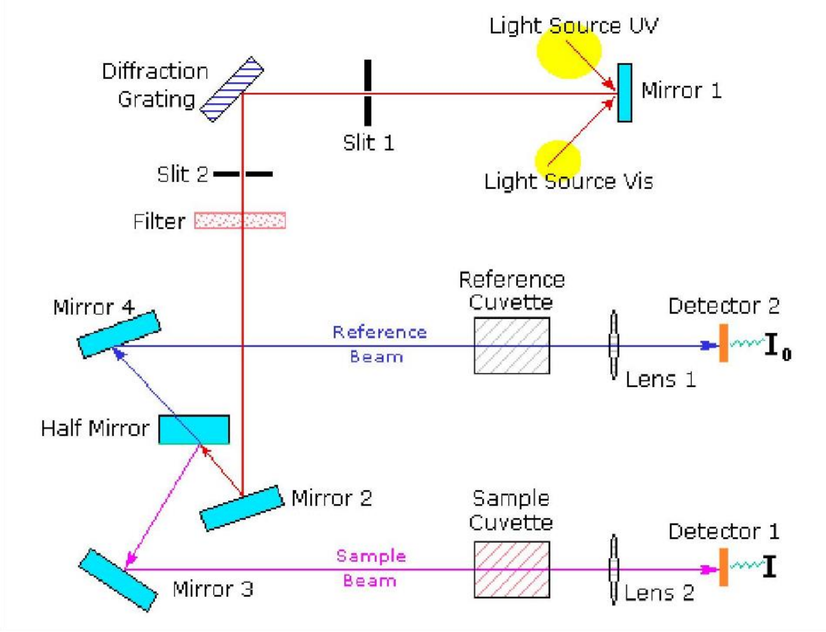

Figure 4.17: Schematic diagram of UV/Visible Spectrophotometer

Figure 4.18: JASCO V-650 UV/Visible Spectrophotometer

So, if all the light passes through a solution without any absorbance, then absorbance is zero, and percentage transmittance is 100%. If all the light is absorbed, then percentage transmittance is zero and absorbance is infinite. The schematic diagram of UV/Visible spectrophotometer is illustrated in fig 4.17.

The samples can be measured in two forms; liquid form in quartz cuvettes or as thin films in glass slides. The UV/Visible spectrophotometer can be used for a wide range of applications ranging from the calculation of the bandgap to study of adsorption or dye degradation experiment. The image of JASCO V-650 UV/Visible spectrophotometer is shown in fig 4.18.

4.6 SPECTROFLUOROMETER−PL (PHOTOLUMINESCENCE)

4.6.1 BASIC PRINCIPLE

Photoluminescence spectroscopy is a contactless, versatile, nondestructive, powerful optical method of probing the electronic structure of materials. Light is directed onto a sample, where it is absorbed and imparts excess energy into the material in a process called photo−excitation. One way this excess energy can be dissipated by the sample is through the emission of light, or luminescence. In the case of photo−excitation, this luminescence is called photoluminescence. Thus, photoluminescence is the spontaneous emission of light from a material under optical excitation. This light can be collected and analyzed spectrally, spatially and also temporally. The intensity and spectral content of this photoluminescence is a direct measure of various important material properties.

Photo excitation causes electrons within the material to move into permissible excited states. When these electrons return to their equilibrium states, the excess energy is released and may include the emission of light (a radiative process) or may not (a non radiative process) as shown in **fig. 4.19**. The energy of the emitted light (photoluminescence) relates to the difference in energy levels between the two electron states involved in the transition between the excited state and the equilibrium state. The quantity of the emitted light is related to the relative contribution of the radiative process. PL spectroscopy gives information only on the low lying energy levels of the investigated system. In semiconductor systems, the most common radiative transition is between states in the conduction and valence bands, with the energy difference being known as the bandgap. During a PL spectroscopy experiment, excitation is provided by laser light with an energy much larger than the optical band gap. The photo excited carriers consist of electrons and holes, which relax toward their respective band edges and recombine by emitting light at the energy of the band gap. Radiative transitions in semiconductors may also involve localized defects or impurity levels therefore the analysis of the PL spectrum leads to the identification of specific defects or impurities, and the magnitude of the PL signal allows determining their concentration. The respective rates of radiative and nonradiative recombination can be estimated from a careful analysis of the temperature variation of the PL intensity and PL decay time. At higher temperatures nonradiative recombination channels are activated and the PL intensity decreases exponentially. Thus photoluminescence is a process of photon excitation followed by photon emission and important for determining band gap, purity, crystalline quality and impurity defect levels of semiconducting material. It also helps to understand the underlying physics of the recombination mechanism.

PL spectrum is quite different from absorption spectrum in the sense that absorption spectrum measures transitions from the ground state to excited state, while photoluminescence deals with transitions from the excited state to the ground state. The period between absorption and emission is typically extremely short. An excitation spectrum is a graph of emission intensity versus excitation wavelength which looks very much like an absorption spectrum. The value of wavelength at which the molecules absorbs energy can be used as the excitation wavelength which provide a more intense emission at a red shifted wavelength, with a value usually twice of the excitation wavelength.

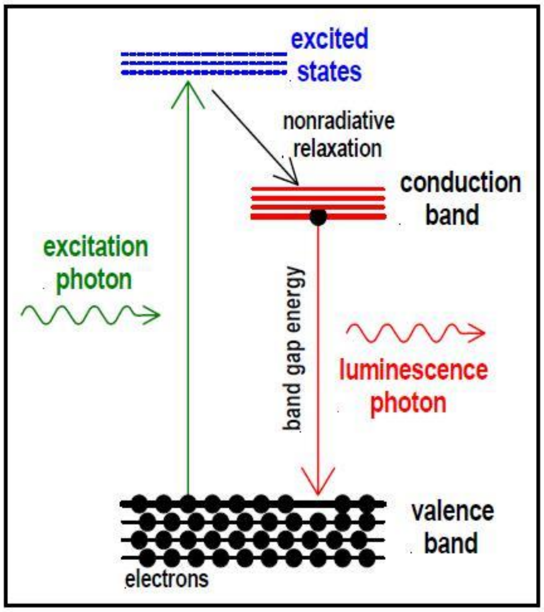

Figure. 4.19 Principle of photoluminescence spectroscopy (PL).

4.6.2 EXPERIMENTAL SET UP

A spectrofluorometer is an analytical instrument used to measure and record the fluorescence of a sample. While recording the fluorescence, the excitation, emission or both wavelength may be scanned. With additional accessories, variation of signal with time, temperature, concentration, polarization, or other variables may be monitored. **Fig. 4.20** shows the block diagram of fluorescence spectrometer. Fluorescence spectrometers use laser sources, which contains wavelength selectors, sample illumination, detectors and corrected spectra.

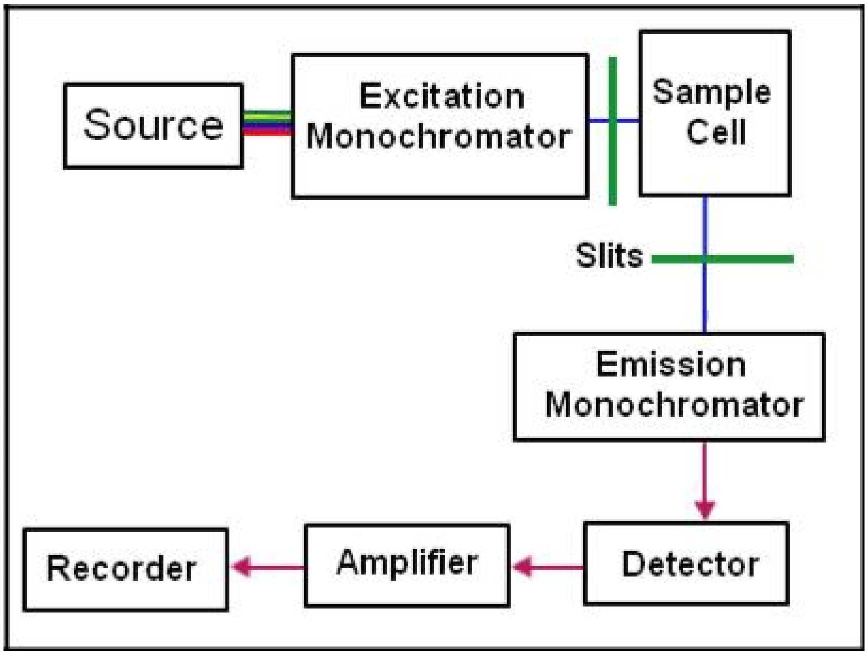

Figure. 4.20 Block diagram of fluorescence spectrometer.

Illuminator source:- The continuous light source is 150 W ozone free xenon arc lamp. Light from the lamp is collected by a diamond turned elliptical mirror, and then focused on the entrance slit of the excitation monochromator. The lamp housing is separated from the excitation monochromator by a quartz window. This vents heat out of the instrument, and protects against the unlikely occurrence of lamp failure. Resolution over the entire spectral range and minimize spherical aberrations and re diffraction.

Monochromators:- It contains two monochromators : Excitation monochromator and Emission monochromator. They use all reflective optics to maintain high resolution over the entire spectral range, and minimize spherical aberrations and re diffraction.

Gratings:- The essential part of a monochromator is a reflection grating. A grating disperses the incident light by means of its vertical grooves. A spectrum is obtained by rotating the gratings contain 1200 grooves mm^{-1}, and are blazed at 330 nm (excitation) at 500 nm (emission). Each grating is coated with MgF_2 for protection against oxidation.

Slits:- The entrance and exit ports of each monochromator have continuously adjustable slits. The width of the slits on the excitation monochromator determines the band pass of light incident on the sample. The emission monochromator's slits control the intensity of the fluorescence signal recorder by the signal detector. When setting slit width, the trade off is intensity of signal versus spectral resolution. The wider the slits are, the more light falls on the sample and detector, but the resolution decreases. The narrower slits are, the higher the resolution gets but at the expense of signal.

Shutters:- An excitation shutter is located just after the excitation monochromator's exit slit. The shutter protects sample from photo bleaching or photo degradation from prolonged exposure to the light source. An emission shutter is placed just before the emission monochromator's entrance and protects the detector from bright light.

Sample compartment:- The sample compartment accommodates various optional accessories, as well as fiber optic bundles to take the excitation beam to a remote sample and return the emission beam to the emission monochromator.

Detectors:- It contains two detectors: Signal detector and reference detector. The signal detector is a photon conting detector. This detector is an R928P photomultiplier tube, which sends the signal to a photon counting module. The reference detector monitors the xenon lamp, in order to correct for wavelength and time dependent output of the lamp. This detector is a UV enhance silicon photodiode, which is just before the sample compartment.

Computer Control:- The entire control of the FluoroMax−4 originates in your PC with our revolutionary new Fluor Essenc software and is transmitted through a serial link. On start up, the system automatically calibrates and presents itself for new experiments or stored routines instantly called from memory. **Fig.4.21** shows Experimental set up of Spectrofluorometer.

Figure. 4.21 Experimental set up of SHIMADZU RF−5301PC Spectrofluorometer.

4.7 RAMAN SPECTROSCOPY

4.7.1 BASIC PRINCIPLE

Raman spectroscopy is a useful technique for the identification of a wide range of substances–solids, liquids and gases. It is a straightforward, non destructive technique requiring no sample preparation. Raman spectroscopy involves illuminating a sample with monochromatic light and using a spectrometer to examine light scattered by the sample.

Raman spectroscopy is a spectroscopic technique based on inelastic scattering of monochromatic light, usually from a laser source. Inelastic scattering means that the frequency of photons in monochromatic light changes upon interaction with a sample. Photons of the laser light are absorbed by the sample and then reemitted. Frequency of the reemitted photons is shifted up or down in comparison with original monochromatic frequency, which is called the Raman effect. This shift provides information about vibrational, rotational and other low frequency transitions in molecules. This effect is based on molecular deformations in electric field E determined by molecular polarizability (α). The laser beam can be considered as an oscillating electromagnetic wave with electrical vector E. Upon interaction with the sample it induces electric dipole moment $P = \alpha E$ which deforms molecules. Because of periodical deformation, molecules start vibrating with characteristic frequency υ_m. Monochromatic laser light with frequency υ_o excites molecules and transforms them into oscillating dipoles. Such oscillating dipoles emit light of three different frequencies as shown in **fig. 4.22** when:

1. A molecule with no Raman active modes absorbs a photon with the frequency υ_o. The excited molecule returns back to the same basic vibrational state and emits light with the same frequency υ_o as an excitation source. This type of interaction is called an elastic Rayleigh scattering.

2. A photon with frequency is absorbed by Raman active molecule which at the time of interaction is in the basic vibrational state. Part of the photon's energy is transferred to the Raman active mode with frequency υ_m and the resulting frequency of scattered light is reduced to $\upsilon_o - \upsilon_m$. This Raman frequency is called Stokes frequency or just "Stokes".

3. A photon with frequency υ_o is absorbed by a Raman active molecule, which, at the time of interaction, is already in the excited vibrational state. Excessive energy of excited Raman active mode is released, molecule returns to the basic vibrational state and the resulting frequency of scattered light goes up to $\upsilon_o + \upsilon_m$. This Raman frequency is called Anti Stokes frequency or just "Anti Stokes''.

The Raman shift does not depend upon the frequency of the incident light but it is regarded as a characteristic of the substance causing Raman effect. For Stoke's lines, $\Delta\upsilon$ is positive and for anti stoke's lines $\Delta\upsilon$ is negative.

It can be noticed that the stokes and anti stokes lines are equally displaced from the Rayleigh line. This occurs because in either case one vibrational quantum of energy is gained or lost. Also, note that the anti stokes line is much less intense than the stokes line. This occurs because only molecules that are vibrationally excited prior to irradiation can give rise to the anti stokes line. Hence, in Raman spectroscopy, only the more intense stokes line is normally measured. Infrared absorption spectroscopy is another similar vibrational technique used to examine molecular structure but differs from Raman spectroscopy in the manner in which way the molecular transitions are taking place. For a transition to be Raman active there must be a change in the polarizability of the molecule during the vibration. This means that the electron cloud of the molecule must undergo positional change. On the other hand, for an Infrared detectable transition, the molecule must undergo dipole moment change during vibration. Homonuclear diatomic molecules such as H_2, N_2, O_2, etc. which do not show infrared spectra since they do not possess a permanent dipole moment do show Raman spectra since their vibration is accompanied by a change in polarizability of the molecule. Thus, Raman spectroscopy permits us to examine the vibrational spectra of compounds that do not lend themselves to IR absorption spectroscopy.

Raman spectroscopy can be used on liquids, solids and gases making it very versatile for studying various materials. Because of the distinct spectra that certain classes of materials give off, due to their structural arrangement, Raman spectroscopy can be used to determine the composition of unknown substances. This also makes Raman spectroscopy ideal for qualitative analysis of materials. In Raman spectroscopy no probe physically touches the material the laser light is the only thing to disturb the sample, this means that the material is not disturbed by the probe physically touching it and in some cases is the only way to accurately study a material.

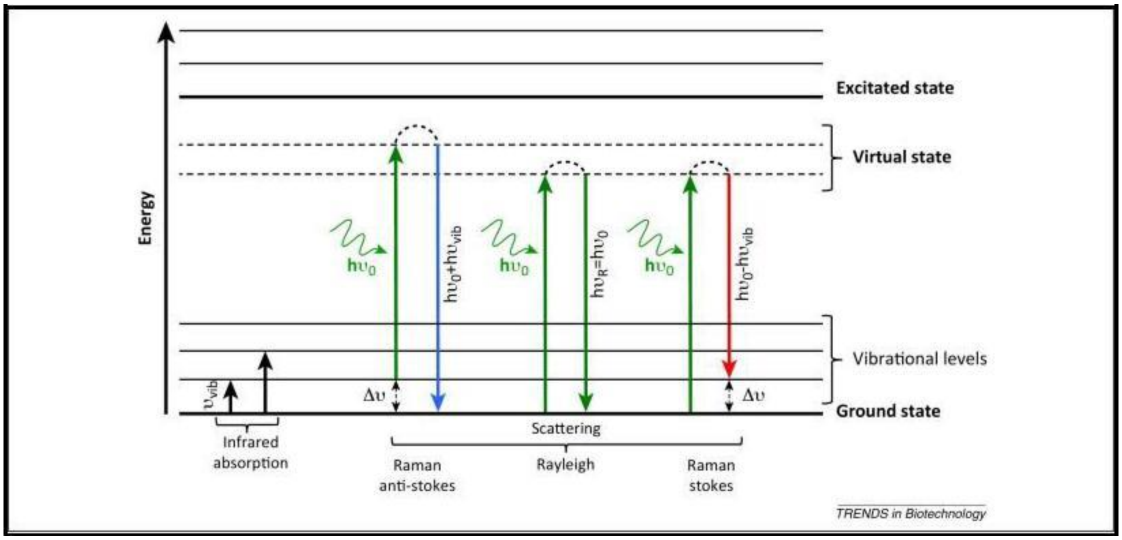

Figure. 4.22 Shows vibrational levels of the material

4.7.2 EXPERIMENTAL SET UP

A Raman system typically consists of four major components:

1. Excitation source (Laser).
2. Sample illumination system and light collection optics.
3. Wavelength selector (Filter or Spectrometer).
4. Detector (Photodiode array, CCD or PMT).

In Raman instrument a sample is illuminated with a laser beam. Light from the illuminated spot is collected with a lens and sent through interference filter or spectrometer to obtain Raman spectrum of a sample. Wavelengths close to the laser line, due to elastic Rayleigh scattering, are filtered out while the rest of the collected light is dispersed onto a detector. By changing the laser light you can confirm if a peak is a true Raman peak and not a peak just associated with the wavelength of the laser light that was used. Spontaneous Raman scattering signal is very weak because most of the incident photons undergo elastic Rayleigh scattering. Therefore special measures should be taken to distinguish it from the predominant Rayleigh scattering. Instruments such as notch filters, tunable filters, laser stop apertures, double and triple spectrometric systems are used to reduce Rayleigh scattering and obtain high quality Raman spectra.

In some instruments, sample is placed into the cryostat chamber where the low temperature is achieved by the use of liquid helium that cooled the cryostat. The cryostat is kept in vacuum so that laser light suffer no scattering from the particles of the air in the chamber. Before every measurement the scattered light would have to be aligned in the spectrometer so that maximum signal would hit the detector. This can be achieved by moving the sample to different positions and using lens, mirror system. In earlier times for taking Raman spectrum single point detectors such as photon counting Photomultiplier Tubes (PMT) was used. However, due to the consumption of very long time PMT is not preferred because it slow down any research or industrial activity based on Raman analytical technique. Nowadays, Raman spectroscopy has become even more accurate and easier due to advancements in optics, laser and computer technology. Researchers use multi channel detectors like Photo Diode Arrays (PDA) or, more commonly, a Charge Coupled Devices (CCD) to detect the Raman scattered light.

Charge Coupled Device (CCD) detectors have enormously helped the use of Raman spectroscopy by allowing scientist to take data quicker and with more precision that they were able to with the older photomultiplier tubes. The CCD has an array of detectors that can look at a range of wavelengths at one time greatly reducing the collection time. Sensitivity and performance of modern CCD detectors are rapidly improving. In many cases CCD is becoming the detector of choice for Raman spectroscopy[7-9].

Raman spectroscopy can be used on liquids, solids and gases making it very versatile for studying various materials. Because of the distinct spectra that certain classes of materials give off, due to their structural arrangement, Raman spectroscopy can be used to determine the composition of unknown substances. This also makes Raman spectroscopy ideal for qualitative analysis of materials. In Raman spectroscopy no probe physically touches the material the laser light is the only thing to disturb the sample, this means that the material is not disturbed by the probe physically touching it and in some cases is the only way to accurately study a material. Surface Enhanced Raman Spectroscopy (SERS) and Resonance Raman Effect (RRE) are different types of Raman spectroscopy. The goal of these two processes is to enhance the weak signal of the Raman spectra. Micro Raman spectroscopy (MRS) is another type of Raman spectroscopy and this process reduces the spot size of the light source on the sample, which is helpful if a small area of the sample is to be observed. It is also used to reduce damage or heating of the sample by the laser light[7-9]. The experimental set up of Raman Spectrometer is shown in the **fig. 4.24**

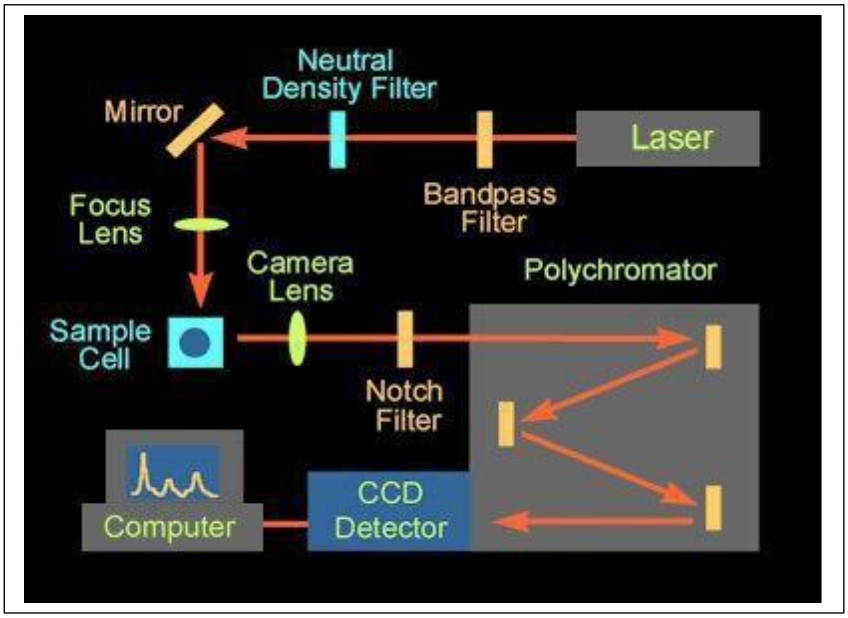

Figure 4.23: Schematic of Raman Spectrometer
4.24: Raman spectrometer Setup

REFERENCES

1. B.D. Cullity, 1978, Elements of X-ray diffraction, 2nd ed, Addison-Wesley, Reading.
2. J.Pawley, Scanning, 1997, **19**,324.
3. J.M. Huggett, H.F. Shaw, Clay minerals, 1997, **32**, 197.
4. Transmission Electron Microscopy; A textbook for materials science, D.B. Williams, C.B. Carter, 2009, **ISBN: 978-0-387-76500-6**.
5. J.S. Gaffney, N.A. Marley, D.E. Jones, 2012, **DOI: 10.1002/0471266965.com107.pub2**.
6. T. Owen, Fundamentals of UV/Visible spectroscopy: A Primer, 1988.
7. C. Kittel, Introduction to Solid State Physics (7th Ed.), John−Wiley and Sons (1995).
8. G. R. Chatwal, S. K. Anand, Instrumental methods of chemical analysis, Himalaya Publishing House (1979).
9. J. R. Ferraro, K. Nakamoto, C. W. Brown, Introductory Raman spectroscopy, Academic Press (2003).

CHAPTER 5

SYNTHESIS OF RUTILE TITANIUM DIOXIDE AND BASIC CHARACTERIZATION

5.1PREPARATION OF PURE TIO$_2$ NANOSTRUCTURES

All the reagents are of analytical grade and used without further purification. In a typical synthesis 2ml of Titanium(III) Chloride solution($TiCl_3$,Sigma-Aldrich) was added with 18ml of DI water while varying the concentration of sodium chloride (NaCl, Marck), as mentioned below. The solution was kept starring for 30 minutes at room temperature and then transferred to a Teflon lined sealed autoclave reactor. It was heated at 180°C for 6 hours and left to cool down. After cooling, the sample was collected and centrifuged at 4000rpm for 15 minutes and thoroughly washed using DI water and ethanol for multiple times. Sample thus obtained was dried inside a hot air oven at 80°C for 1 hour and collected.

Sl. No	Concentration of NaCl	Sample Code
1.	0M	S_{0M}
2.	0.5M	$S_{0.5M}$
3.	1M	S_{1M}
4.	3M	S_{3M}
5.	5M	S_{5M}

Table 5.1 Sample code of different TiO_2

After drying the samples, they showed distinct colour variation as shown in figure 5.1.

Figure 5.1 Colour variation of different samples of TiO_2

5.2 XRD ANALYSIS

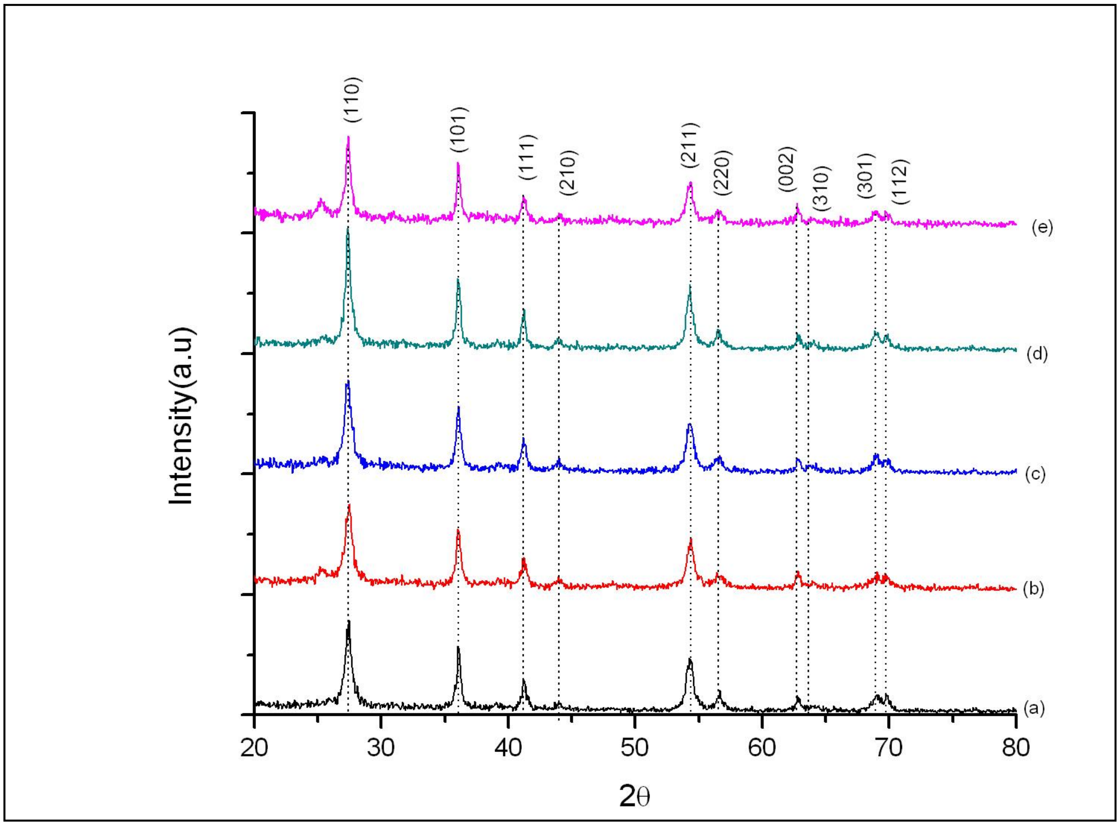

Figure 5.2: XRD Pattern of (a) S_{0M} (b) $S_{0.5M}$ (c) S_{1M} (d) S_{3M} (e) S_{5M} obtained from hydrothermal reaction by varying the concentration of NaCl

Figure 5.2shows the X-Ray Diffraction (XRD) pattern of the as synthesized sample, phase of which is confirmed as TiO2 Rutile, Tetragonal Primitive lattice (JCPDS Card Number 78-2485). Most intense diffraction peaks are detected at 27.44°, 36.10° and 54.32° which may be attributed to reflection from (110), (101) and (211) plane respectively whereas other peaks presented at 41.23°, 43.91°, 56.58°, 62.79°,63.90°,69.02° and 69.83° which are attributed from (111), (210), (220), (002), (310), (301) and (112) plane respectively.

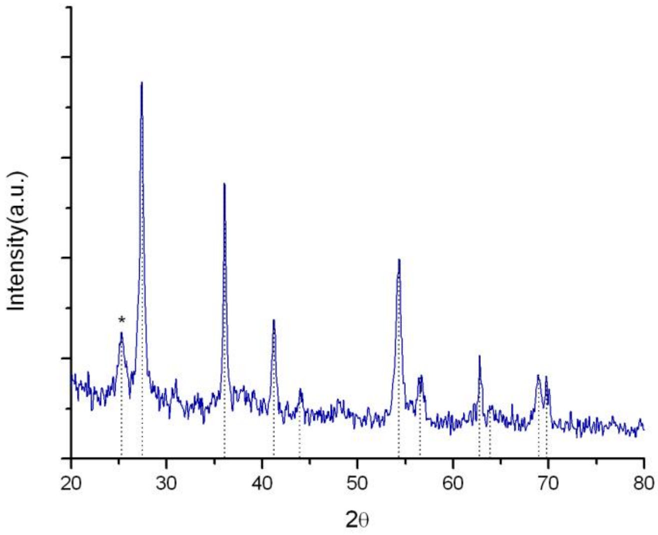

Figure 5.3:XRD Pattern of S_{5M}

Figure 5.3 represents the XRD Pattern of S_{5M} which contains one additional peak at 2θ=25.25°(marked using '*') which can be identified as $H_2Ti_8O_7$ (JCPDS Card Number 360656) has a negligible(<6%) contribution towards overall diffraction pattern.

5.2.1CALCULATION OF AVERAGE CRYSTALLITE SIZE

XRD pattern is one of the widely used technique to determine the average crystallite size. From the well-known Scherrer formula the average crystallite size, L, is:

$$L = \frac{0.9\lambda}{\beta \cos\theta} \ldots\ldots\ldots.(5.1)$$

where λ = wavelength of incident radiation, for Cu Kα radiation, $\lambda = 1.5404$ Å

β = Full width half maxima(FWHM) of XRD peak

The major problem with this calculation is the involvement of huge error. Using Modified Scherrer Equation[1] average crystallite size of the samples cab be calculated more accurately.

From equation (5.1)

$$L = \frac{0.9\lambda}{\beta \cos\theta}$$

$$\beta = \frac{0.9\lambda}{\mathrm{L}\cos\theta}$$

Taking $\log_e$ in both sides,

$$\ln\beta = \ln\frac{0.9\lambda}{\mathrm{L}\cos\theta}$$

$\ln\beta = \ln\frac{0.9\lambda}{L} + \ln\frac{1}{\cos\theta}$………………. (5.2)

Comparing this equation with $y = mx + c$, if we plot $\ln\beta$ vs $\ln\frac{1}{\cos\theta}$ then slope m=1 and intercept c= $\ln\frac{0.9\lambda}{L}$ and the graph will look like figure 5.4.

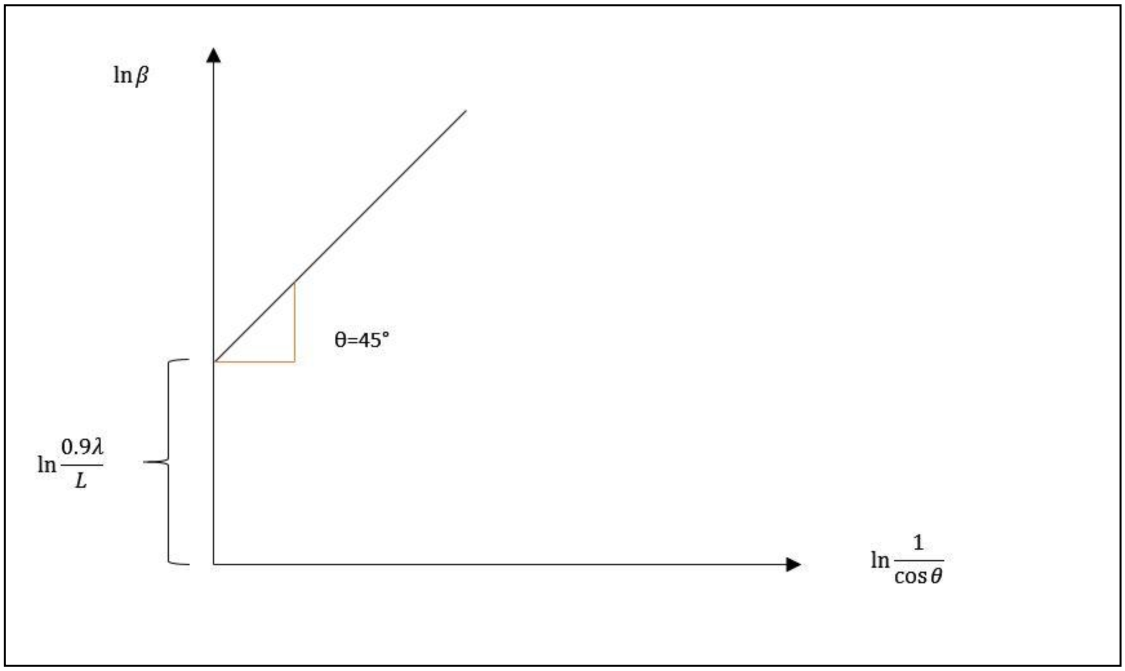

Figure 5.4: Modified Scherrer equation

Theoretically this straight line must be with a slope of 45° but, since errors are associated with experimental data, the least squares method gives the best slope and most accurate lnK/L. After getting the intercept, then the exponential of the intercept is obtained:

$$e^{\ln\frac{K\lambda}{L}} = \frac{K\lambda}{L} \text{……………}(5.3)$$

Having K = 0.9 a single value of L in nanometre can be calculated.

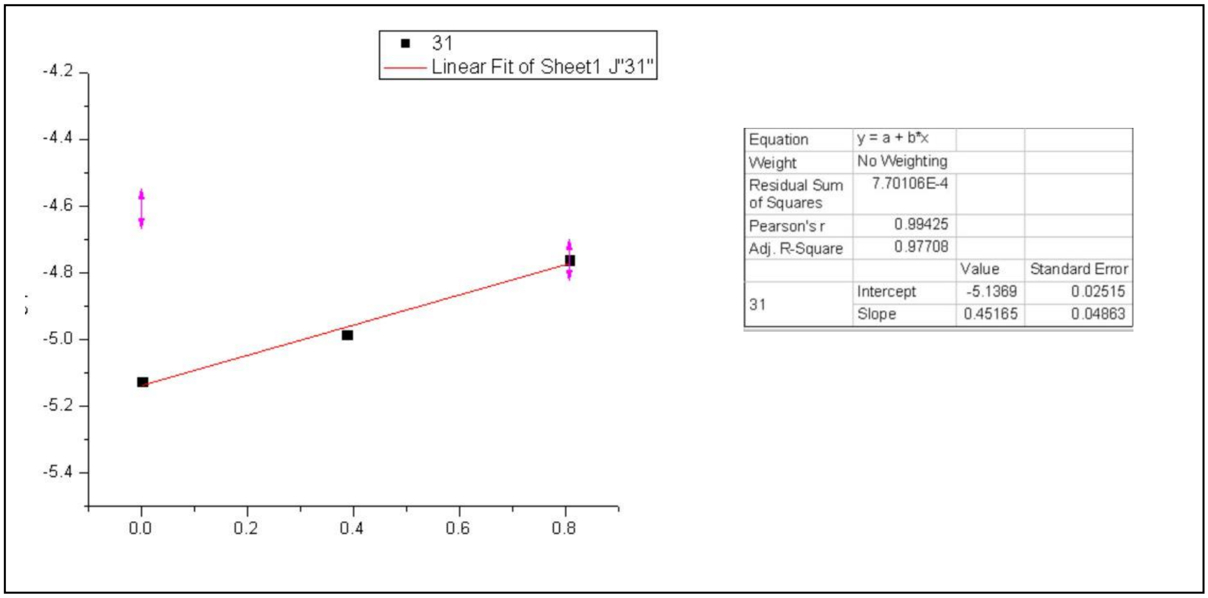

Equation	y = a + b*x		
Weight	No Weighting		
Residual Sum of Squares	7.70106E-4		
Pearson's r	0.99425		
Adj. R-Square	0.97708		
		Value	Standard Error
31	Intercept	-5.1369	0.02515
	Slope	0.45165	0.04863

Figure 5.5: Modified Scherrer equation linear fit

Applying the above-mentioned technique, we have calculated average crystallite size of as synthesized TiO_2.

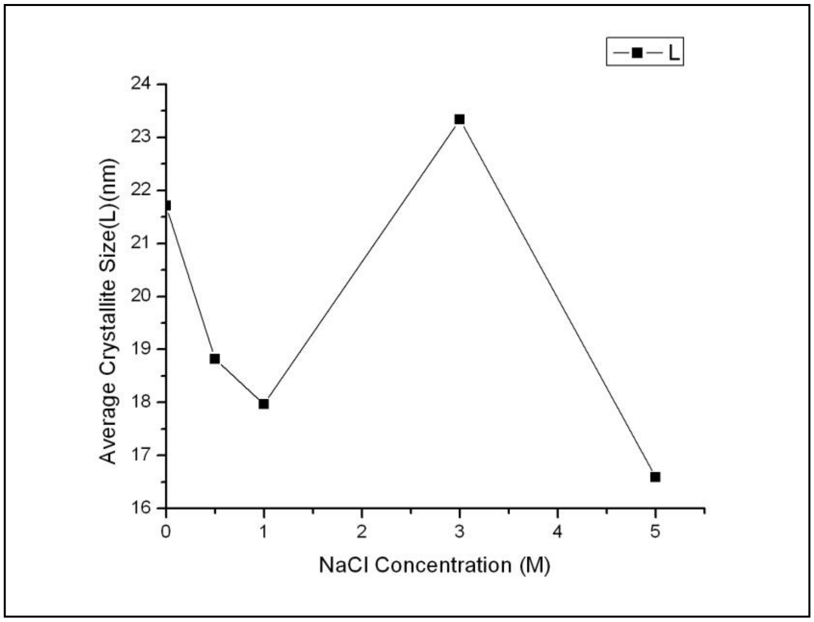

Figure 5.6: Variation of average crystallite size

Sl. No	Sample Code	Average Crystallite Size(nm)	Standard Deviation(nm)
1	S_{0M}	21.71	0.10593
2	$S_{0.5M}$	18.82	0.11338
3	S_{1M}	17.97	0.09788
4	S_{3M}	23.33	0.13372
5	S_{5M}	16.59	0.08768

Table 5.2 Variation of crystallite size of different TiO_2

From the table 5.2 it is clear that in the absence of NaCl average crystallite size is much higher(~22nm). In order to understand the phenomena, we must elaborately study the growth mechanism of as synthesized TiO_2.

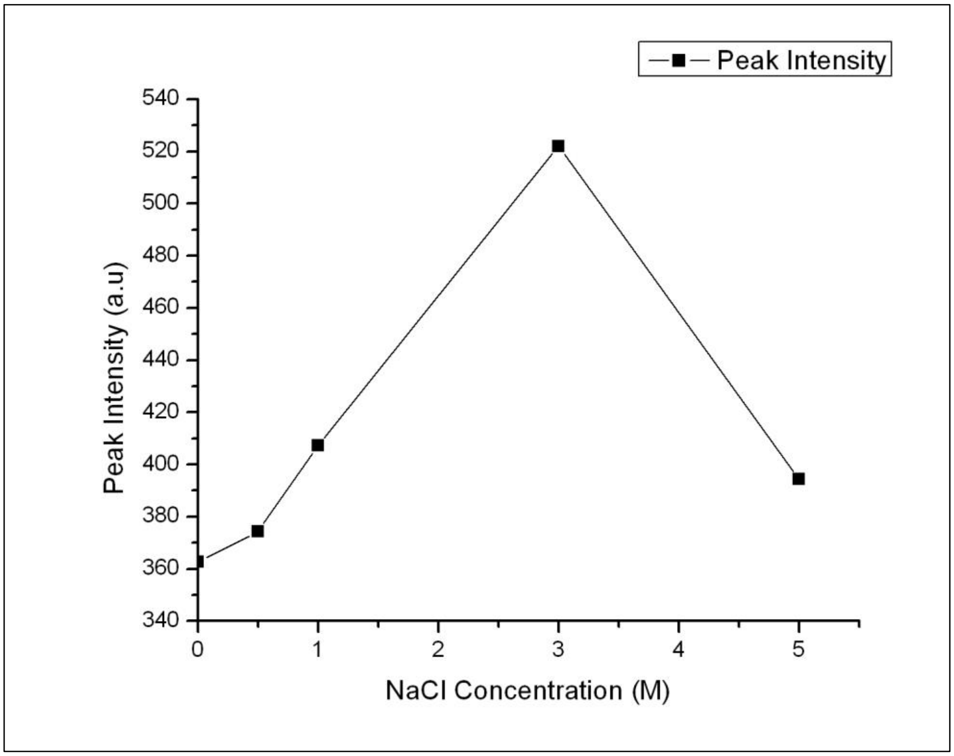

Figure 5.7: Variation of intensity of (110) peak

5.3FESEM ANALYSIS

FESEM or Field Effect Scanning Electron Microscopy Technique is used to visualize the microstructures and surface morphology of the as synthesized samples.

(a)

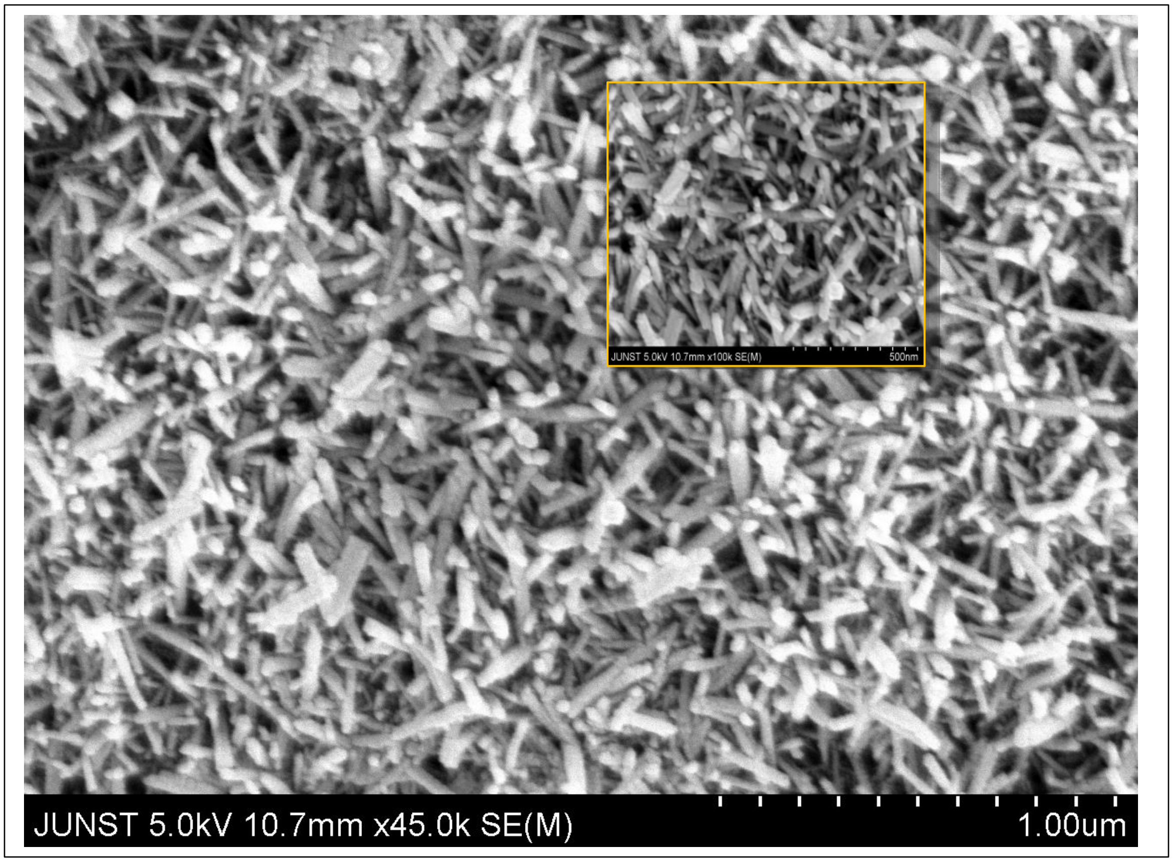

b(i)

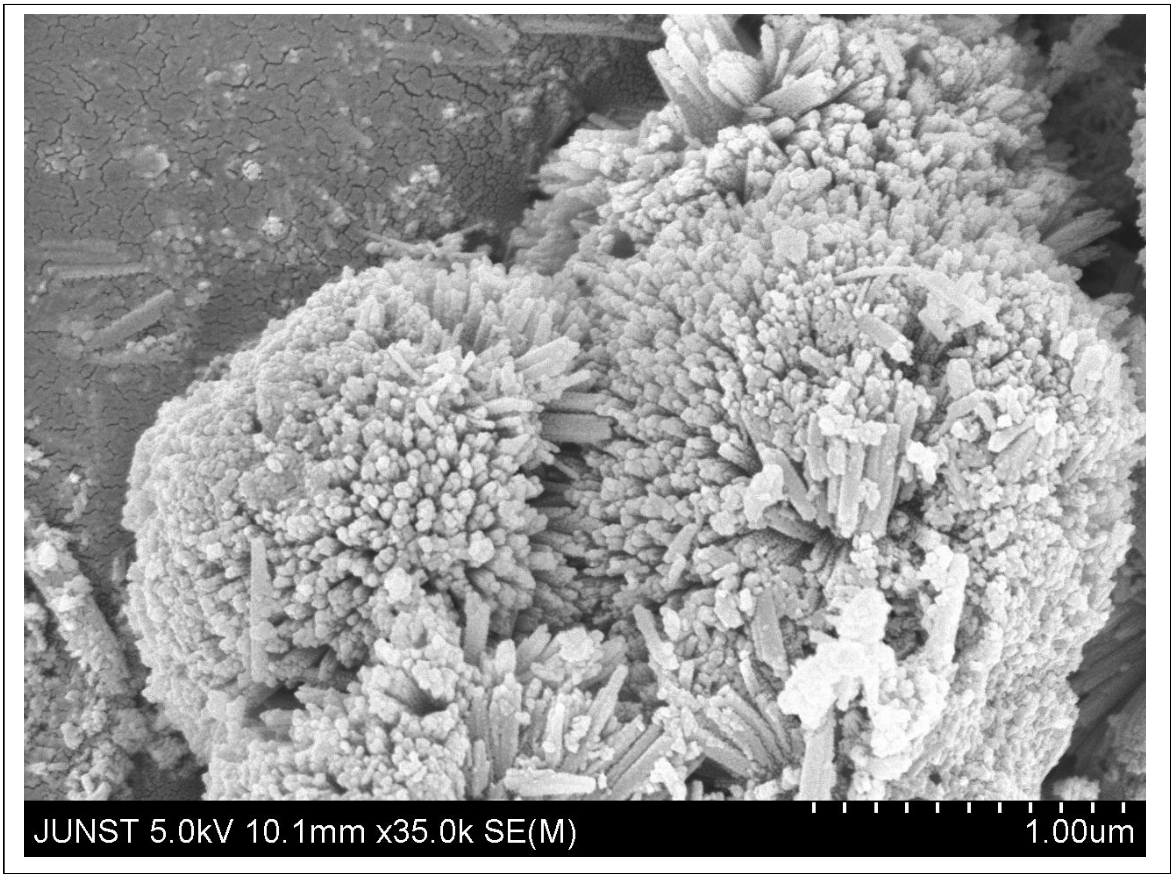
JUNST 5.0kV 10.1mm x35.0k SE(M)
1.00um

b(ii)

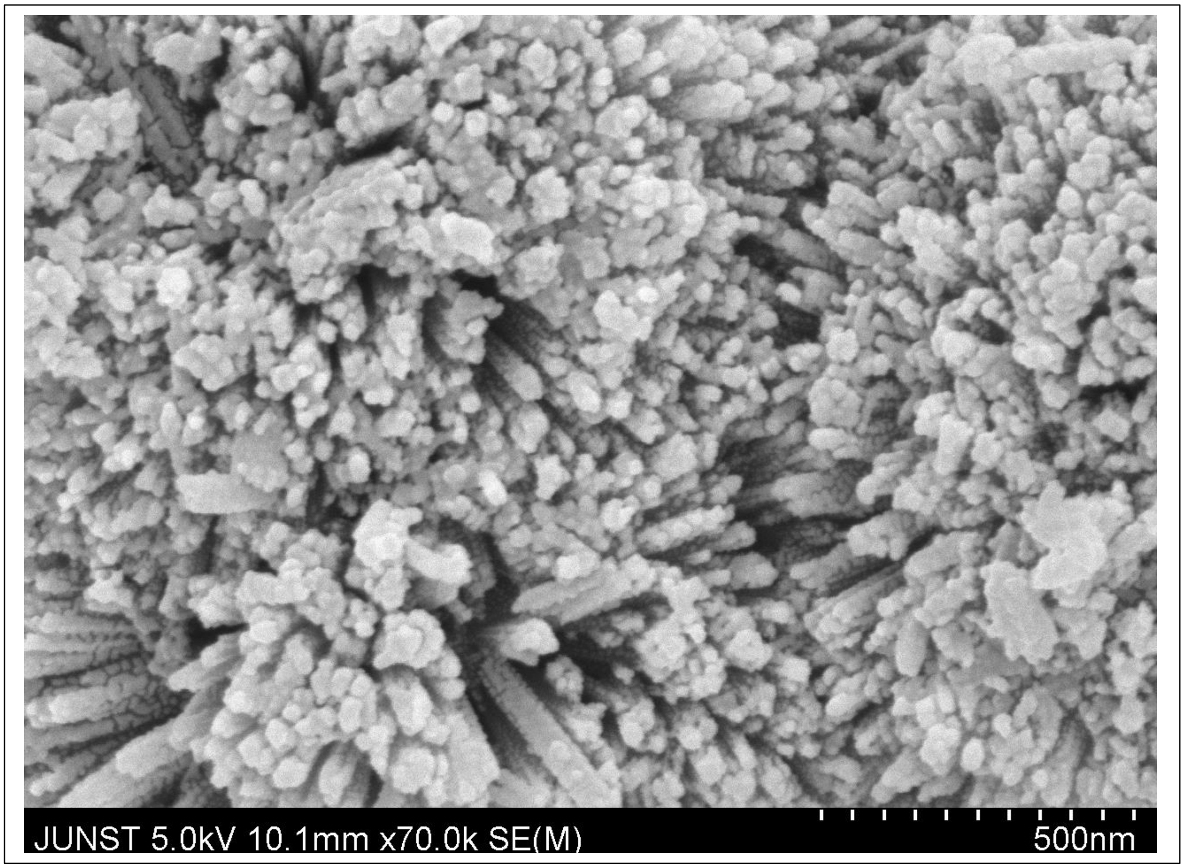
JUNST 5.0kV 10.1mm x70.0k SE(M)
500nm

c(i)

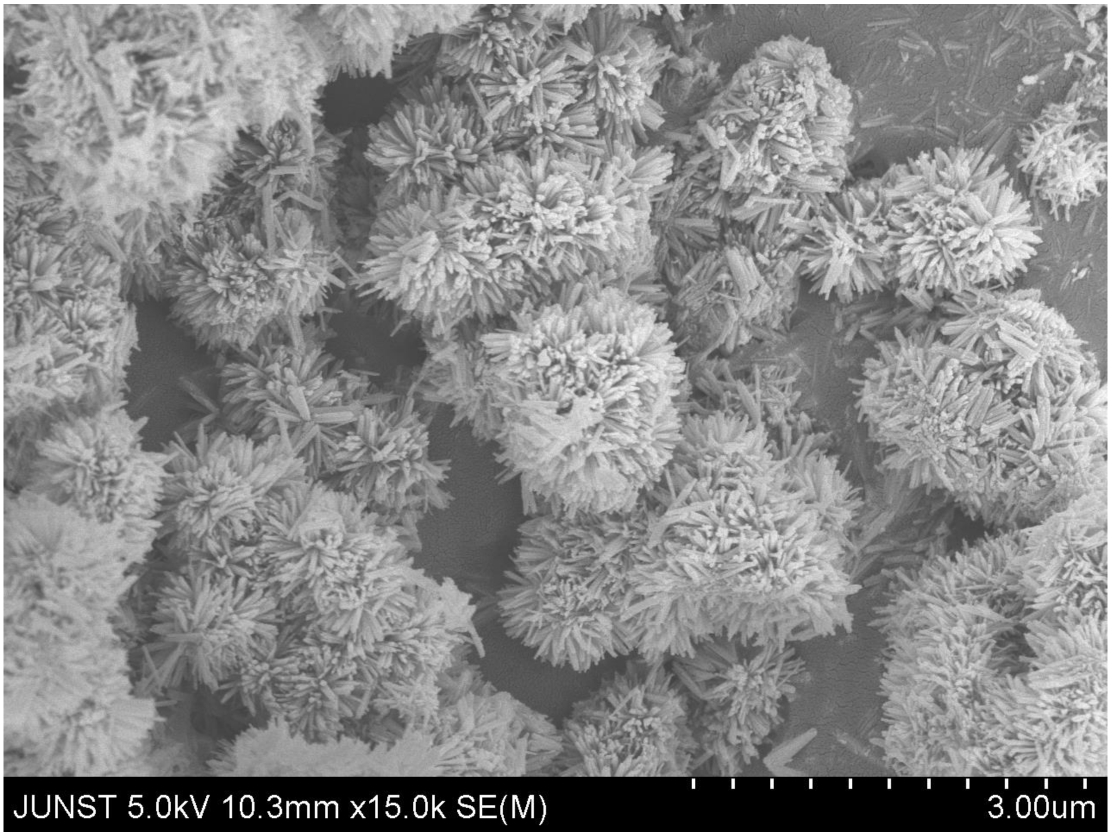
JUNST 5.0kV 10.3mm x15.0k SE(M)
3.00um

c(ii)

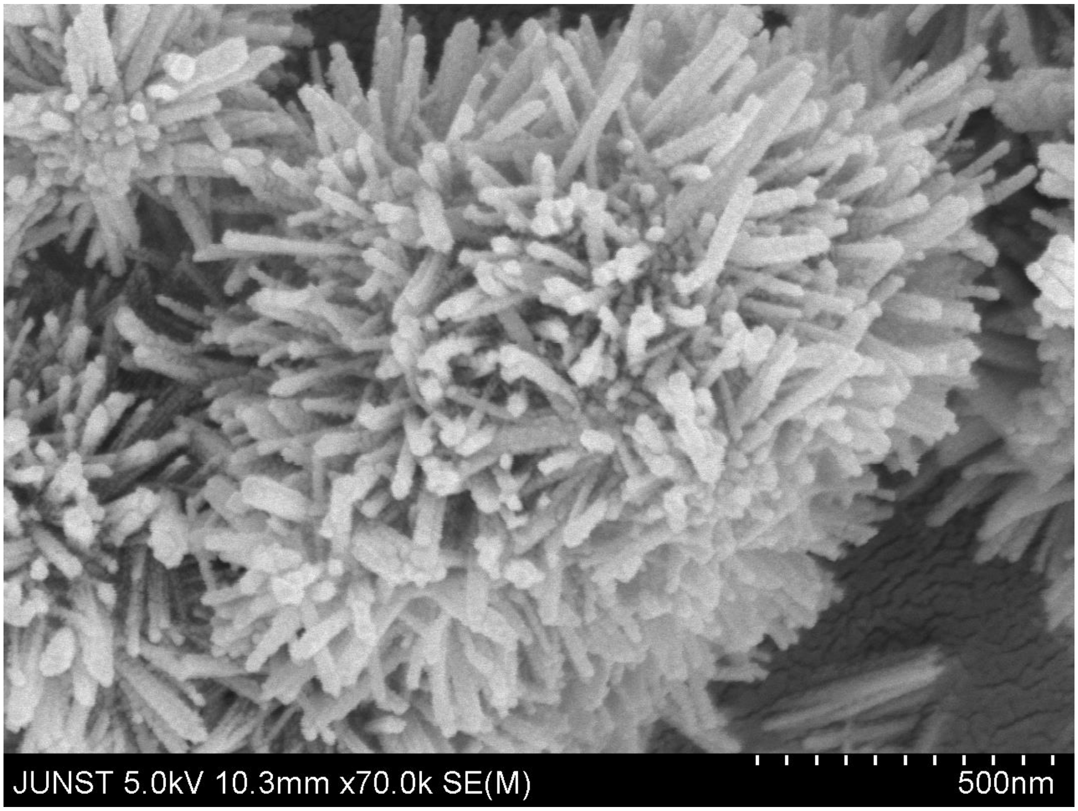
JUNST 5.0kV 10.3mm x70.0k SE(M)
500nm

c(iii)

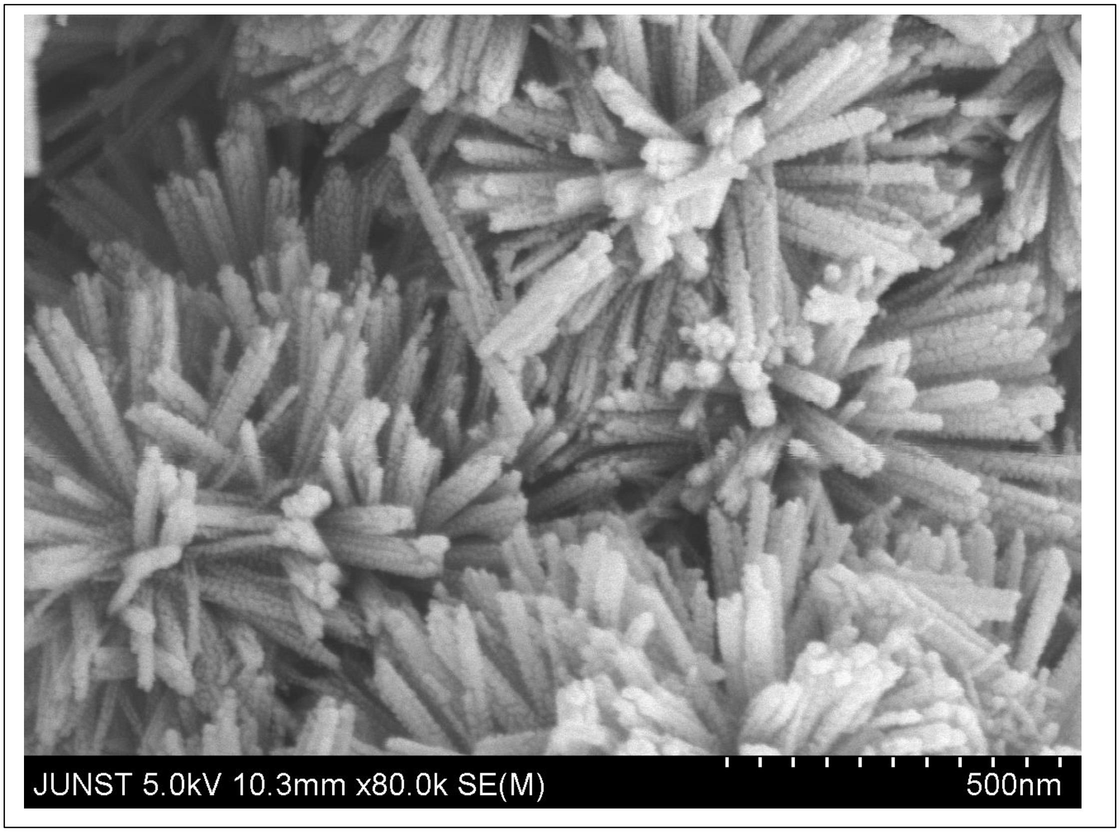
JUNST 5.0kV 10.3mm x80.0k SE(M)
500nm

c(iv)

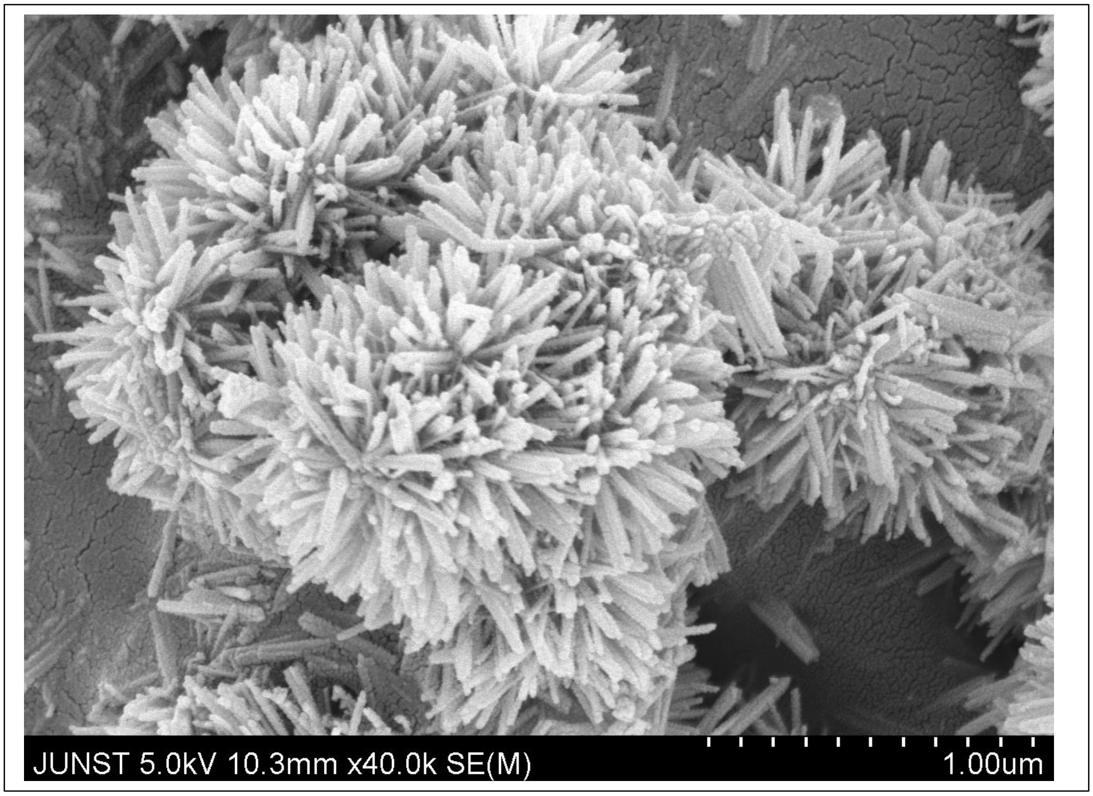
JUNST 5.0kV 10.3mm x40.0k SE(M)
1.00um

d(i)

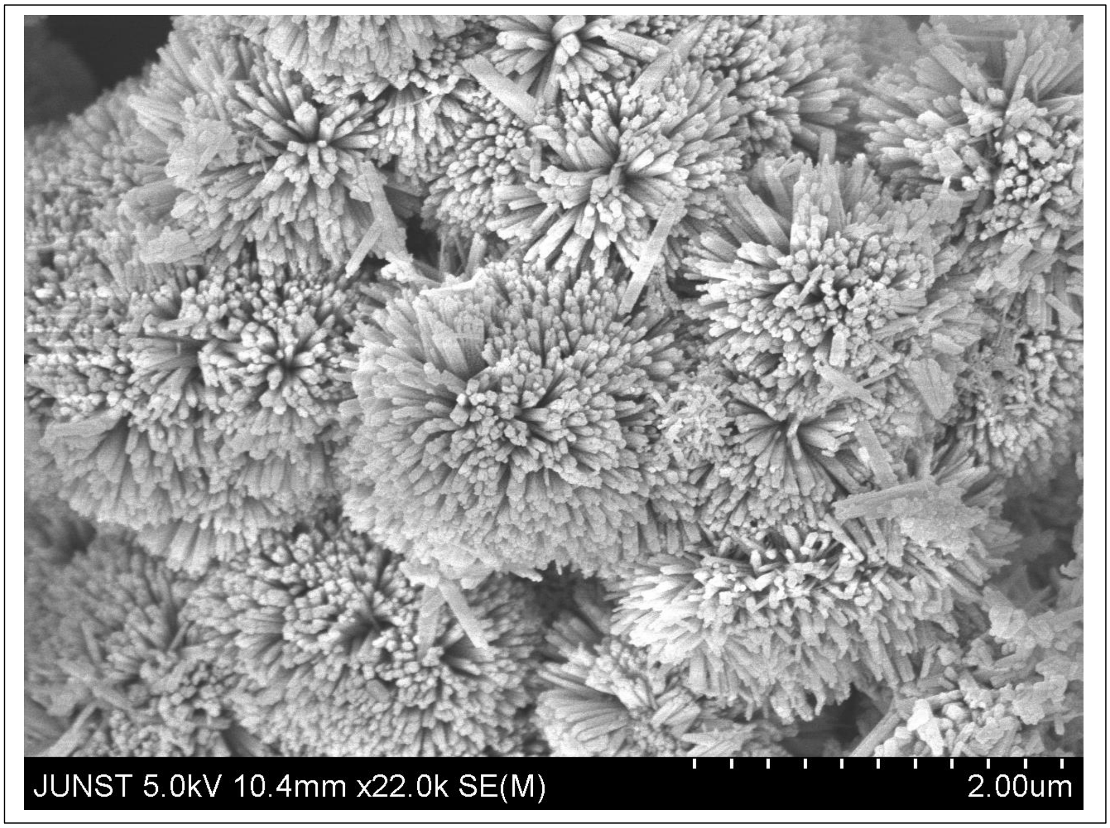
JUNST 5.0kV 10.4mm x22.0k SE(M)
2.00um

d(ii)

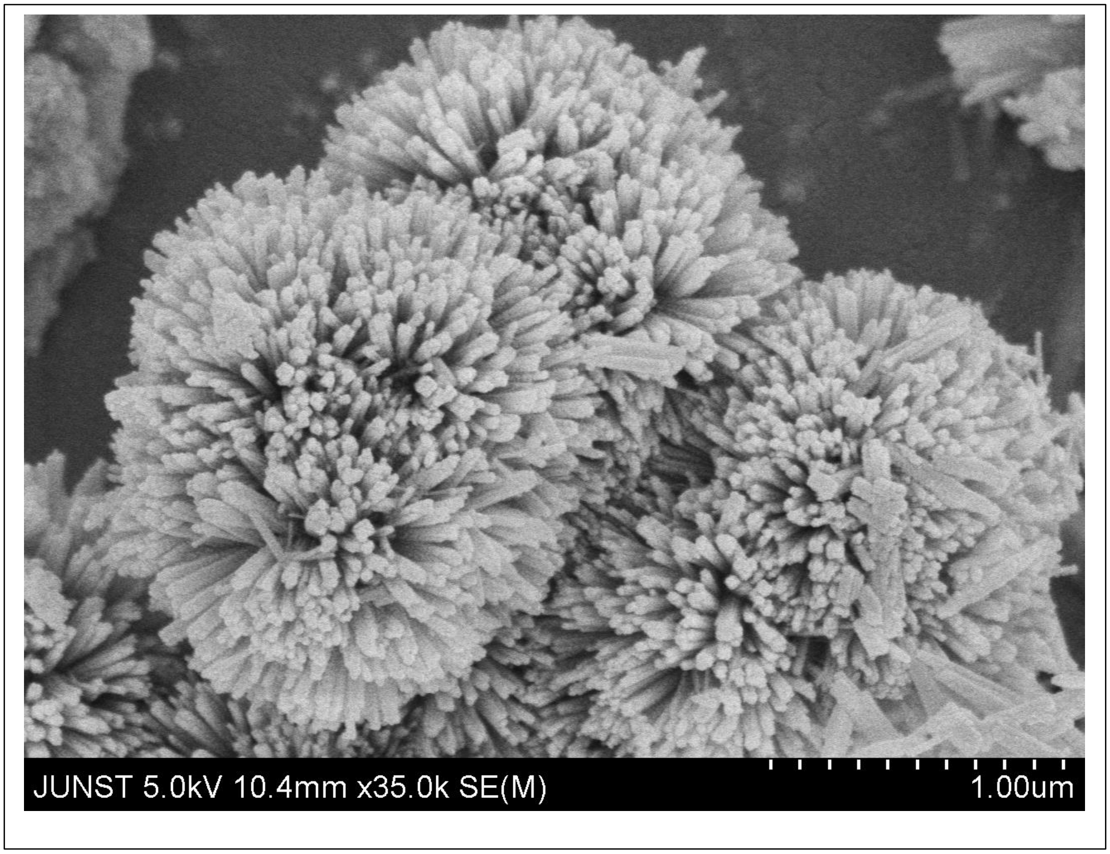
JUNST 5.0kV 10.4mm x35.0k SE(M)
1.00um

d(iii)

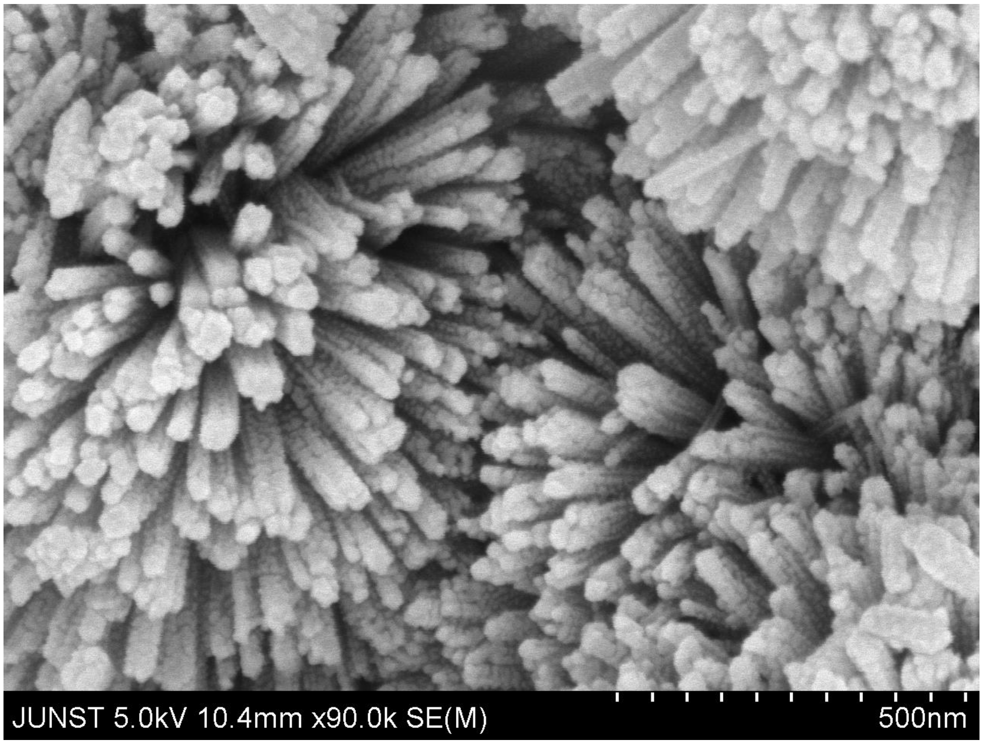
JUNST 5.0kV 10.4mm x90.0k SE(M)
500nm

d(iv)

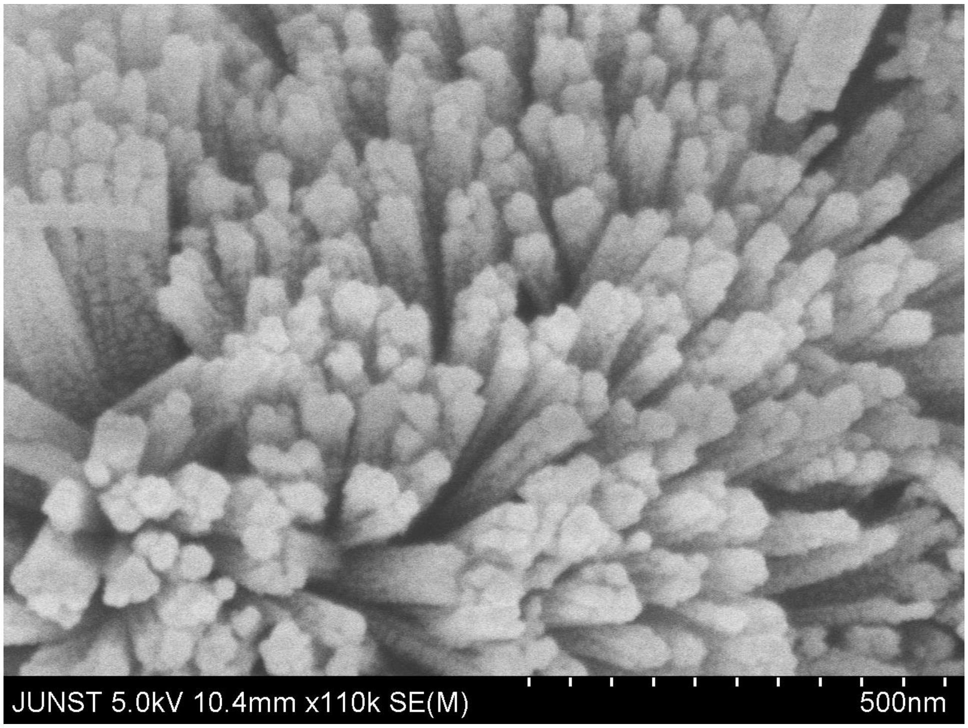
JUNST 5.0kV 10.4mm x110k SE(M)
500nm

e(i)

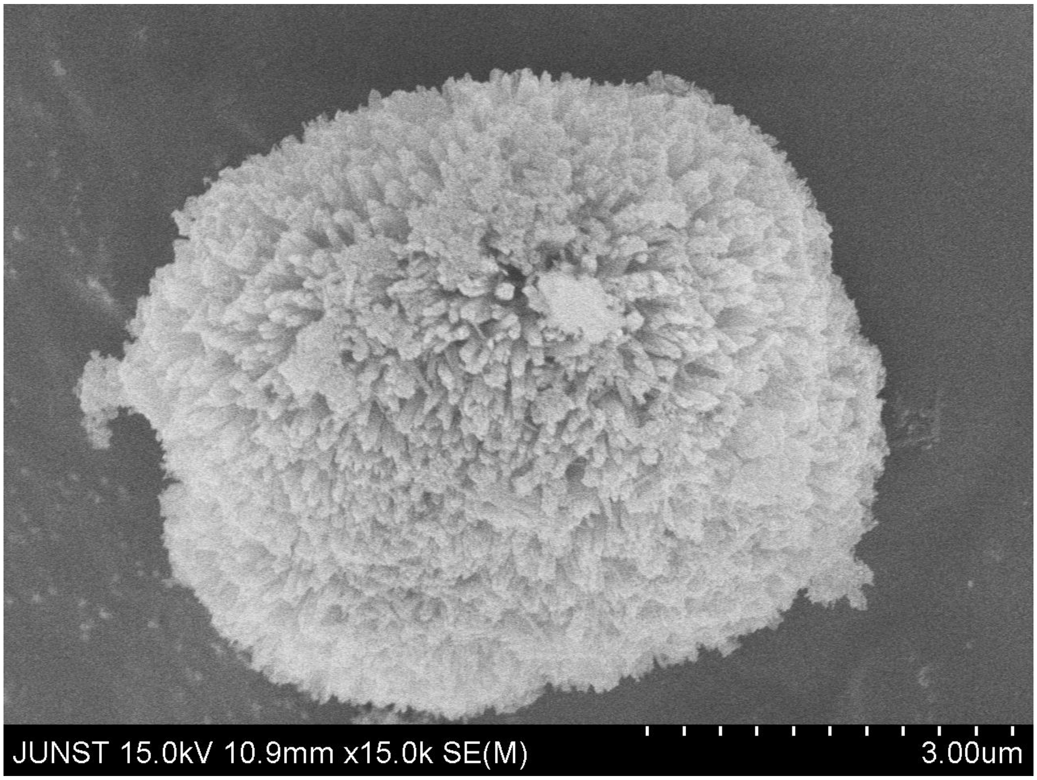
JUNST 15.0kV 10.9mm x15.0k SE(M)
3.00um

e(ii)

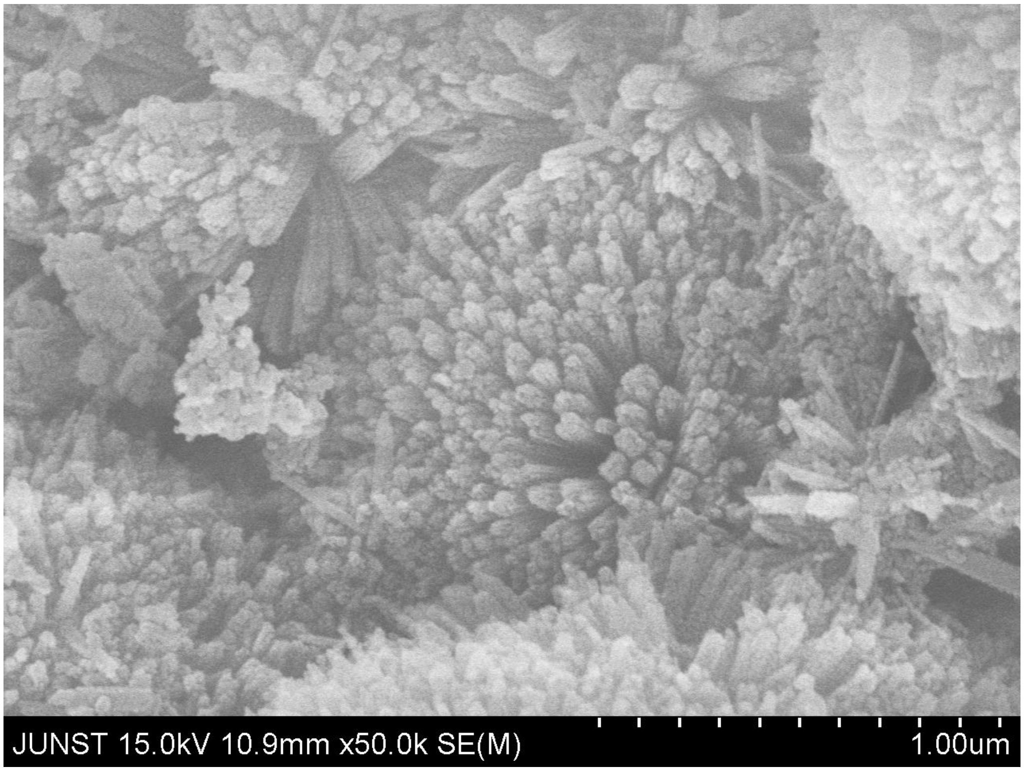
JUNST 15.0kV 10.9mm x50.0k SE(M)
1.00um

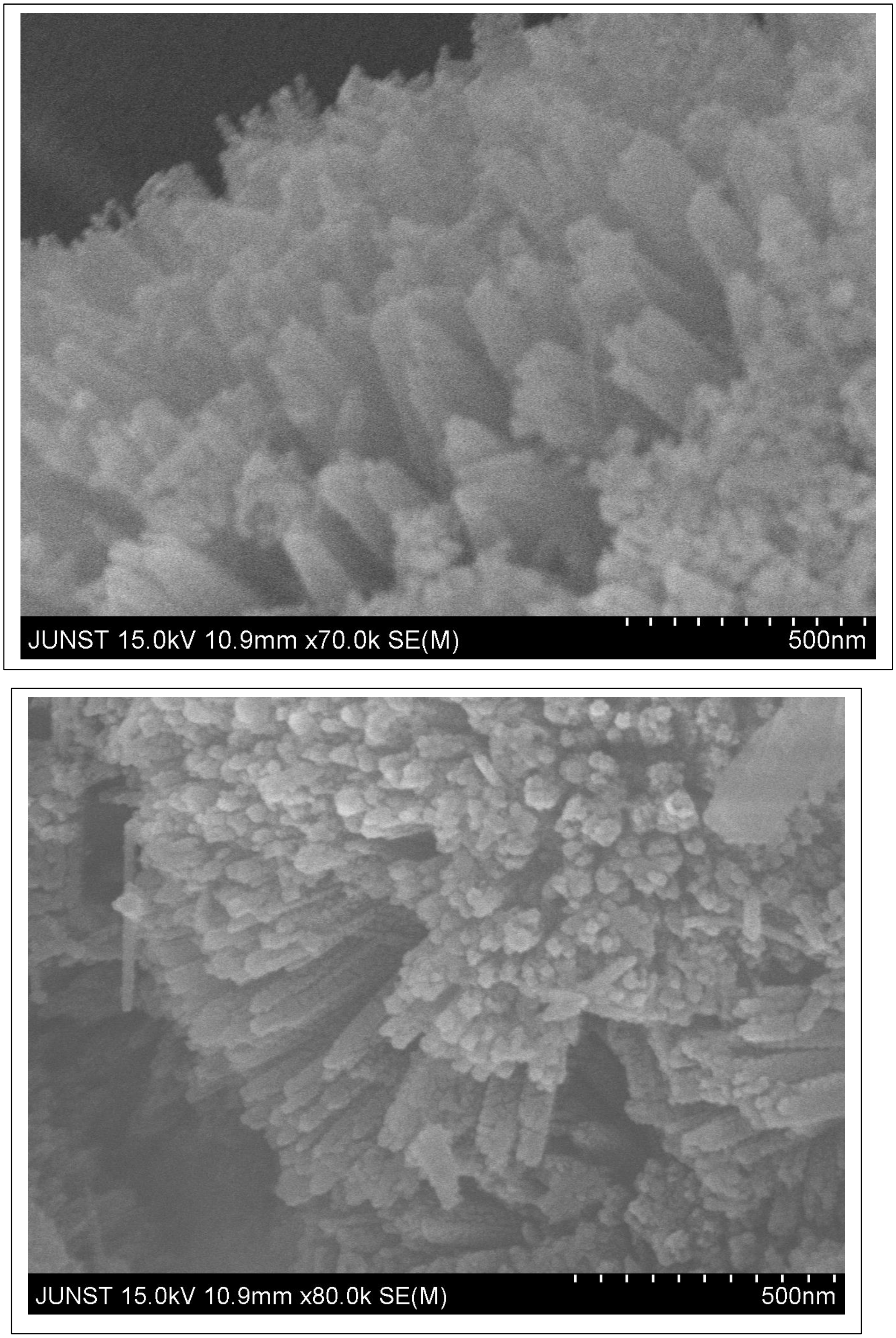

Figure 5.8: FESEM Images of (a) S_{0M} (b) $S_{0.5M}$ (c) S_{1M} (d) S_{3M} (e) S_{5M} obtained from hydrothermal reaction by varying the concentration of NaCl

From FESEM images as shown in it is clear that for S_{0M} no microstructure is obtained. For all other samples hierarchical nanoflower structure, comprises of nanorods is obtained.

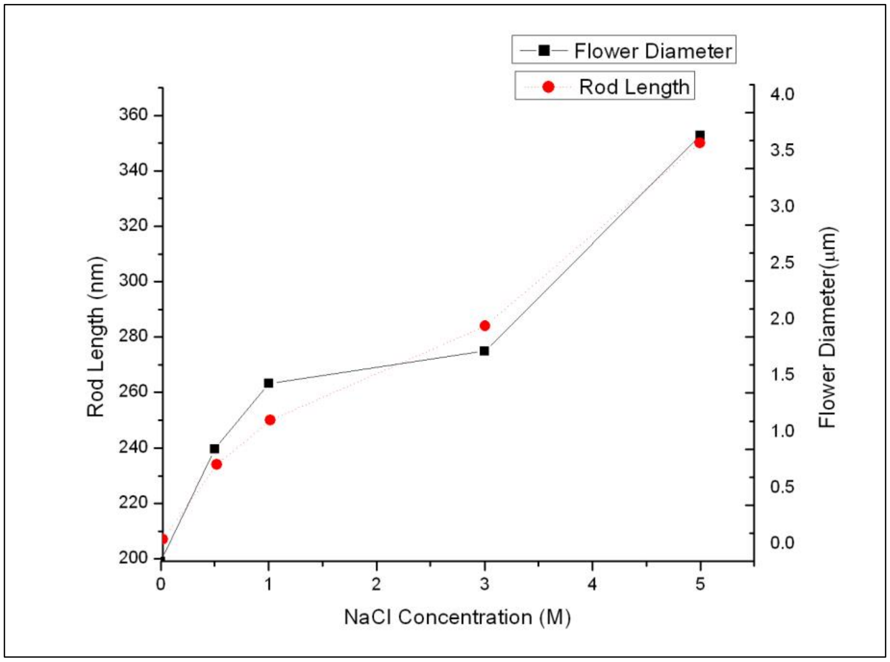

Figure 5.9: Variation of average rod length and flower diameter

From figure 5.9 it is clear that with increase in NaCl concentration, a consistent enhancement of nanorod length and hierarchical flower diameter is evident.

Sample Code	Nanorod Length(nm)	Flower Diameter(μm)
S_{0M}	207	0
$S_{0.5M}$	234	1
S_{1M}	250	1.584
S_{3M}	284	1.872
S_{5M}	350	3.8

Table 5.3 Variation of average nanorod length and flower diameter of different TiO_2

5.4HRTEM ANALYSIS

HRTEM or High-resolution transmission electron microscopy is used for better understanding of microstructure and experimentally find out the interplanar spacing. Since for all the samples, except S_{0M} microstructures are analogous to each other, as obtained from FESEM analysis, we have done HRTEM analysis of one typical sample (S_{3M}).

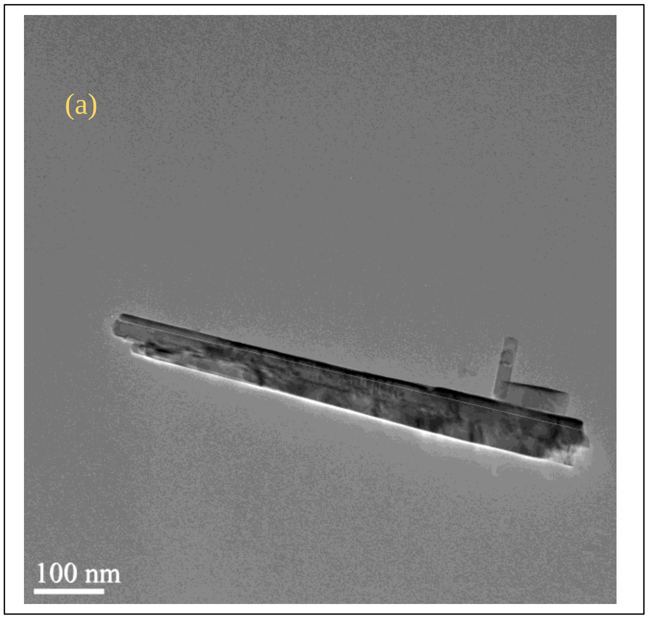

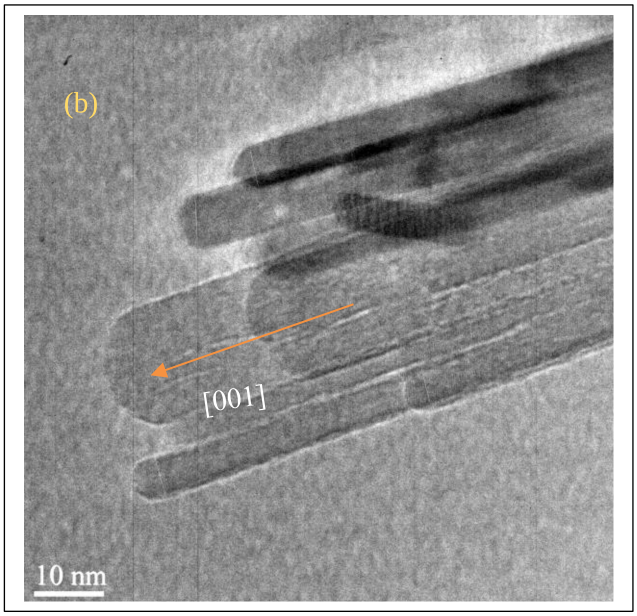

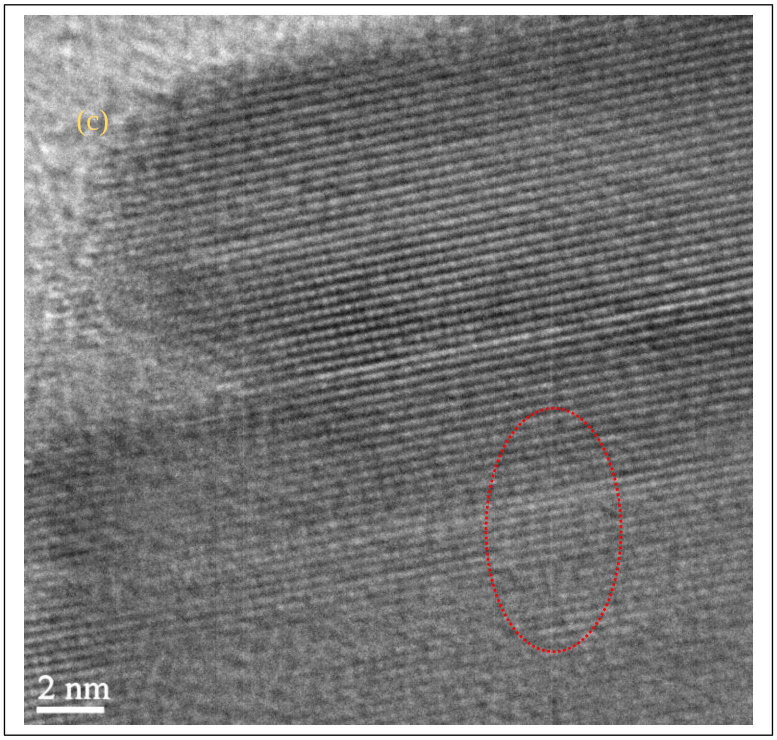

(d)

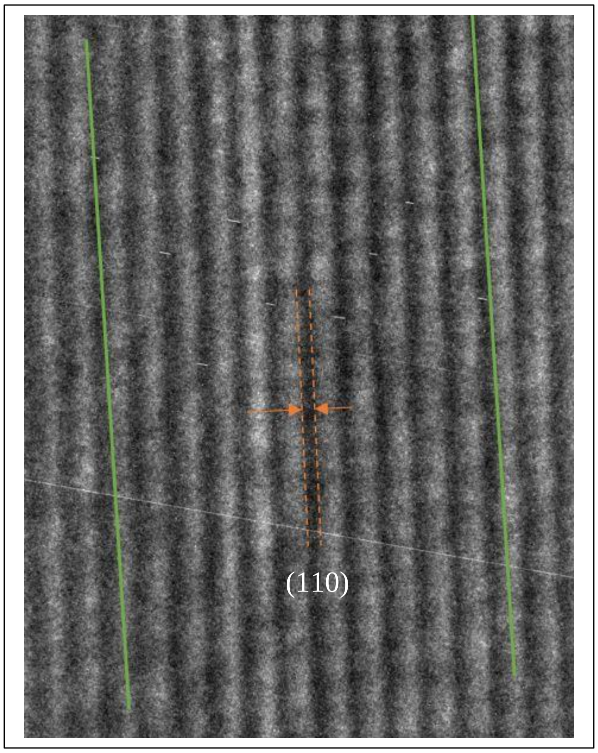

Figure 5.10: (a) single nanorod; (b) structure of tip; (c)&(d) fringe pattern for interplanar distance calculation

In figure 5.10(c) the region marked by red ellipse has been zoomed in figure 5.9(d). The measured d spacing between (110) planes of rutile TiO_2 is d_{110}=3.24Å, which is consistent with the previously reported data[2,3]. (110) plane is known to be thermodynamically most stable plane of rutile TiO_2[4,]

By using HRTEM analysis in figure 5.10(a) rod length for S_{3M} has been determined to be 683nm, which is much higher as measure from FESEM (table5.3) images. This is mainly because of the presence of agglomerated sample for FESEM analysis whereas TEM samples were dispersed into liquid medium.

Parameter measured	Measured value
Nanorod Length	683nm
Nanorod Diameter	5.748nm
Tip Diameter	6.7nm
d_{110}	3.24Å

Table 5.4 Parameters obtained from TEM Analysis

5.5POSSIBLE GROWTH MECHANISM OF TIO$_2$ HIERARCHICAL NANOSTRUCTURE

Development of any nano structure is broadly a two-step process, nucleation followed by growth. It depends on various factors of synthesis process such as precursor material, precursor concentration, pH, reaction temperature, stirring time etc.

Throughout our experiment we have varied concentration of one precursor (NaCl) by meticulously keeping another parameters constant.

According to previous reports NaCl plays very important role in the formation of TiO_2 nanostructures. Bae et al.[6] reported that with the variation of NaCl concentration from 1M to 5M larger and well dispersed nanorods has been achieved. Average crystallite size varies from 66-97.20nm. In his work Bai et al.[7] varied NaCl concentration from 7M to 11M and both size and packing of dandelions increases. Size varies from hundreds of micrometers to few nanometers. Cassaignon et al.[8] in his work used HCl instead of NaCl and explained that if the pH of the solution pH<1 then only rutile is formed. For pH 2.5-4.5 again rutile is main phase with pure rutile in pH=4. He termed this as “soft condition” for rutile synthesis and the particles thus obtained are of rod like structures. Hosono et al.[3] reported same synthesis as ours but with a higher concentration of NaCl(10M) and obtained parallelepiped rutile TiO_2 microstructures with length 3-4μm and width 150-250 nm.

According to the classical nucleation theory, when the solubility exceeds the equilibrium value, the precursor(solute) forms a new solid phase to reduce overall Gibb's free energy(ΔG_v) of the system following the thermodynamic law,

$\Delta G_v = -(\frac{kT}{\Omega}) \ln(1+\sigma)$ ……………..(5.4)

where σ represents the level of supersaturation and Ω represents atomic volume.

Due to formation of new solid phase overall Gibb's free energy can be given by,

$\Delta G = (\frac{4}{3}\pi r^3 \Delta G_v + 4\pi r^2 \gamma)$…………….(5.5)

Using the concept of maxima-minima analysis, if minimum critical radius be (r*) and minimum critical free energy be (ΔG_v*) then,

$\Delta G_v^* = {16(16\pi\gamma)}/{(3\Delta G_v)^2}$ …………….(5.6)

From equation(5.6) it is clear that with increase in successful nucleation ΔG_v* reduces due to enhancement of ΔG_v , making the system thermodynamically stable.

In the absence of NaCl, $TiCl_3$ can also be converted into TiO_2 in aqueous medium following the given chemical reaction by the anodic oxidative hydrolysis[3]

$Ti^{3+} + H_2O \rightarrow TiOH^{2+} + H^+$……….. (5.7)

$TiOH^{2+} \rightarrow e^- + Ti(IV) oxo\ species \rightarrow TiO_2$……….. (5.8)

The Ti(IV) oxo species is assumed to be transitional between TiO^{2+} and TiO^2, involving of partly dehydrated polymeric Ti(IV) hydroxide. If the method is free from electrochemical process then the involved chemical reaction changes and the oxidation process occurs with dissolved oxygen, which happens in this case.

$TiOH^{2+} + O_2 \rightarrow Ti(IV) oxospecies + O_2^- \rightarrow TiO_2$……… (5.9)

Bai et al.[7] mentioned in his work the time growth of nanorod is a three step process, beginning with homogenous nucleation followed by formation of immature, loosely packed dandelions and mature dense packed dandelions. By closely inspecting the matter he reported that the well-crystallized nanorods, which happened at lower NaCl concentration, can only form the loosely packed immature dandelions. This suggests that in the nucleation and growth process, some newly nucleated nanorods, which grow along the radial direction and misaligned with respect to the originally aggregated nanorods, promote the, growth of the densely packed mature dandelions. In this process pH plays a very important role as shown in equation(5.7)[3]. In a highly acidic solution, the high concentration of H+ cations restrains the hydrolysis and results in a low reaction rate. A low reaction rate favors the agglomeration of TiO2 particles[9,10] and the formation of 1D nanorods via heterogeneous nucleation. High NaCl concentration favours the formation of dandelions as Cl^- and H^+ ions both suppress the hydrolysis reaction due to the common ion effect. Cl^- ions also promotes the growth along [001] direction which has also been reported in previous works[3]. As mentioned in the previous report, initial chemical reaction was similar as shown in equation(5.9). But since the experiment is carried out in sealed reactor, once the dissolved oxygen gets exhausted reaction shown in equation(5.9) gets altered and oxidation takes place following the given reaction.

$$Ti(III)OH^{2+} + H^+ \rightarrow Ti(IV)oxospecies + H_2 \rightarrow TiO_2 \ldots\ldots\ldots(5.10)$$

Though the chemical reaction shown in equation(5.10) is energetically unfavourable, previously formed TiO2, high temperature and pressure drives it towards formation of rutile TiO_2.

Similar mechanism has been proposed by Park et al.[2] where he mentioned that strongly acidic condition is crucial for the formation of rutile TiO_2 which coincides with previously reported data. With the increase in the number of coordinated chloride ions, with increase in NaCl concentration, the titania-chloro complex $[Ti(OH)_2Cl_4]^{2-}$ becomes more symmetric, leading to enhancement of rutile formation. Chemical reactions in this process has been previously reported[3.] Presence of Cl^- supress the growth of (110) plane by enhancing growth along [001] direction.

Summarizing the previous reports, it is clear that Role of NaCl as Cl^- in the formation of TiO_2 can be of two folds. They are

I. Retarding the formation of TiO_2 by changing composition or coordination structure of growing units.

II. Influencing the morphology through adsorption of Cl^- and promotion the growth in [001].

In our work we have varied the concentration of NaCl from 0M to 5M and obtained hierarchical flower like morphology for all the samples except S_{0M}. This is mainly because in the absence of NaCl rate of reaction was very high, so just after the nucleation from each nucleation centre, growth of nanorod happened and they precipitated into the solution, which is evident from figure(5.8). With addition of NaCl, the growth is governed by the reactions mentioned in equation (5.9) and (5.10) respectively. As Cl^- of NaCl retards the rate of reaction, so the formed nucleus gets ample amount of time for more successful nucleation, which in turn reduces the ΔG_v^*, making the system thermodynamically more stable. It is possible that these newly formed nuclei may join together, by forming nucleation centre from which further growth takes place. So from the discussion it can be concluded that with increase in NaCl concentration hierarchical nanoflower with densely packed nanorod will be the anticipated microstructure, which is supported by the FESEM images as shown in figure(5.8).

Figure 5.7 indicated the fact that sample with 3M NaCl concentration (S_{3M}), has the most oriented growth on [001] direction, which coincides with our anticipated result and previous reports.

5.6 FTIR ANALYSIS

Fourier Transform Infrared Spectroscopy (FTIR) is widely used to identify organic functional group present in any molecule.

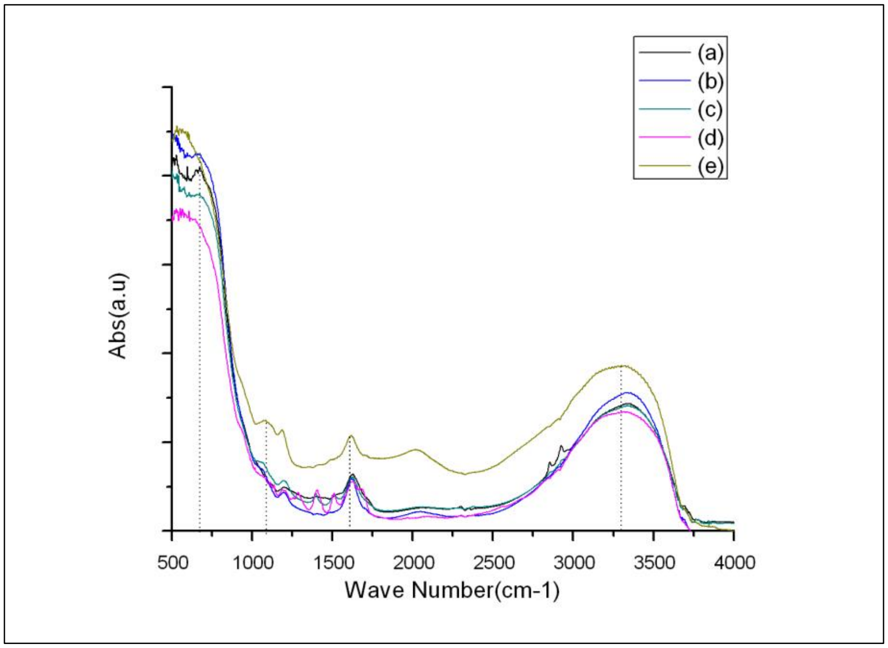

Figure 5.11: FTIR Spectrum of (a) S_{0M} (b) $S_{0.5M}$ (c) S_{1M} (d) S_{3M} (e) S_{5M} obtained from hydrothermal reaction by varying the concentration of NaCl

Khore et al.[11] did FTIR analysis of hydrothermally synthesized undoped and N-doped TiO_2 and assigned them as mentioned. He obtained a sharp band centred at 500–750 cm^{-1}, attributed to a metal oxygen (Ti–O) bond as well as the bridging Ti–O–Ti stretching mode. The formation of the O–Ti–O lattice produced IR signal in the range of 400–1250 cm^{-1}. This can be considered as the characteristics signal. The very broad peak at 3300 to 3750 cm^{-1} can be assigned as fundamental stretching vibrations of monodentate O–H (free or bonded) and surface adsorbed water molecules or a hydroxy (-OH) group. The weak band located at 1620–1630 cm^{-1} corresponds to the bending vibration of O–H.

In our work we have obtained peaks are at 647cm^{-1},1090 cm^{-1},1608 cm^{-1} and 3300 cm^{-1} which coincides with the previously reported data and confirms formation of phase pure TiO_2.

REFERENCES

1. A.Monshi, M.Reza Foroughi, M. Reza Monshi, WJNSE, 2012,2(3), 154-160.
2. K.Park, K.Min, Y.Jin, S.Seo, G.Lee, H.Shim,D.Kim, J. Mater. Chem.A,2012,22(31).
3. E. Hosono, S. Fujihara, K. Kakiuchi, H. Imai, J. Am. Chem. Soc.2014,126 , 7790–7791
4. R. V. Kasowski and R. H. Tait, Phys. Rev. B: Condens. Matter Mater.Phys., 1979, 20, 5168
5. R. H. Tait and R. V. Kasowski, Phys. Rev. B: Condens. Matter Mater.Phys., 1979, 20, 5178
6. E.Bae, N.Murakami, T.Ohno,J.Mol.Catal-A-Chem,2009,300(1-2),72-79
7. X.Bai, N.Pan, X.Wang, H.Wang, J.Solid State Chem.,2008,181(3),450-456
8. S.Cassaignon, M.Koelsch,J.Jolivet,J.Phys.Chem.Solids,2007,68(5-6),695-700
9. D.V. Bavykin, V.N. Parmon, A.A. Lapkina, F.C. Walsh., J. Mater.Chem. 14 (2004) 3370–3377
10. S. Yamabi, H. Imai, Chem. Mater. 14 (2002) 609–614
11. S.K.Khore,N.V.Tellabati,S.K.Apte,S.D.Naik,P.Ojha,B.B.Kale,R.S.Sonawane,RSC Adv.,2017,7,33029

CHAPTER 6

DETERMINATION OF LATTICE PARAMETER: RIETVELD REFINEMENT

Rietveld refinement, using Fullprof software is one of the most reliable technique for determination of lattice parameter from XRD spectrum.

6.1INTRODUCTION TO FULLPROF SUITE:

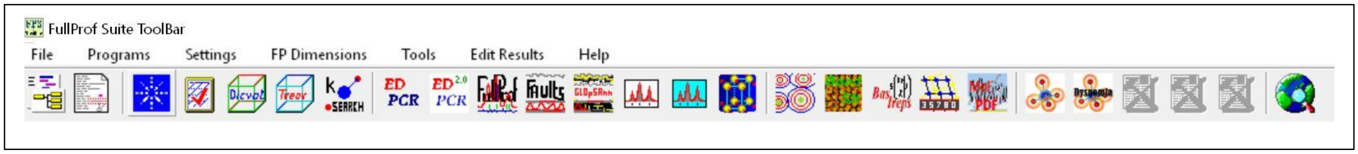

Figure 6.1: Fullprof Suite Toolbar

For our analysis purpose we need to focus on two function of the toolbar namely WinPLOTR and EDPCR.

6.1.1WinPLOTR

WinPLOTR is used to plot and analyse powder diffraction patterns. Background correction of experimentally obtained XRD pattern can be done using this function.

(a)

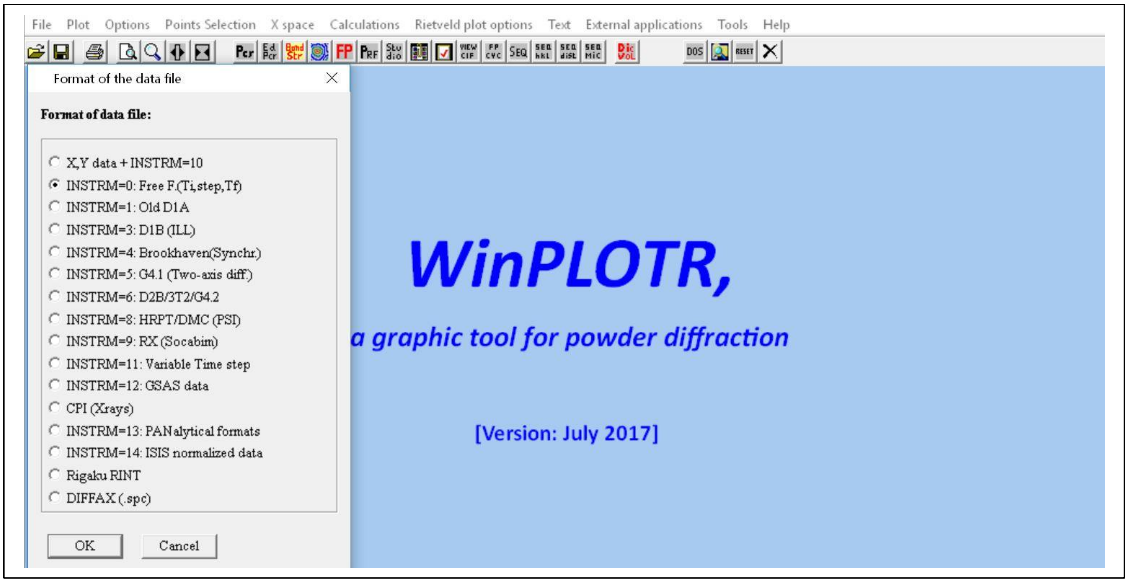

Format of the data file

Format of data file:

○ X,Y data + INSTRM=10
● INSTRM=0: Free F.(Ti,step,Tf)
○ INSTRM=1: Old D1A
○ INSTRM=3: D1B (ILL)
○ INSTRM=4: Brookhaven(Synchr.)
○ INSTRM=5: G4.1 (Two-axis diff.)
○ INSTRM=6: D2B/3T2/G4.2
○ INSTRM=8: HRPT/DMC (PSI)
○ INSTRM=9: RX (Socabim)
○ INSTRM=11: Variable Time step
○ INSTRM=12: GSAS data
○ CPI (Xrays)
○ INSTRM=13: PANalytical formats
○ INSTRM=14: ISIS normalized data
○ Rigaku RINT
○ DIFFAX (.spc)

(b)

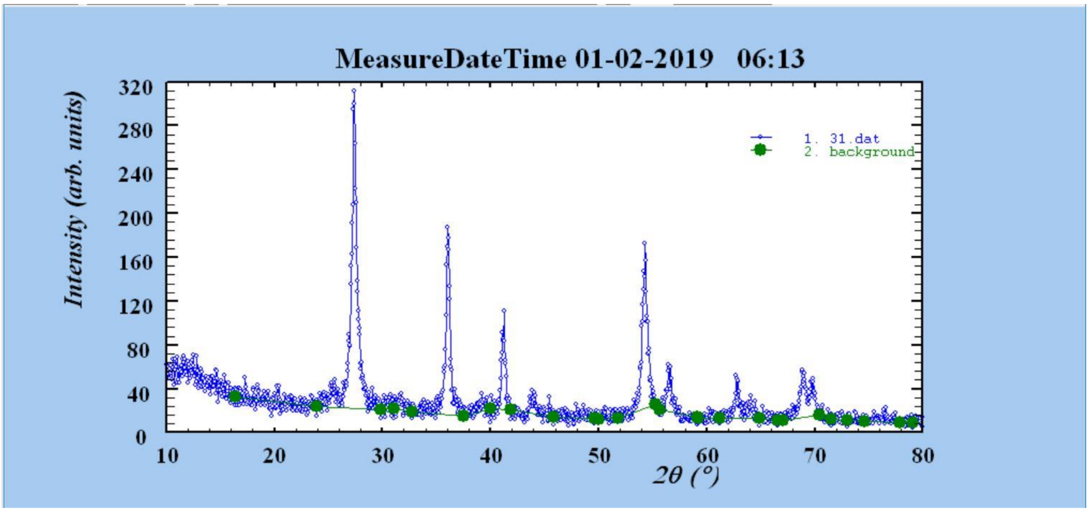

Figure 6.2: (a) WinPLOTR Tab
(b) Background Correction

6.1.2EDPCR

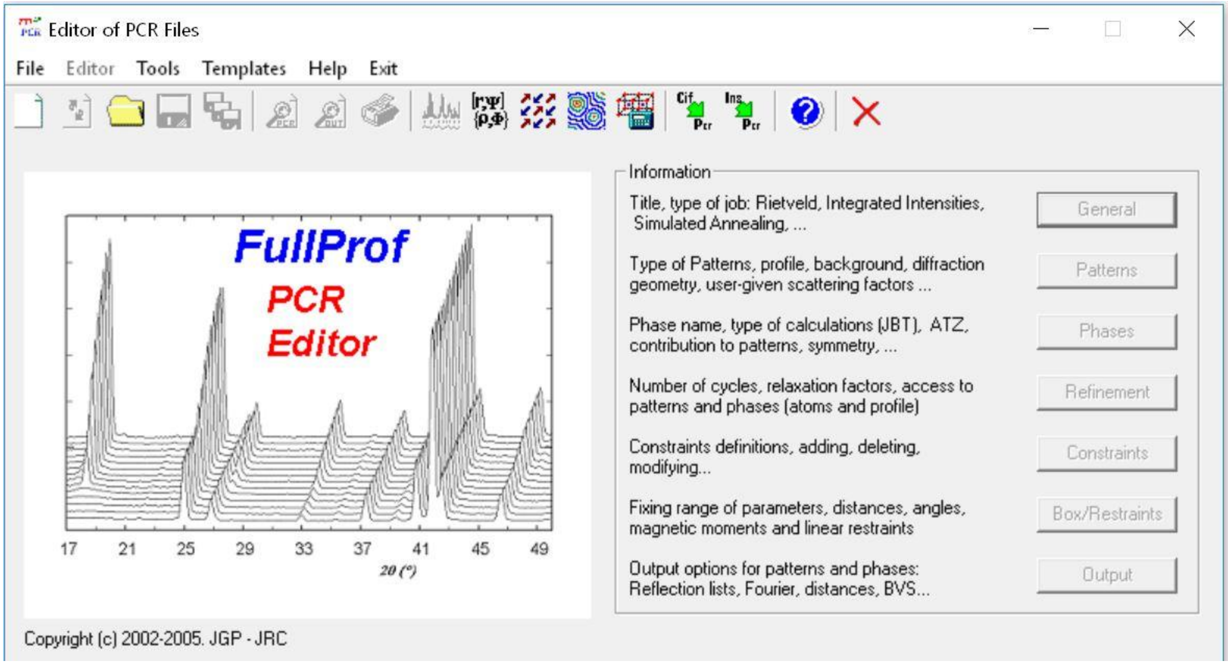

Title, type of job: Rietveld, Integrated Intensities, Simulated Annealing, ...

Type of Patterns, profile, background, diffraction geometry, user-given scattering factors ...

Phase name, type of calculations (JBT), ATZ, contribution to patterns, symmetry, ...

Number of cycles, relaxation factors, access to patterns and phases (atoms and profile)

Constraints definitions, adding, deleting, modifying...

Fixing range of parameters, distances, angles, magnetic moments and linear restraints

Output options for patterns and phases: Reflection lists, Fourier, distances, BVS...

Copyright (c) 2002-2005. JGP - JRC

Figure 6.3: EDPCR Window

Figure 6.3 represents a typical EDPRC window. The main functions can be explained below.

The information of the PCR file is distributed in seven buttons:

- General defines a general information such as title, type of job: Rietveld, Profile Matching, Simulating Annealing.
- Patterns defines patterns information: types of profile, background, geometry aspects...
- Phases defines Phase information: Names, contribution to patterns, symmetry…
- Refinement: This button is the access to the most important part of EdPCR: editing structural and profile parameters and conditions of refinement. Atom positions, profile shape parameters, magnetic moments, micro structural parameters, etc are accessible through this button.
- Constraints defines constrains for refinable parameters. You can modify, add and delete constrains relations easily by using mouse selection and clicks.
- Output is the access to the selection of output options for each phase and pattern. This allows selecting output files: Fourier, hkl-lists, files for other programs, etc.

After completion of all the necessary requirement the we need to run the Fullprof program and output is shown in the figure 6.4.

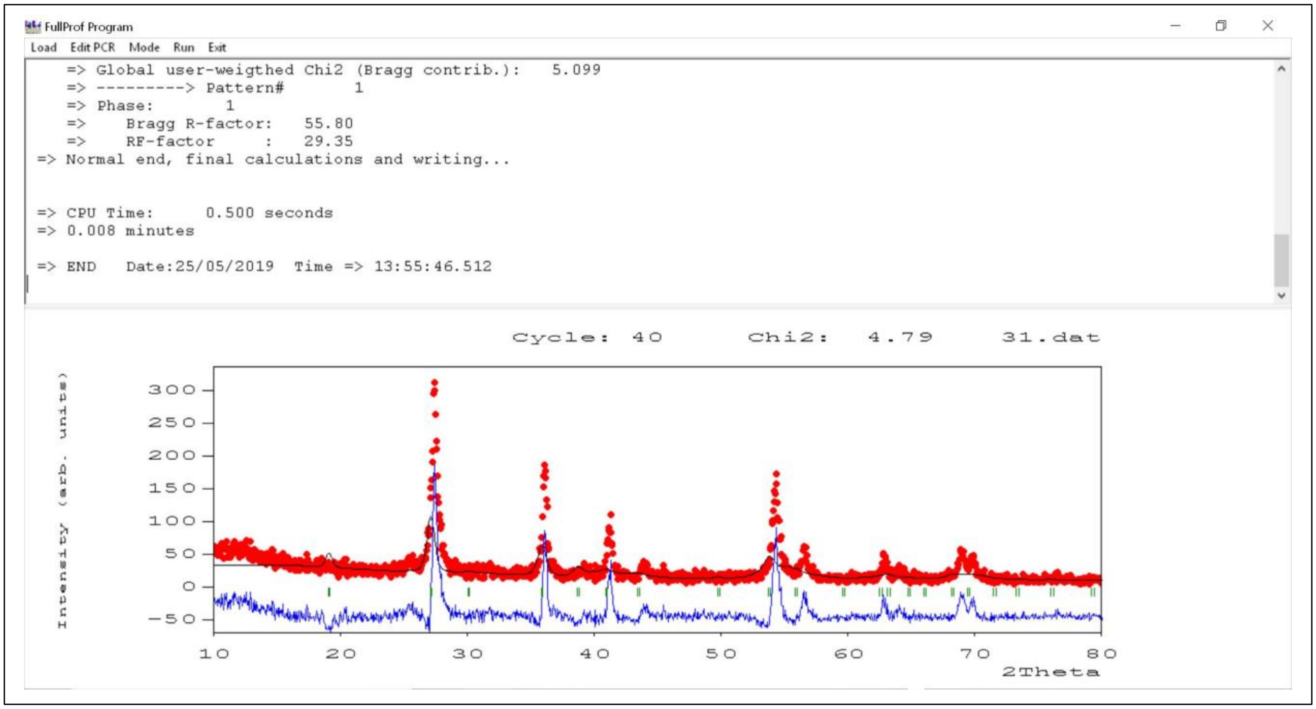

```
    => Global user-weigthed Chi2 (Bragg contrib.):   5.099
    => ---------> Pattern#       1
    => Phase:        1
    =>    Bragg R-factor:   55.80
    =>    RF-factor     :   29.35
 => Normal end, final calculations and writing...


 => CPU Time:      0.500 seconds
 => 0.008 minutes

 => END   Date:25/05/2019  Time => 13:55:46.512
```

Figure 6.4: Typical Fullprof output

6.2INITIAL DATA FILES NEEDED FOR REFINEMENT

- Original XRD data file
- Crystallographic Information (.cif) file
- Refined XRD pattern with phase matching for multiphase system

6.3SIMULATED STRUCTURE

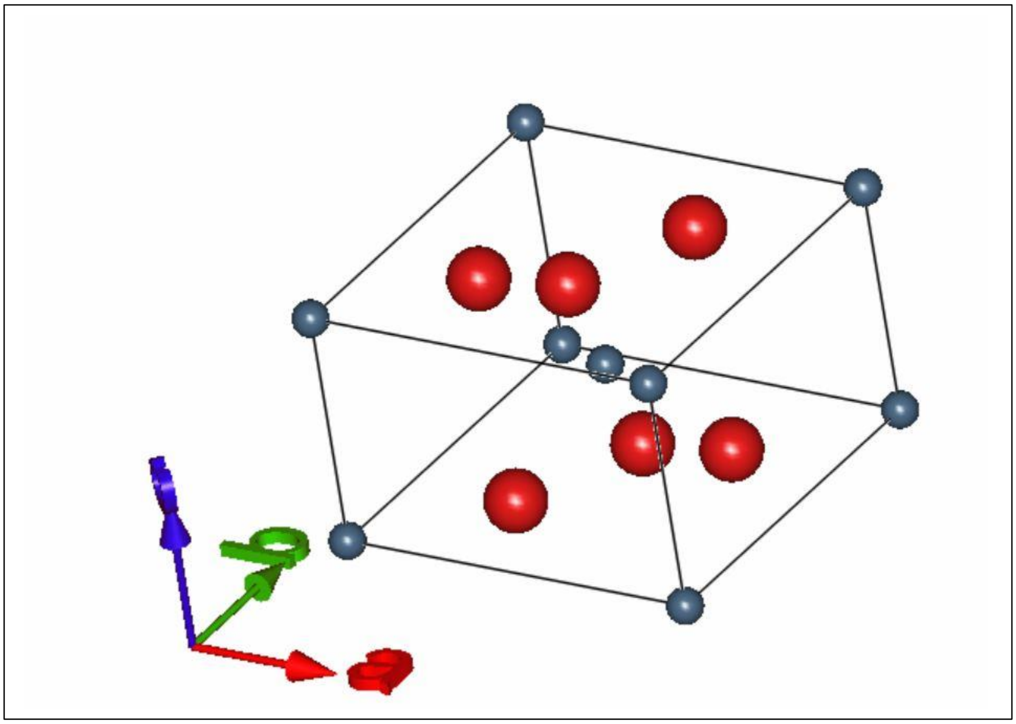

Figure 6.5: Typical Fullprof simulated structure

6.4RESULT AND DISCUSSION

Rutile TiO_2 is a tetragonal unit cell with lattice parameter a=b=4.584 Å, and c = 2.953 Å[1]. The titanium cations have a coordination number of 6, meaning they are surrounded by an octahedron of 6 oxygen atoms. The oxygen anions have a coordination number of 3, resulting in a trigonal planar coordination.

In his work Ali et al[2], completely summarize the crystal structure, optical and electrical properties of TiO_2 nanostructure as below.

Property	**Rutile Tio$_2$**
Crystal Structure	Tetragonal
Lattice Constant(Å)	a=b=4.5936; c=2.9587
Space Group	P42/mnm
Molecule(cell)	2
Volume/Molecule(Å^3)	31.21
Density (g cm^{-3})	4.13
Ti-O Bond Length (Å)	1.949 (4); 1.980 (2)
O-Ti-O Bond Angle	81.2°;90.0°
Bandgap At 10k	3.051eV
Nature of Conductivity at Room Temperature	n-type semiconductor (during undoped condition)

Table 6.1: Crystallite properties of rutile TiO$_2$

6.4.1DETERMINATION OF LATTICE PARAMETER

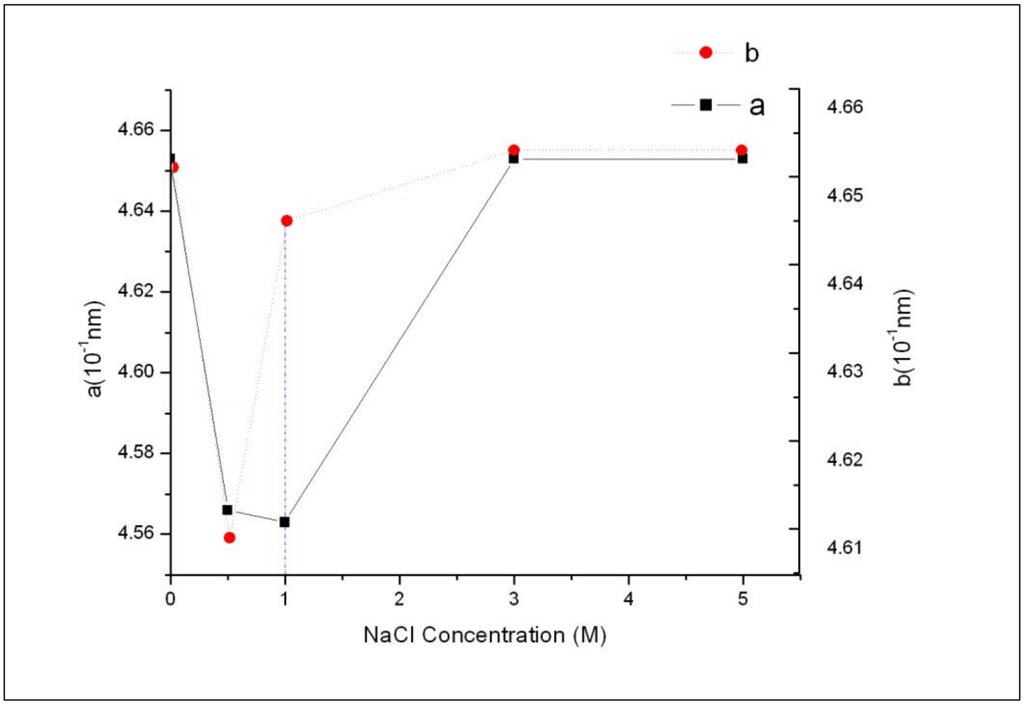

Sample Code	**a(Å)**	**b(Å)**	**a~b(Å)**
S_{0M}	4.653	4.651	0.002
$S_{0.5M}$	4.566	4.609	0.043
S_{1M}	4.563	4.645	0.082
S_{3M}	4.653	4.653	0
S_{5M}	4.653	4.653	0

Figure 6.6 ;Table 6.2: Lattice parameter variation

From figure 6.5 and table 6.2 it is clear that difference between lattice parameter is a and b is maximum for sample with 1M NaCl, S_{1M}.

Cassaignon et al.[3] reported in his work that if the pH of the precursor solution is in between 2.5 to 4.5 rutile comes as major phase with rutile particle of unexpectedly small size. As a result of it quadratic structure symmetry will be lost($a \neq b$) and modification of particle size will modify crystallite size. Borghols et al.[4] reported in work that incorporation of Li^+ ion alters the lattice parameters as internal strain is generated. Santara et al.[5] mentioned in his work that because of presence of large oxygen vacancy, internal strain is generated and change of crystallite size becomes obvious.

From the above reported results, it can be anticipated that maximum strain has been generated for $S_{1M,}$ which may be governed by required pH of precursor solution or presence of large oxygen vacancy, which may be concluded using further characterization.

6.4.2DETERMINATION OF AXIAL RATIO

Another important parameter for crystallographic analysis is axial ratio, which is nothing but ratio between lattice parameter. For rutile TiO_2 crystal axial ratio(c/a)=0.644. Axial ratio represents lattice symmetry[5]. From figure 6.6, it is clear that for S_{5M} axial ratio is minimum and deviation is also minimum. So sample with 5M concentration produces most symmetric sample, which was also expected from result tabulated in table 6.3.

Sample Code	**a(Å)**	**c(Å)**	**Axial ratio(c/a)**	**Deviation from standard value**
S_{0M}	4.653	2.978	0.64002	-0.00398
$S_{0.5M}$	4.566	2.969	0.65024	0.00624
S_{1M}	4.563	2.961	0.64892	0.00492
S_{3M}	4.653	2.969	0.63808	-0.00592
S_{5M}	4.653	2.932	0.63013	-0.01387

Table 6.3: Parameters obtained from Rietveld Refinement

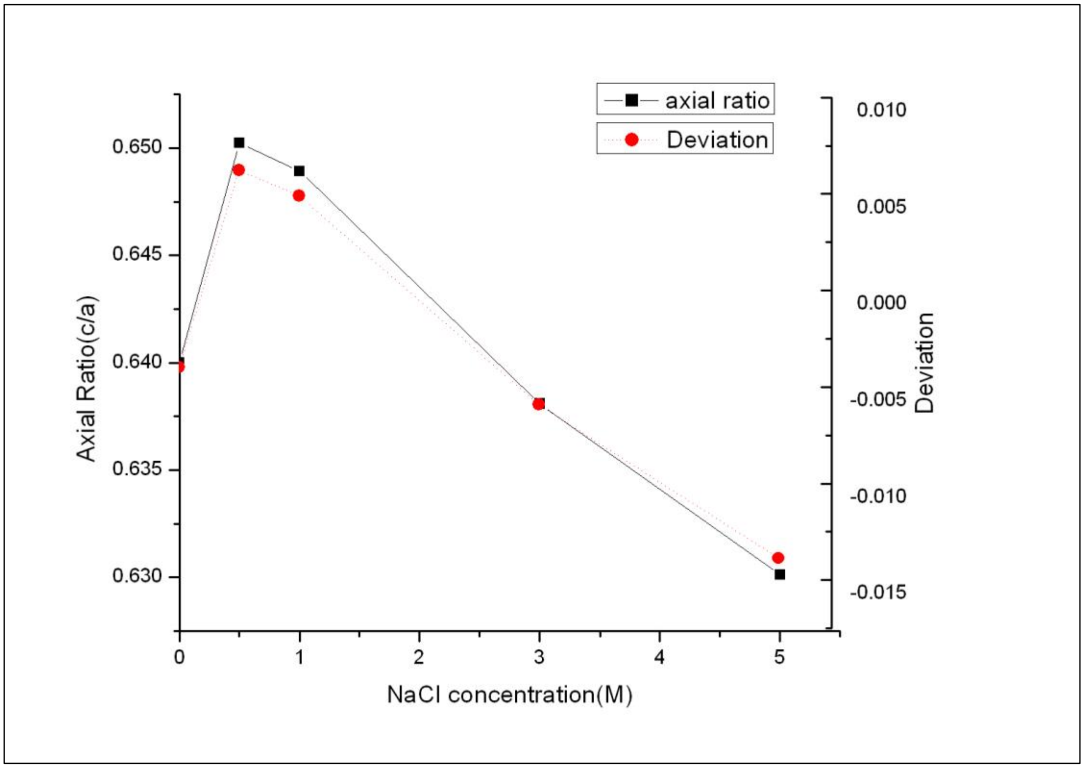

Figure 6.7: Variation in axial ratio

REFERENCES

1. U.Diebold,Surf Sci Rep,2003,48(5-8),53
2. I.Ali,M.Suhail,Z.A.Alothman,A.Alwarthan,RSC Adv.,2018,8(53),30125-30147
3. S.Cassaignon, M.Koelsch,J.Jolivet,J.Phys.Chem.Solids,2007,68(5-6),695-700
4. W.J.H.Borghols,M.Wagemaker,U.Lafont,E.M.Kelder,F.M.Mulder,Chem. Mater.,2008,20(9),2949-2955
5. B.Santara, P.K.Giri,K.Imakita,M.Fujii,J Phys D Appl Phys,2014,47(21),215302

CHAPTER 7

STUDY OF DEFECT STRUCTURE: ANALYSIS OF OPTICAL PROPERTIES

7.1UV-VISIBLE SPECTROSCOPY

UV-Visible Spectroscopy is one of the widely used technique to determine optical bandgap of any material. From UV-Visible Spectrometer Absorbance vs Wavelength spectra can be achieved, which then converts into Tauc plot to determine optical bandgap of the material.

It has been reported in previous studies that typical TiO_2 rutile poly-crystalline structure exhibits bandgap at 3.0eV[1]. In our study we have engineered defect level in order to vary the bandgap of the material.

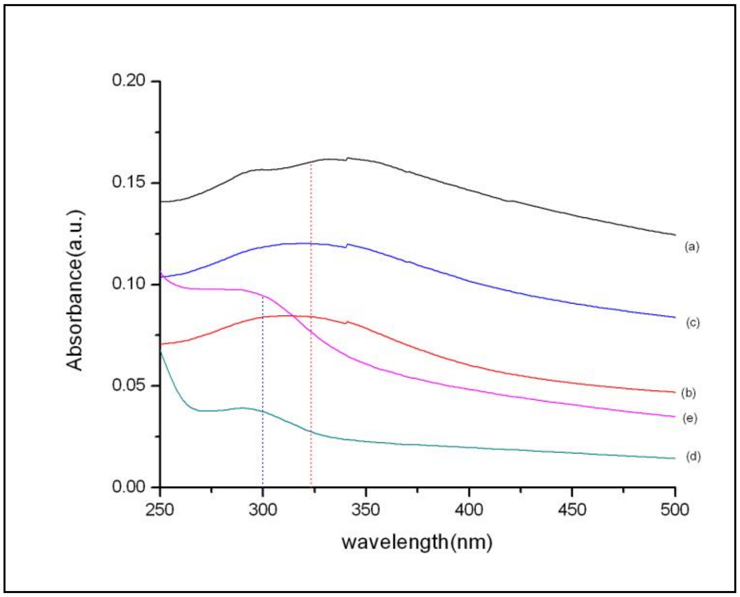

Figure 7.1: Wavelength vs absorption spectra obtained from UV-Visible spectroscopy

Tauc relation can be given as[2]

$$\alpha h\nu = A_0(h\nu - E_g)^n \ldots\ldots\ldots\ldots\ldots \quad (7.1)$$

where α is the measured absorption coefficient (cm^{-1}) near the absorption edge, A_0 is a constant, $h\nu$ is photon energy (eV), E_g is optical band gap (eV), n is a constant. The value of n is determined from the nature of optical transition, n=1/2 for direct allowed and n=2 for indirect allowed transition.

The optical band gap of semiconductor can be estimated from the intercept of the extrapolated linear fit for the plotted experimental data of $(\alpha h\nu)^n$ versus incident photon energy ($h\nu$) near the absorption edge.

(a)

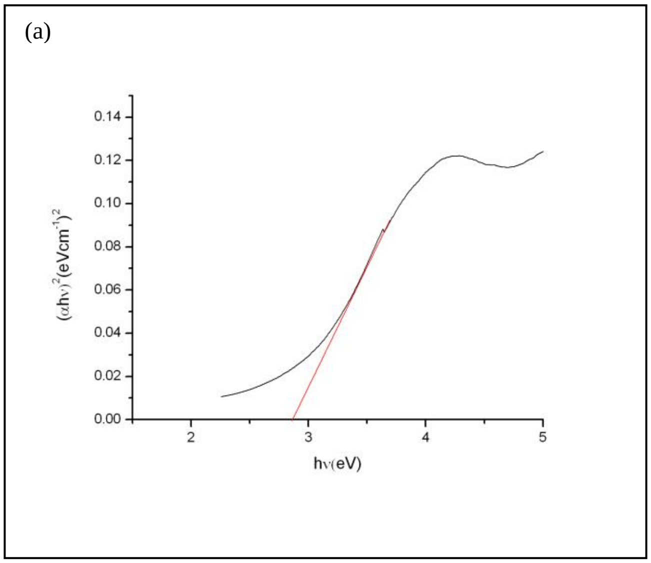

0.14
0.12
0.10
0.08
0.06
0.04
0.02
0.00
$(\alpha h\nu)^2(eVcm^{-1})^2$
2
3
4
5
hν(eV)

(b)

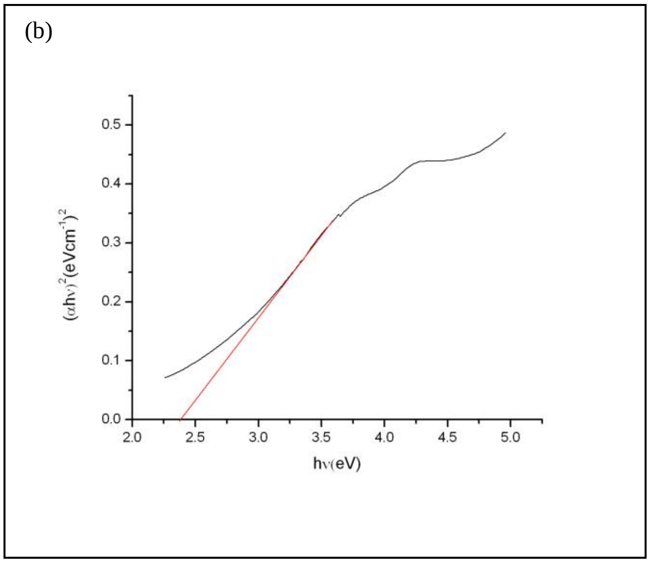

0.5
0.4
0.3
0.2
0.1
0.0
$(\alpha h\nu)^2(eVcm^{-1})^2$
2.0
2.5
3.0
3.5
4.0
4.5
5.0
hν(eV)

(c)

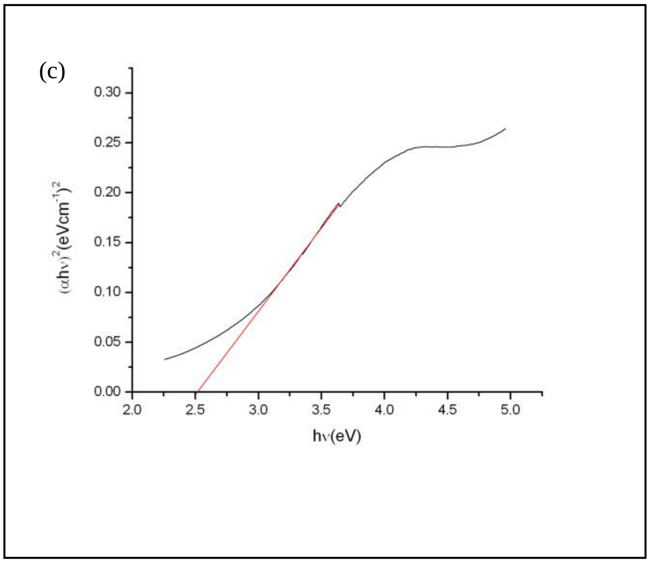

0.30
0.25
0.20
0.15
0.10
0.05
0.00
$(\alpha h\nu)^2(eVcm^{-1})^2$
2.0
2.5
3.0
3.5
4.0
4.5
5.0
hν(eV)

(d)

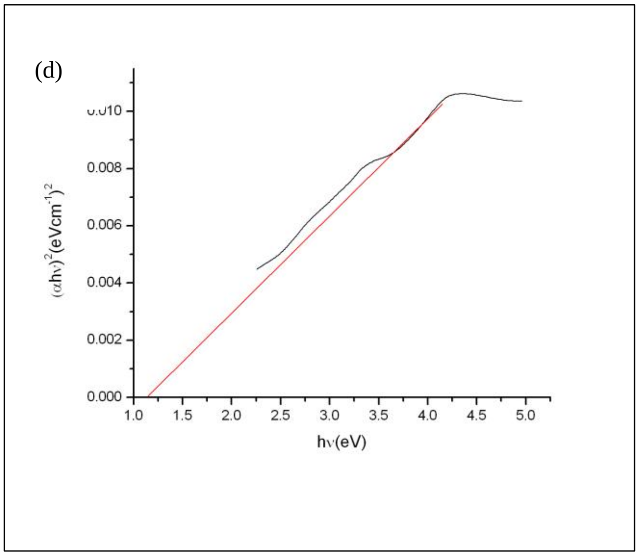

0.010
0.008
0.006
0.004
0.002
0.000
$(\alpha h\nu)^2(eVcm^{-1})^2$
1.0
1.5
2.0
2.5
3.0
3.5
4.0
4.5
5.0
hν(eV)

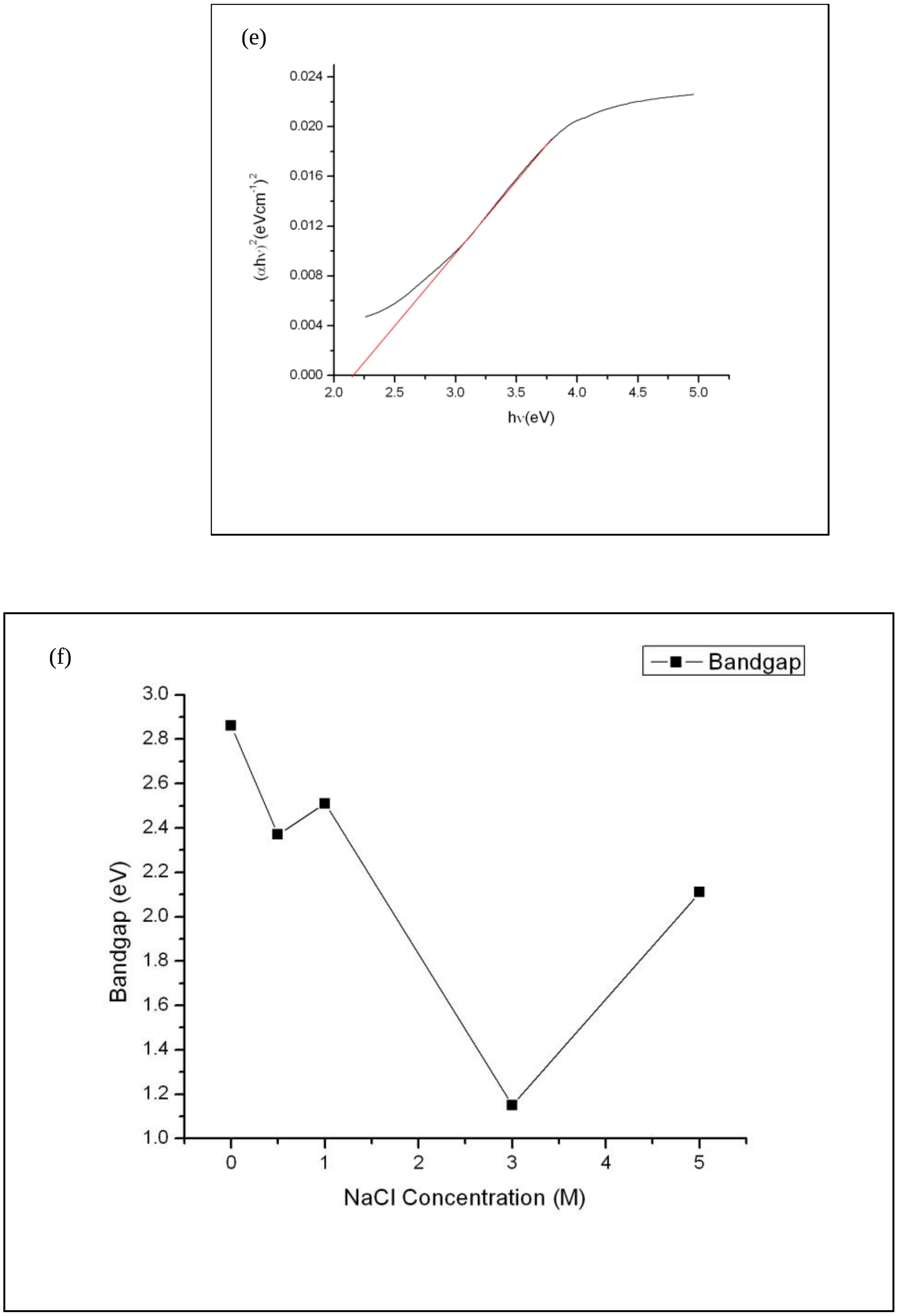

Figure 7.2: Tauc Plot of (a) S_{0M} (b) $S_{0.5M}$ (c) S_{1M} (d) S_{3M} (e) S_{5M} (f) Variation of bandgap with variation of the concentration of NaCl

From figure 7.2 it is clear that bandgap varies between 1.15eV to 2.86eV with variation in NaCl concentration. In previous work this variation in bandgap has been studied meticulously. In his work Xiao et al.[3] reported that absorption in visible region increases with increase in calcination temperature due to formation of surface oxygen vacancy and bandgap variation from 3.0eV to 2.56eV. Beranek et al.[4]explained that with increase in nitrogen content bandgap reduces from 3.18eV to 2.20eV. In another report by Beranek et al.[5] he explored N-modified anatase TiO_2 and 3.23 ± 0.03 eV— 2.11 ± 0.03 eV with increase in modification temperature which may be because of intense reduction of surface Ti^{4+} atoms to Ti^{3+} through formation of oxygen vacancies. Kernazhitsky et al.[6] observed peak and features near UV absorption edge (2.8-3.4eV) and explicated that weak absorption bands between 2.3eV and 2.9eV and assigned them to d–d transitions associated with Ti^{3+} localized states which can be associated with the presence of defect levels in-between valance band(VB) and conduction band(CB) . Presence of UV absorption peaks at 2.91–2.93 eV has also been allocated to overlapping of the lowest-energy fundamental absorption and absorption by defect states associated with TiO_2.

From the discussion and previous reports variation in bandgap in our study may be due to the formation of defect levels in between valance band (VB) and conduction band (CB) due to formation of surface oxygen vacancy. From figure 7.2(f) it is evident that the variation is not linearly increasing with increase in NaCl concentration. In order to comprehend the reason of this trend and defect concentration variation we have done further characterization such as Photoluminescence Spectroscopy, Raman Spectroscopy and TCSPC Analysis.

7.2PHOTOLUMINESCENCE ANALYSIS

PL is a very useful technique to disclose the efficiency of charge carrier trapping, immigration and transfer in a semiconductor. Generally, it is originated from the radiative recombination of electrons and holes. In this work, the luminescence properties of as synthesized TiO_2 has been studied in details.

It has been reported that when TiO_2 samples are excited at wavelength less than 320nm ($\lambda ext<320nm$), in the emission spectra the interband recombination peak appeared at around 360nm and another peak at 550nm can be attributed to indirect recombination via oxygen vacancy (Vo). Appearance of other peaks related to electronic structure or indirect recombination of bulk defects are also conceivable.[7]

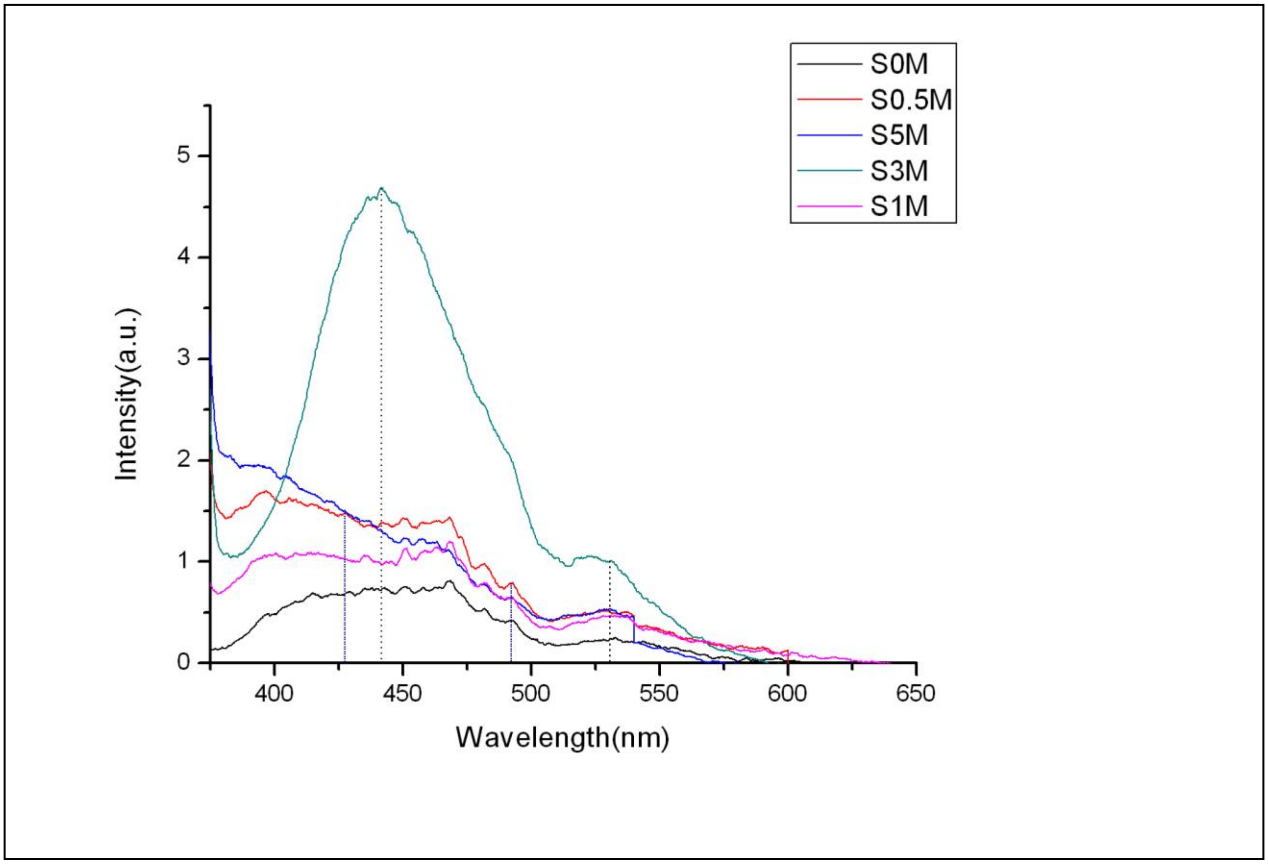

Figure 7.3: Variation of defect concentration with variation of the concentration of NaCl

In our study, we have excited all the samples at $\lambda ext=330$ nm and found out two major peaks at

(a) Violet emission at 441nm
(b) Green emission at 530nm

Though TiO_2 is a wide band gap(~3.00eV) material in the recent studies it has been found that surface defects could narrow the bandgap and endorses the parting of photogenerated charge carriers. In this context surface oxygen vacancy (Vo), gains its popularity and can be considered as one of the extensively studied surface defects.[3]

In his work Liu et al.[7] reported existence of emission peak between 400-450nm due to band edge free excitation. This surface emission was due to an indirect transition from $X_{1a} \rightarrow \Gamma_{1b}$ and can be associated with the recombination of sallow trapped surface state. Byzynski et al.[8] reported that when the sample was excited at λext=350 nm they observed emission peak at 500 nm which can be related to indirect transitions. Moreover, they noticed continuous emission from blue to yellow region (450-650nm) which can be attributed to radiative recombination between the donors associated with surface oxygen vacancy and acceptors related to the original defects. Selman et al.[9], in his study, he mentioned presence of strong emission band from 345-440nm and 527nm at λext=325nm which can be attribute to recombination of excited electron and holes and radiative recombination of the self-trapped excitons respectively. Akshay et al.[10] also cited, self-trapped excitons (STE), defects associated with oxygen vacancies and other surface defects could be the reason of the occurrence of emission peaks at 400 nm and 450 nm. He observed two peaks at 489 nm and 520 nm which may be due to Ti^{3+} to TiO_6^{2-} charge transfer, directly related to oxygen vacancies, and the formation of F+ centers, which is nothing but the oxygen vacancies with two trapped electrons respectively. In terms of energy, Kernazhitsky et al.[6] reported the presence of sharp PL peak at 2.71-2.81eV(460-440nm),2.91eV (426nm) arise from the excitonic $e^- \rightarrow h^+$ recombination via oxygen vacancies and recombination of free excitons respectively.

From figure 7.2 it is quite evident that for all the samples except S_{3M}, instead of a single peak, a broad spectrum of violet and blue emission (427nm-492nm) can be observed. Keeping the above discussion in mind it is clear that in the emission spectra, the broad peak ranging from violet to blue region(427-492nm) with centre at 441nm can be associated with the STE, defects related to surface oxygen vacancy (Vo) and other surface related defects which is extensively prominent for $S_{3M.}$ Due to the presence of defect sites, F-center, formation will be facilitated and, further, electrons occupying these will try to interact with the adjacent Ti^{4+}. A less intense peak at 530nm can therefore be attributed to the formation of F center in as synthesized TiO_2.

This result coincides with the prediction of formation of defect level between VB and CB from UV-Visible Spectroscopy analysis. From figure 7.2, it is clear that maximum band gap (2.86eV) has been obtained for the S_{0M} having minimum defect concentration whereas minimum band gap (1.15eV) is achieved for S_{3M} having maximum defect concentration.

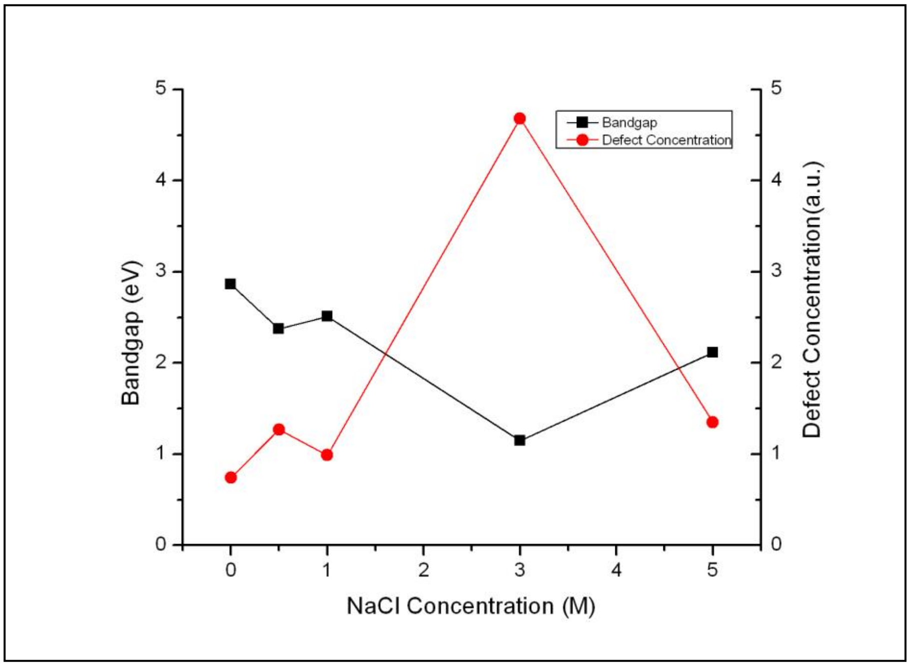

Figure 7.4: Variation of defect concentration and bandgap with variation of the concentration of NaCl

From figure 7.4, it is clear that with the increase in defect concentration bandgap reduces, which perfectly coincides with the predicted nature. So, we can conclude that with increase in surface oxygen vacancy produces defect levels in between valance band (VB) and conduction band (CB) which has also been reported in previous works.

7.3TIME-CORELATED SINGLE PHONON COUNTING (TCSPC) TECHNIQUE

Time-Correlated Single Photon Counting (TCSPC) is one of the most important methods to determine fluorescence lifetimes on the nanosecond scale. This tool is extensively used to understand radiative, non-radiative recombination, quantum yield etc by measuring the life time of excited electron. Here experimental decay curves (I(t)) corresponding to band-to-band transition needs to be fitted with biexponential decay kinetic model.

Relation between I(t) and lifetime can be given by

$I(t) = A_1 e^{(-t/\tau_1)} + A_2 e^{(-t/\tau_2)}$……………….(7.2)

where τ_1 and τ_2 represent lifetime of decay processes and 'A_1' and 'A_2'refer to corresponding decay amplitudes, i.e., weighing factors.

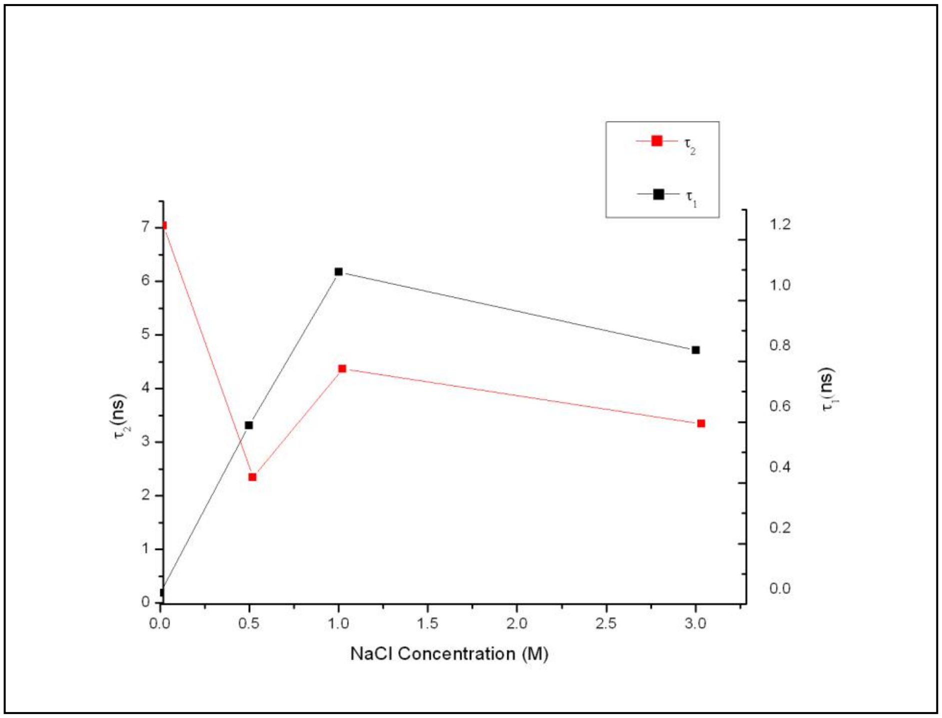

Figure 7.5: Variation of radiative and nonradiative lifetime with variation of the concentration of NaCl

Figure 7.5 represents the variation of τ_1 and τ_2 with the variation of NaCl concentration. In her work Bhattacharyya et al.[11] has mentioned that shorter (τ_{NR}) and longer (τ_R)lifetimes are assigned to non-radiative and radiative transitions, respectively, and corresponding recombination rates (k_{NR} and k_R) are expressed by $k_{NR} = \tau_{NR}^{-1}$ and $k_R = \tau_R^{-1}$. So here from figure 7.5 it is clear that $\tau_1 = \tau_{NR}$ and $\tau_2 = \tau_R$.

In his work Dingle[12] did an excellent theoretical frame work on analysis of life time measurement of semiconductor materials(GaAs). If wavefunction of electron in conduction band be Ψ_i and that of valance band be Ψ_f then,

$k_R \propto |\int \Psi_f P \Psi_i \, dv|^2$ ……………….(7.3)

where P is called momentum operator.Thomas et al.[13] elucidated that for delocalized electron-hole pair equation(7.3) attains somehow more simplified form, given by,

$k_R(r) \propto e^{-2r/a_B}$ ……………………..(7.4)

where r and a_B represent the delocalization of the electron–hole pair and Bohr radius, respectively.

As Bohr radius is constant so increase in delocalization of electron-hole pair, reduces k_R, which in turn rises τ_R. From figure 7.5 it is clear that for S_{0M} radiative recombination life time is maximum but non radiative recombination life time is minimum

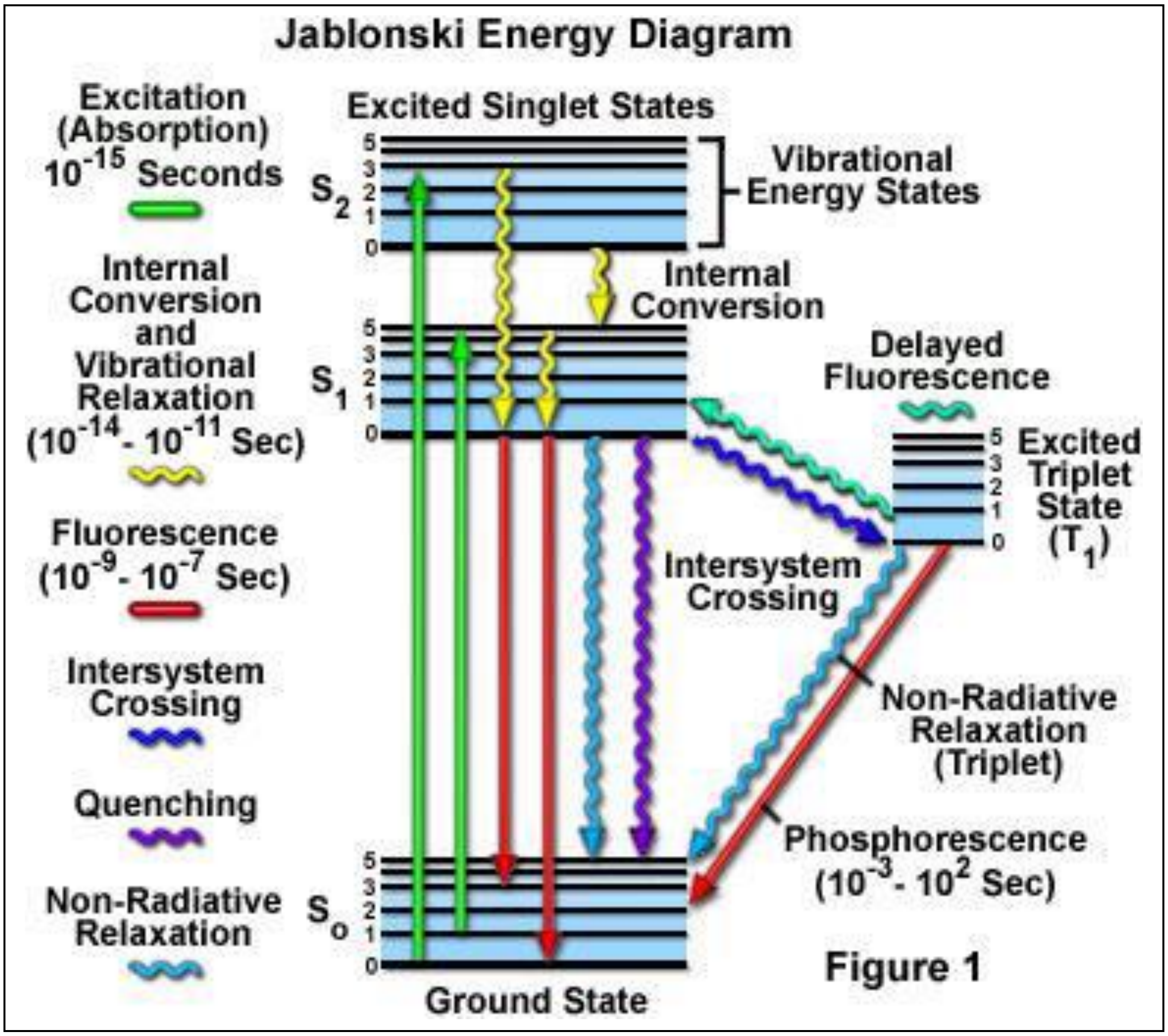

Figure 7.6: Jablonski energy diagram

By utilizing Jablonski energy diagram(figure 7.6),

it is evident that non radiative recombination takes place in the presence defect state inside crystal lattice. For S_{0M} we have already predicted that defect concentration is very low. It is impossible to fabricate any semiconductor in the complete absence of defects. Existence of inherent defects eventually gives rise to some non-radiative recombination for S_{0M}.

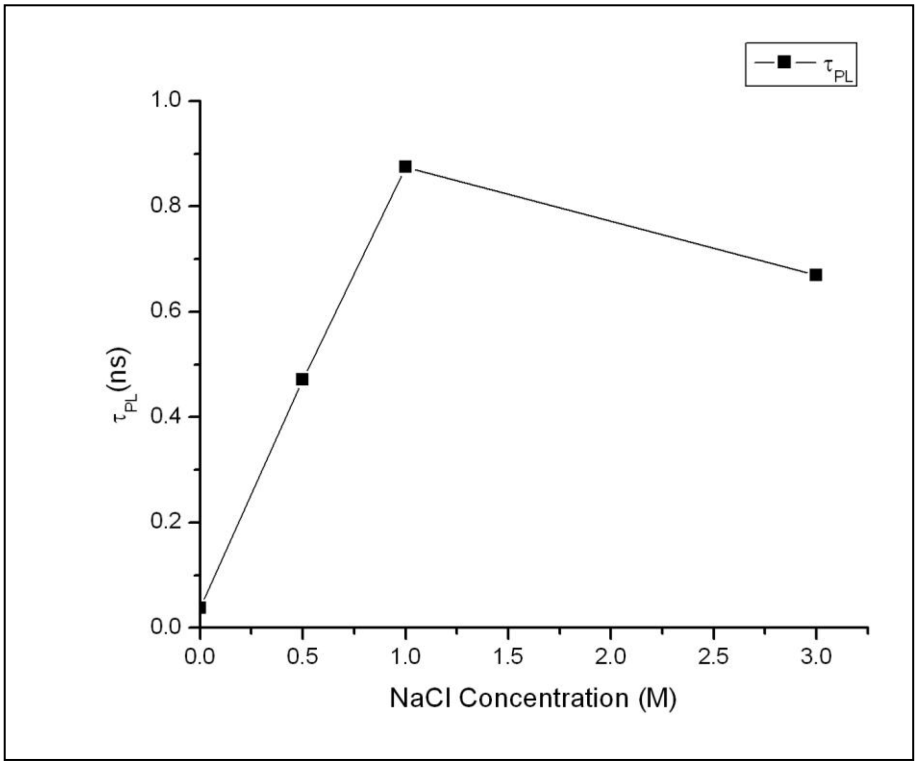

Figure 7.7: Variation of characteristic lifetime with variation of the concentration of NaCl

Characteristic Life time (τ_{PL}) can be given as,

$\tau_{PL}^{-1} = \tau_1^{-1} + \tau_2^{-1}$………………(7.5)

Figure 7.7 shows the variation of characteristic life time of as synthesized TiO_2, where S_{1M} shows maximum characteristic life time which in turn clarifies the fact that total probability of recombination is maximum for this sample, following the trend of τ_{NR}. So non-radiative recombination is predominant for all the samples because of presence of highly concentrated defect levels.

Sample Code	τ_R (ns)	τ_{NR}(ns)	τ_{PL}(ns)
S_{0M}	7.0416	0.03773	0.03753
$S_{0.5M}$	2.35	0.589	0.47096
S_{1M}	4.37	1.093	0.87432
S_{3M}	3.347	0.8368	0.66943

Table 7.1: Parameters obtained from TCSPC Analysis

7.4MICRO RAMAN ANALYSIS

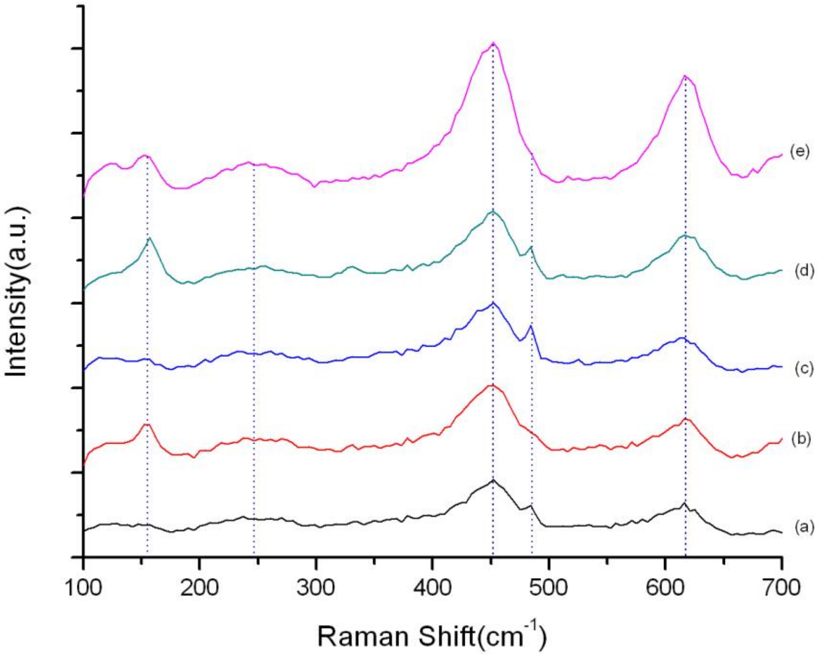

Figure 7.8: Raman Spectra of (a) S_{0M} (b) $S_{0.5M}$ (c) S_{1M} (d) S_{3M} (e) S_{5M}

Figure 7.8 represents the micro raman analysis of as synthesized samples of Rutile phase TiO2. Raman Spectroscopy shows the peaks around 155cm^{-1}, 250cm^{-1},452cm^{-1} and 617cm^{-1} .

The optical modes of Rutile TiO_2 at T point can be given as[14]

$T_{opt} = A_{1g} + A_{2g} + A_{2u} + 2B_{1u} + B_{1g} + B_{2g} + E_g + 3E_u$……..(7.6)

where g represents Raman active, u infrared active and E degenerate modes.

E_g mode can be associated with the motion of O tetrahedral, causing a significant stretching of the tetrahedral bonds. The four O atoms show breathing like vibrations with different vibrational direction of O tetrahedron. Thus, this mode can be fundamentally considered as an anti-symmetric breathing vibration of the O tetrahedron.

B_{1g} and B_{2g} modes are related with motion of Ti atoms in tetrahedron, especially the stretching and breathing motions

A_{1g} mode can be connected to the displacements in which two oxygen atoms bend out of phase perpendicular to the centre Ti atom.

A less intensified peak at around 480cm^{-1} is mainly related to amorphous silicon (Si) which originates due to glass substrate.[15]

In his work Park et al.[16] synthesized Rutile TiO_2 and obtained distinct Raman peaks at 140cm^{-1}, 240cm^{-1}, 442cm^{-1} and 607cm^{-1} and marked them as B_{1g} mode, Multiphoton process, E_g mode and A_{1g} mode respectively. Cheng et al.[17] mentioned in his work that with reduction in grain size E_g mode decreased by about 8 cm^{-1}, while a new broad band near 112 cm^{-1} appeared gradually and the band near 144 cm^{-1} could be covered. Hardcastle et al.[18] cited that presence of major peaks at 610, 446, and 242 cm^{-1} can confirm the formation of Rutile TiO_2. Aoyama et al.[19] also mentioned in his work that Raman spectroscopy peaks around 240, 450, and 620 cm^{-1} is consistent with second order phonon, E_g, and A_{1g} modes of rutile TiO_2 crystal.

From figure 7.8 distinct peaks obtained at 155cm^{-1}, 250cm^{-1}, 452cm^{-1}, 617cm^{-1} can be assigned to B_{1g} mode, Multiphoton process or second order phonon mode, E_g mode and A_{1g} mode respectively. From the reported data a consistent blue shift of 10cm^{-1} has been achieved which is mainly because when light comes in contact with the material, it either gains by some quanta or loses some quanta by interacting with the vibrational modes of the material, called phonons. Blue shift indicates increase in energy, thus by gain of quanta.

Xiao et al.[3] extensively studied the effect of oxygen vacancy on rutile TiO_2 in his work. In consistence with previous work on Raman spectroscopy analysis he also mentioned that broadening of raman peaks demonstrates that surface oxygen vacancies break down the symmetry of rutile TiO_2 lattice, which is consistence with our result.

In his work P. Colomban[20] meticulously explained the raman spectroscopy analysis on nano material domain. According to his work presence of strong peaks between 400 and 1000 cm^{-1} for inorganic phases represents stretching M–X modes, which is eventually been established in previously mentioned reports.

He also presented a very strong guide line on intensity variation of Raman peaks. According to his work

Sample Code	B_{1g} (cm^{-1})	Second Order Phonon (cm^{-1})	E_g (cm^{-1})	A_{1g} (cm^{-1})
S_{0M}	137.83	249.56	451.91	616.13
$S_{0.5M}$	154.35	253.67	450.44	618.48
S_{1M}	140.47	248.39	451.91	614.66
S_{3M}	156.84	255.13	451.91	617.60
S_{5M}	153.47	245.75	451.91	618.77s

Table 7.2: Parameters obtained from Microraman Analysis

parameters governing vibration-induced charge transfers, in other words the "conductivity," (iono-covalency, band structure, electronic insertion, resonance,) will set the Raman peak intensity. The vibration of charged species is somewhat analogous to high frequency conductivity.

Relation between Raman Intensity ($I_{raman}(\bar{\nu})$) and conductivity ($\sigma(\bar{\nu})$) can be related using the following eqautaion

$I_{raman}(\bar{\nu}) \propto \frac{n^B(\bar{\nu})+1}{\bar{\nu}}\sigma(\bar{\nu})$……………….(7.7)

where n^B is called Bose occupation factor.

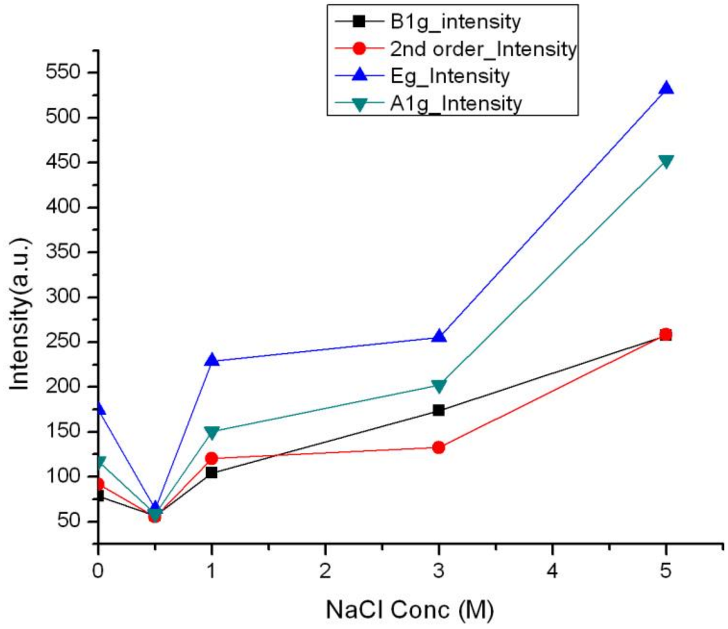

Figure 7.9: Variation of different Raman active modes with variation of the concentration of NaCl

From the figure 7.9 it is expected to have minimum conductivity for $S_{0.5M}$ but this method involves certain problems[21]. During assessment an unknown changes of Raman cross sections for the materials this will lead to an overestimation of the phase when calculating the $I_{raman}(\bar{v})$ for layers with higher oxygen contents.

REFERENCES

1. J.Bu,J.Fang,W.R.Leow,K.Zhenga,X.Chen,RSC Adv., 2015,5, 103895-103900
2. P.S.Shinde,G.H.Goa,W.J.Lee,J. Mater. Chem., 2012,22, 10469-10471
3. F.Xiao,W.Zhou,B.Sun,H.Li,P.Qiao,L.Ren,X.Zhao,H.Fu,Science China Materials,2018,61(6),822-830
4. R.Beranek,B.Neumann,S.Sakthivel,M.Janczarek,T.Dittrich,H.Tributsch,H.Kischa,Chem.Phys.,2007,339(1-3),11-19
5. R.Beranek,H.Kischa,Photochem. Photobiol. Sci., 2008,7, 40-48
6. L.Kernazhitsky,V.Shymanovska,T.Gavrilko,V.Naumov,L.Fedorenko,V.Kshnyakin,J.Baran,J. Lumin.,2014,146,199-204
7. B.Liu,X.Zhao, L.Wen, Mater Sci Eng B Solid State Mater Adv Technol,2006,134(1),27–31
8. G.Byzynski,C.Ribeiro,E.Longo,INT J PHOTOENERGY,2015,831930
9. A.M.Selmana,Z.Hassana,M.Hushama,N.M.Ahmeda,Appl Surf Sci.,2014,305,445–452
10. V.R.Akshay,B.Arun,G.Mandal,A.Chandad,M.Vasundhara,New J. Chem.,2019,43,6048-6062
11. P.Bhattacharyya,S.Bhattacharjee,M.Bar,U.K.Ghorai,M.Pal,S.Baitalik,C.K.Ghosh,Appl Phys A,2018,124(11),9
12. R.Dingle,PhysRev.,1969,184,788
13. D.G.Thomas,J.J.Hopfield,W.M.Augustynia,Phys.Rev.,1965,14(1A),202
14. I.Lukačević,S.K.Gupta,P.K.Jha,D.Kirin,Mater.Chem.Phys.,2012,137(1),282-289
15. R.L.C. Vink, G.T. Barkema, and W.F. van der Weg, Phys. Rev. B,2001 ,63, 115210
16. K.Park, K.Min, Y.Jin, S.Seo, G.Lee, H.Shim,D.Kim, J. Mater. Chem.A,22(31),15981,2012
17. H.Cheng,J.Ma,Z.Zhao,L.Qi,Chem. Mater.1995,74,663-671
18. F.D.Hardcastle,H.Ishihara,R.Sharma,A.S.Birisb,J. Mater. Chem.,2011,21,6337-6345
19. Y.Aoyama,Y.Oaki,R.Isea,H.Imai,CrystEngComm,2012,14,1405-1411
20. P.Colomban,Quantum Matter,2014,3(4),361-380
21. A.Lambertz,T.Grundler,F.Finger,J.Appl.Phys,2011,109,113109

CHAPTER 8

MEASUREMENT OF PHOTODIODE CHARACTERISTICS OF TiO2-pSi HETEROJUNCTION FABRICATED ON P-Si SUBSTRATE

Photodiode is one of the fundamental optoelectronic two terminal devices. Photodiodes are designed to respond to photon absorption. Some photodiodes have extremely high sensitivity. With the advancement in the field of electronics, photodiodes play an important role in optoelectronic as well as energy harvesting device.

8.1THEORY OF PHOTODIODES

8.1.1THEORY OF P-N JUNCTION

A p–n junction is a boundary or interface between two types of semiconductor materials, p-type and n-type, inside a single crystal of semiconductor. An intrinsic semiconductor, free from impurity is not capable of carry charge at 0K, as no electron is present in conduction band. If we replace one atom of these intrinsic semiconductor by atom of pentavalent material (group V in periodic table) such as P, As or Sb or trivalent material (group III in periodic table) such as B, Al, Ga then defect state is produced due to presence of excess or insufficient electrons respectively. These semiconductors are called extrinsic semiconductor, and the replacement are called “doping”.

Doping by pentavalent material generates excess electron defect level in close proximity of conduction band, which is known as “donor level”, because very less energy is needed to excite electron from this level to conduction band. As in this case electron is the majority charge career, they are known as “n-type semiconductor”.

Doping by trivalent material results in deficiency of electron or excess of hole, which produces defect level in close proximity of valance band, which is known as “acceptor level”, because very less energy is needed to excite electron from valance band to this level, thus producing more hole in valance band. As in this case hole is the majority charge career, they are known as “p-type semiconductor”.

Diffusion of n-type and p-type semiconductor into each other produces p-n junction. As a result of diffusion, depletion region is produced in the junction.

8.1.2 ENERGY BAND DIAGRAM

(a)

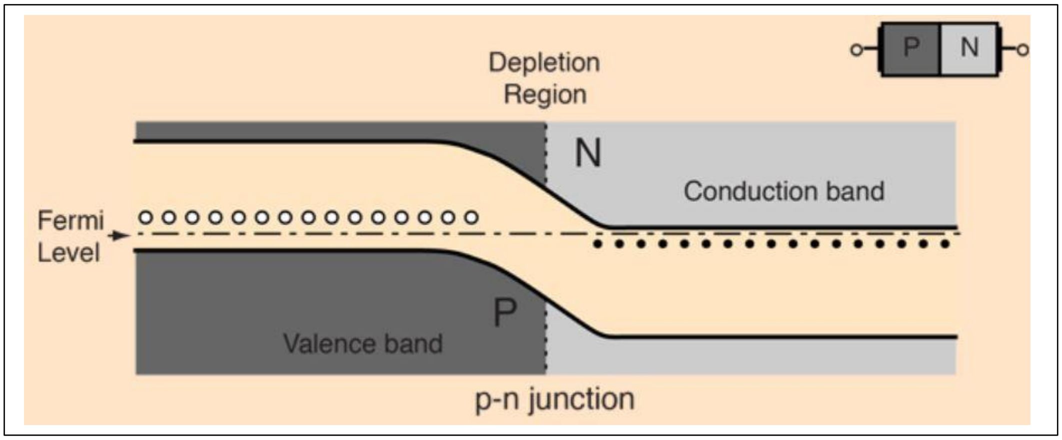

(b)

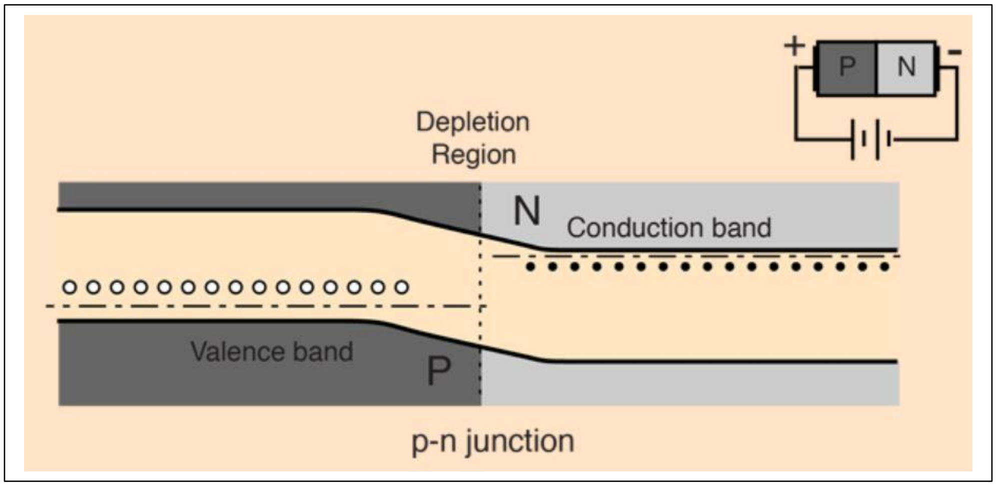

(c)

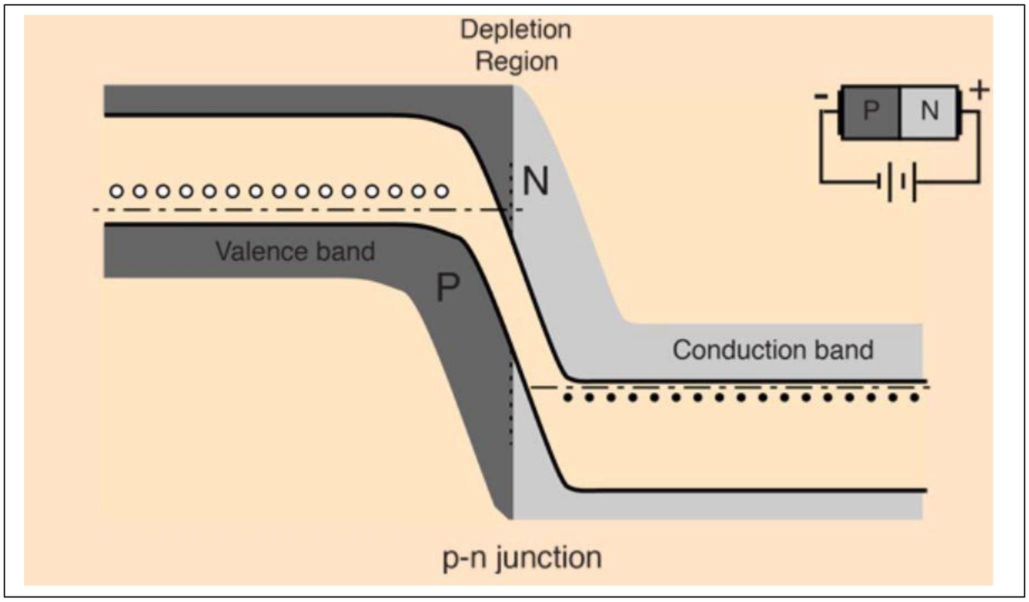

Figure 8.1: Energy Band diagram of p-n junction

8.1.3.CURRENT AND VOLTAGE IN AN ILLUMINATED JUNCTION

Generation of current can be considered due to drift of minority carriers across junction. In particular, carriers generated within depletion region are separated by junction field, electrons being collected in the n-region and holes in p-region. If the junction is uniformly illuminated such that $h\nu > E_g$, an added generation rate g_{op}(EHP/cm^3-s) participates in this current. The number of holes and electrons created per second within a diffusion length of the transition region on n-side and p-side is AL_pg_{op} and AL_ng_{op} respectively. So the resulting current due to collection of this optically generated carriers can be given as,

$I_{op} = qAg_{op}(L_p+L_n+W)$…………(8.1)

where W is the junction length

If I_{th} be the thermally generated current and I_{op} be the optically generated current, then net current directed from n to p side can be given as,

$I = I_{th}\left(e^{\frac{qV}{kT}} - 1\right) - I_{op}$ …………….(8.2)

So,from equation (8.1) and (8.2) it can be predicted that with increase in optical generation, I-V curve will be lowered proportional to the generation rate g_{op}.

8.2EXPERIMENTAL

8.2.1FABRICATION OF P-N BULK HETEROJUNCTION

TiO_2 is a n-type semiconductor, so we deposited it into a p-Si substrate in order to fabricate p-n bulk heterojunction. Initially, substrate was cleaned following standard procedure in an ultrasonic bath. A well dispersed solution of as synthesized TiO2 nanostructures has been prepared and deposited onto p-Si substrate using spin coating technique with a spin rate of 1500rpm, followed by annealing at 90°C for 45 minutes. Using surface profiler thickness of the film was maintained as 1 micron. Effective cell area was maintained as $1mm^2$.

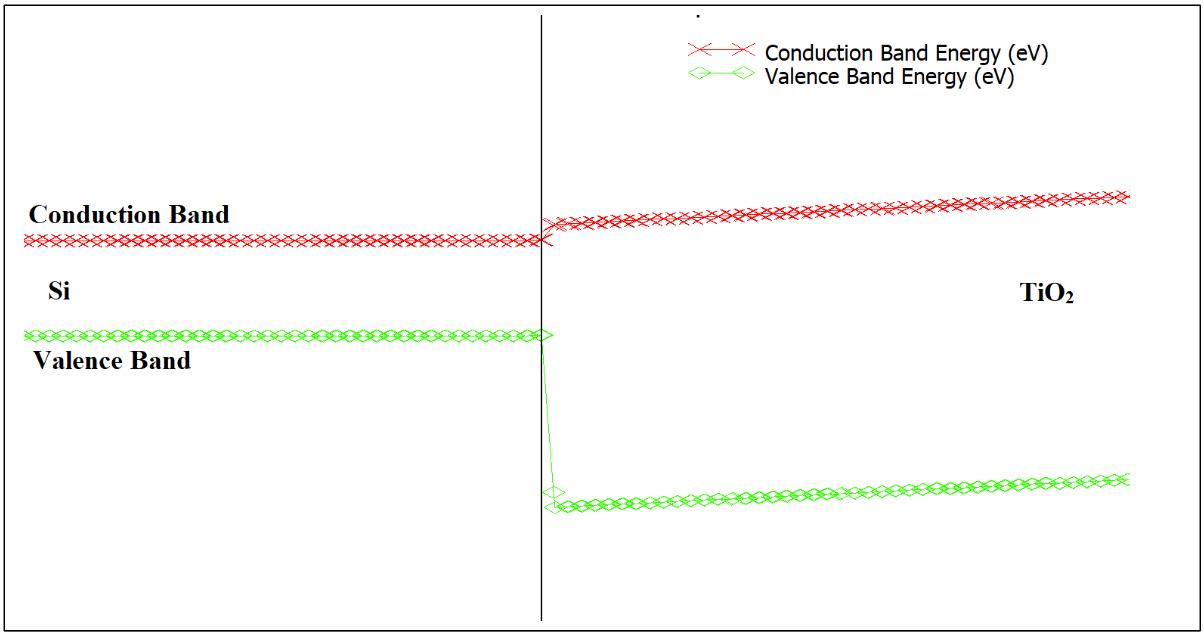

Figure 8.2: Energy Band diagram of p-Si-TiO_2 bulk heterojunction

8.3RESULT AND DISCUSSION

Electrical characterization has been done under 1.5AM solar simulator, with average power of 100mWcm^{-2}, and current voltage characteristics(V-I) has been measured.

(a)

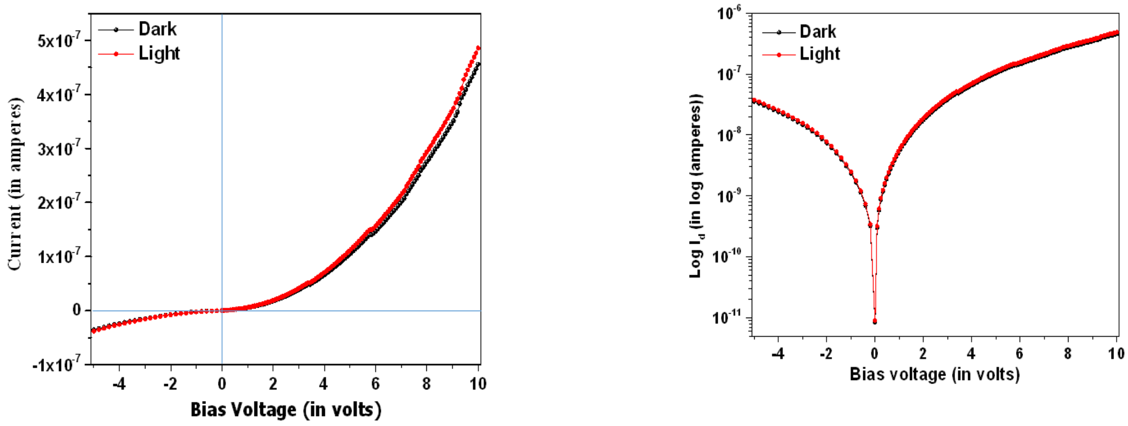

(b)

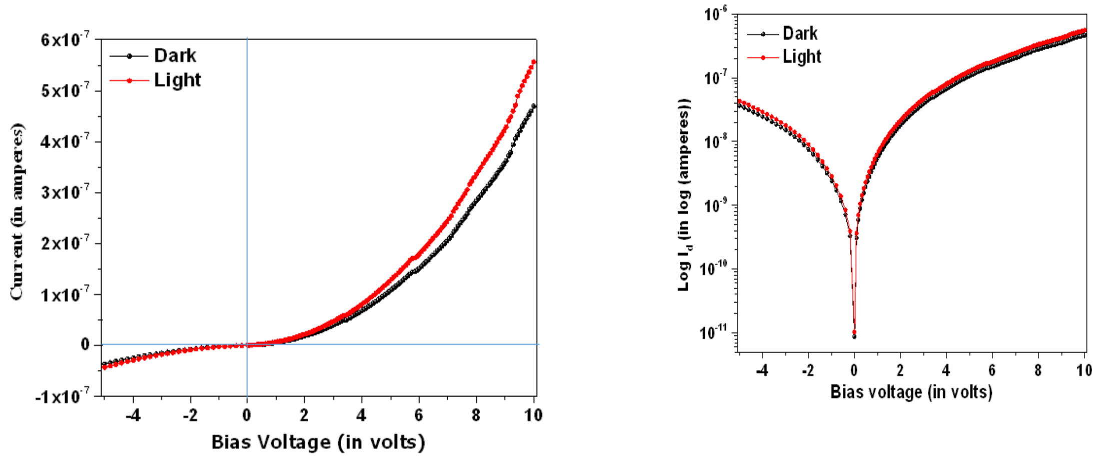

(c)

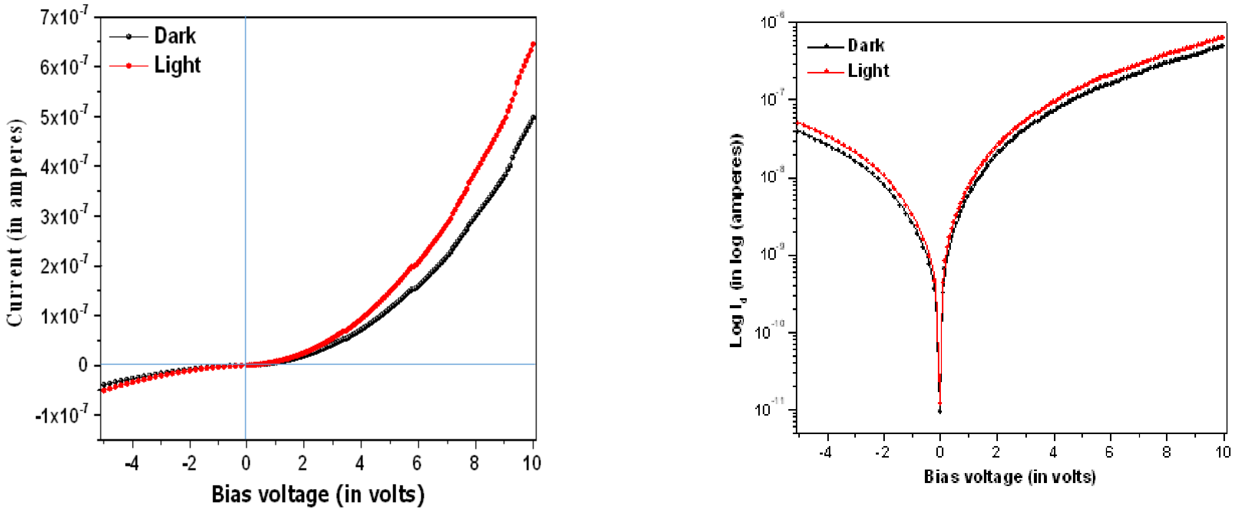
Dark
Light
Current (in amperes)
7x10-7
6x10-7
5x10-7
4x10-7
3x10-7
2x10-7
1x10-7
0
-1x10-7
-4
-2
0
2
4
6
8
10
Bias voltage (in volts)
Dark
Light
Log Id (in log (amperes))
10-6
10-7
10-8
10-9
10-10
10-11
-4
-2
0
2
4
6
8
10
Bias voltage (in volts)

(d)

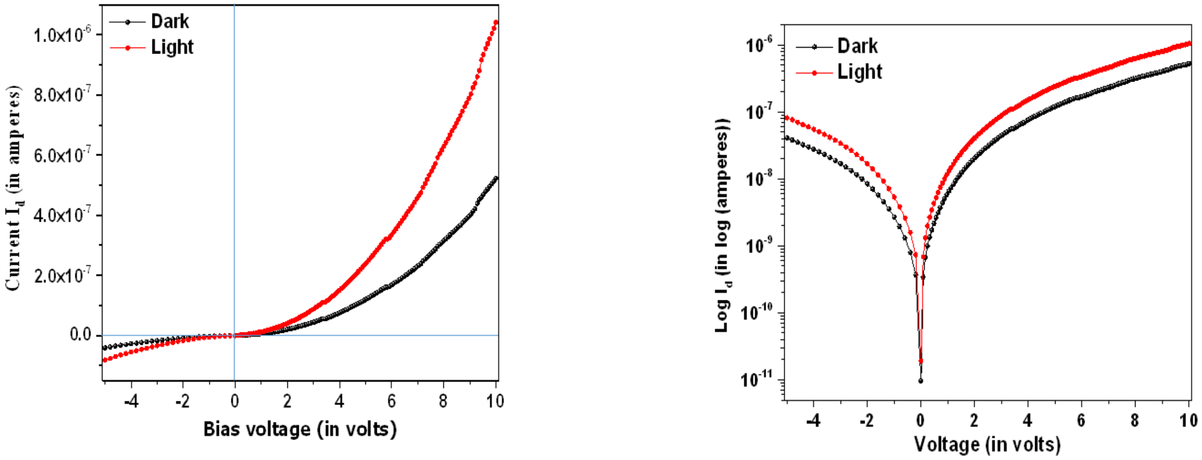
Dark
Light
Current Id (in amperes)
1.0x10-6
8.0x10-7
6.0x10-7
4.0x10-7
2.0x10-7
0.0
-4
-2
0
2
4
6
8
10
Bias voltage (in volts)
Dark
Light
Log Id (in log (amperes))
10-6
10-7
10-8
10-9
10-10
10-11
-4
-2
0
2
4
6
8
10
Voltage (in volts)

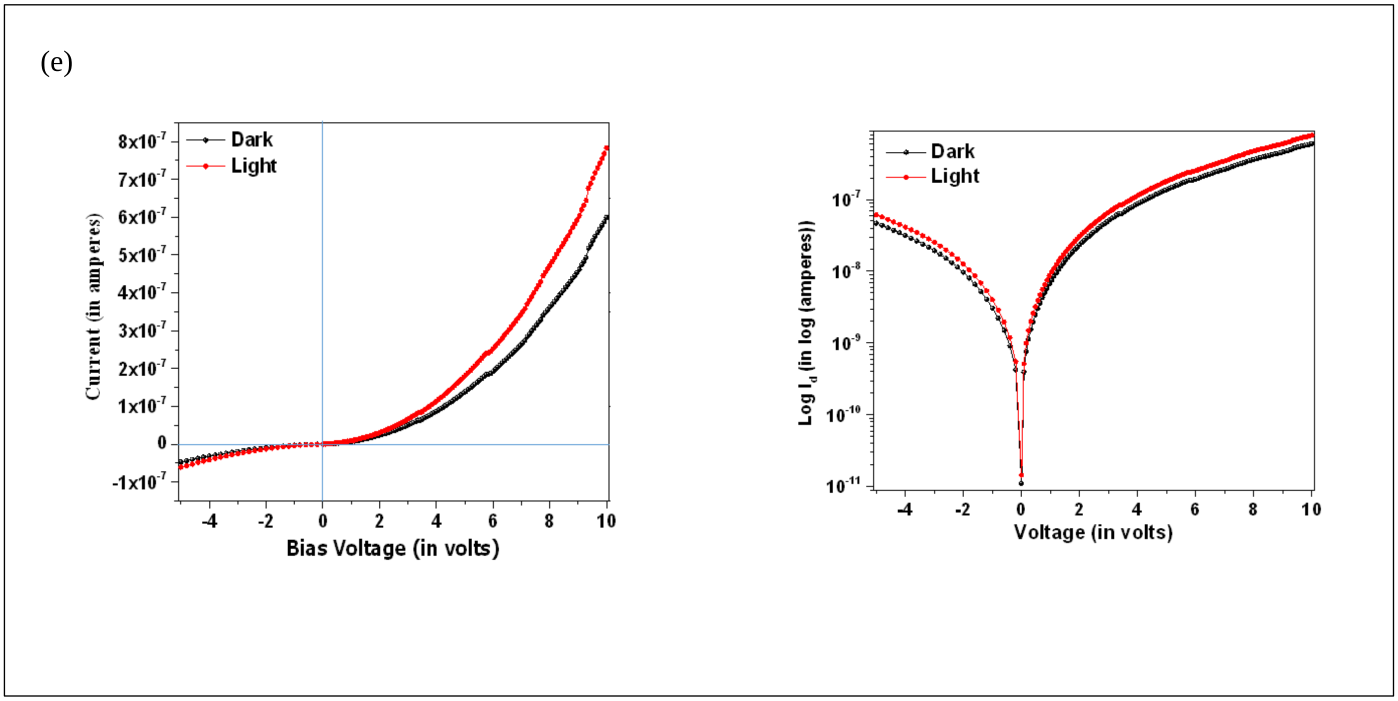

Figure 8.3: V-I characteristics of p-Si-TiO$_2$ bulk heterojunction

Figure 8.3 current-voltage characteristics of fabricated photodiode. Net calculated current of a photodiode can be given as,

$I_D=I_d-I_{ph}$ …………….(8.3)

where I_d represents dark current and I_{ph} represents photo current.

From figure 8.3 it is clear that under illumination, with increase in bias voltage, I_{ph} becomes predominant over I_d which generates due to thermionic emission of the diode. Using equation(8.3) photo diode current has been calculated across sample and plotted.

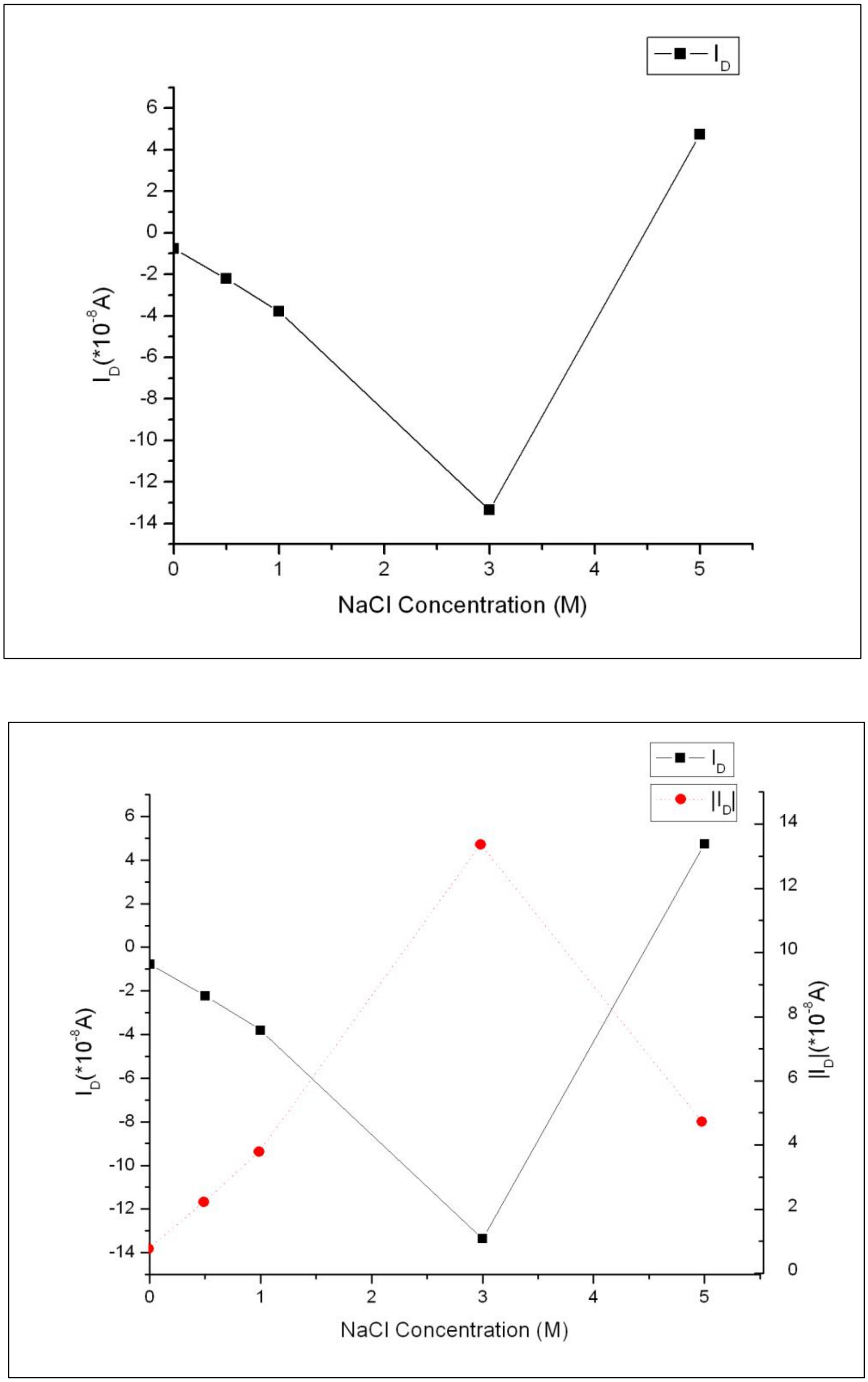

Figure 8.4: Variation of photodiode current

From figure 8.4 apparently it may look like for S_{3M}, diode current is minimum. This is because of the fact that photodiode current is governed by equation(8.3), which indicates appearance of negative sign, as photocurrent is much higher in magnitude of dark current. From figure 8.4, it is clear that S_{3M} is capable of producing maximum diode current in bulk heterojunction.

Under dark condition, the device showed current value which is one order of magnitude smaller than the current under illumination. This finding indicates that the PD can exhibit excellent light response. The current stays nearly constant at small bias ($V_{bias}< 1$ V). These results indicate that the charge carriers created by the illumination at a high bias voltage ($V_{bias}> 1$ V) have a main function of determining the current, which causes the increase in current. However, when a small bias is applied, the current is not sensitive to the illumination since the current of the device is restricted by the depletion region between the n-TiO_2 and p-Si. Therefore, the TiO_2 nanostructures will absorb the light and generate electron–hole pairs in the depletion region. The presence of an electric field in the depletion region by applied bias voltage ($V_{bias}> 1$ V) results in the separation of the charge carriers, where the holes will move to the p-side and the electrons will move to n-side. Thus, a photocurrent will be generated at the external contact[1].

Furthermore, TiO_2 is an n-type semiconductor. The surface oxygen defect (V_o)is predicted to have a significant function in the photodetection mechanism by TiO_2. Whereas, in dark state, oxygen molecules are adsorbed on the surface that separates free electrons from n-type TiO_2. This process produces a depletion layer with low conductivity near the surface of TiO_2.[2,3]

$O_2(g)+e^-\rightarrow O_2^-(ads)$ ………(8.4)

$O_2(g)+e^-\rightarrow O_2^{2-}(ads)$ ……….(8.5)

Upon illumination with light energy above or equal to energy gap of TiO_2, charge carrier pairs are created. The electric field produced in the depletion region moves the holes toward theTiO_2 surface, thereby leaving the electrons behind. Before the recombination between charge carrier pairs, the holes migrate to the surface and will recombine with electrons from the adsorbed oxygen ions (O_2^- or O_2^2), which leads to the release of oxygen atoms from the surface.[4,5]

$h\nu\rightarrow e^-+h^+$…………(8.6)

$O_2^-(ads) + h^+\rightarrow O_2(g)$………(8.7)

$O_2^{2-}(ads) +2\ h^+\rightarrow O_2(g)$……….(8.8)

This mechanism results in increased electron concentration in the material, which consequently increases conductivity. Therefore, the observed high photocurrent can be attributed to light-induced charge carrier generation at the depletion region ofTiO_2NRs, especially near the heterostructure interface. Furthermore, the large difference between can be attributed to the short transit time of charge carriers with long lifetime. The presence of oxygen caused hole trap states at the TiO2 surface which prevents the generation charge carrier pair (e^-–h^+) recombination and extends the lifetime of holes[6].

Sensitivity of the photodiode can be given as,

$S(\%) = \frac{I_{ph} - I_d}{I_d} * 100\%$............(8.9)

Using the formula in equation(8.9) variation of sensitivity can be plotted with NaCl concentration as shown. Figure 8.5 indicates that sample with 3M NaCl concentration has the highest sensitivity(~60%). Two circuit parameters namely responsivity(R), and external quantum efficiency(η), can be accounted for the sensitivity also.

Responsivity(R) can be given as,

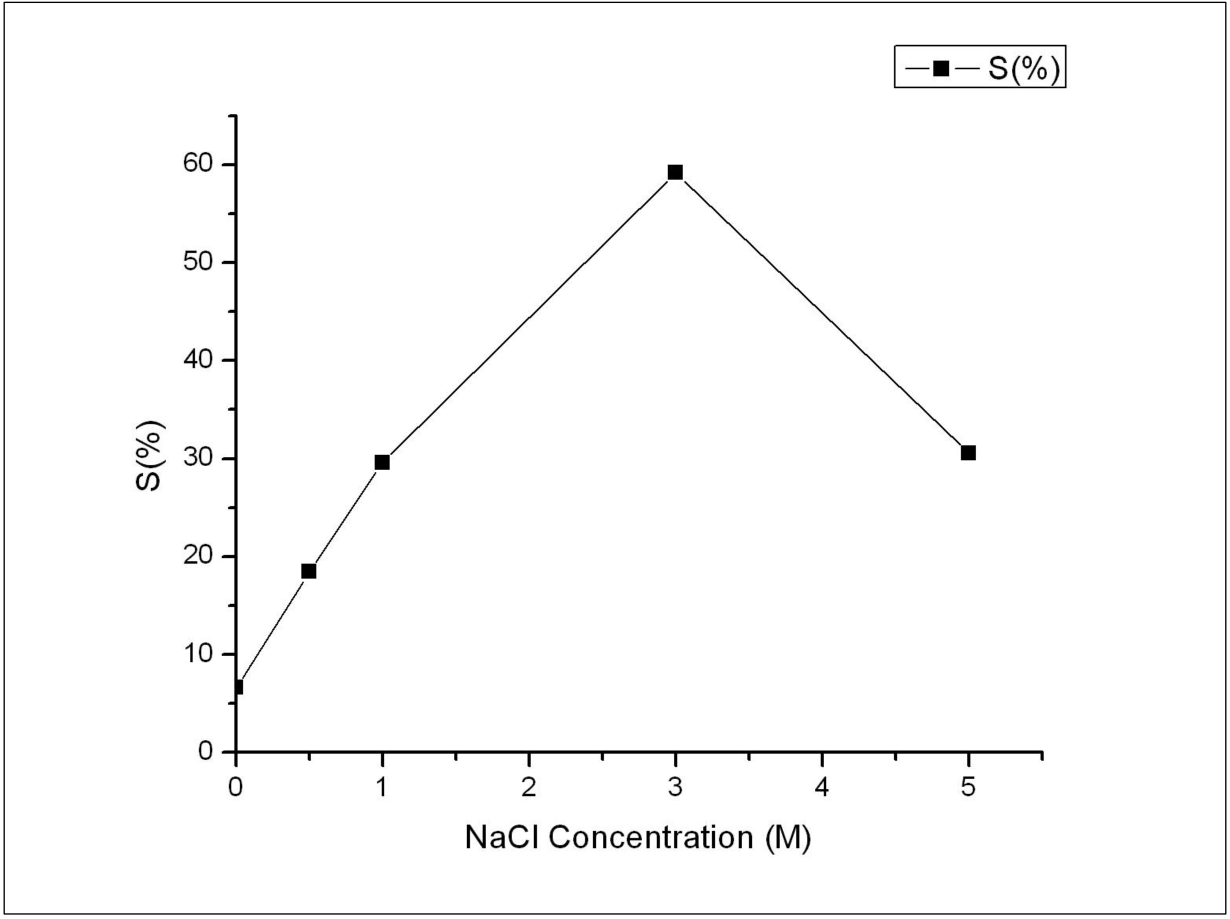

Figure 8.5: Variation of sensitivity with sample

$R = {}^{I_{ph}}\!/_{P_{inc}}$………(8.10),

where I_{ph}= Photocurrent in Ampere

P_{inc}= Input power in W

In our experiment input power was 100mWcm^{-2} of the solar simulator. Since the effective cell area was 1mm^{2}, hence net input power Pinc=100*10^{-5}W.

Internal quantum efficiency(η) can be given as,

$\eta = R * \frac{h\nu}{q}$ …….. (8.11)

So from equation(8.11) it is expected that variation of η, will follow variation of R.

Another important parameter of photodiode is current gain(g), which indicates enhancement of current under illumination, and can have significant importance for practical application.[7]

$g = \frac{I_{ph}}{I_d}$…………(8.12)

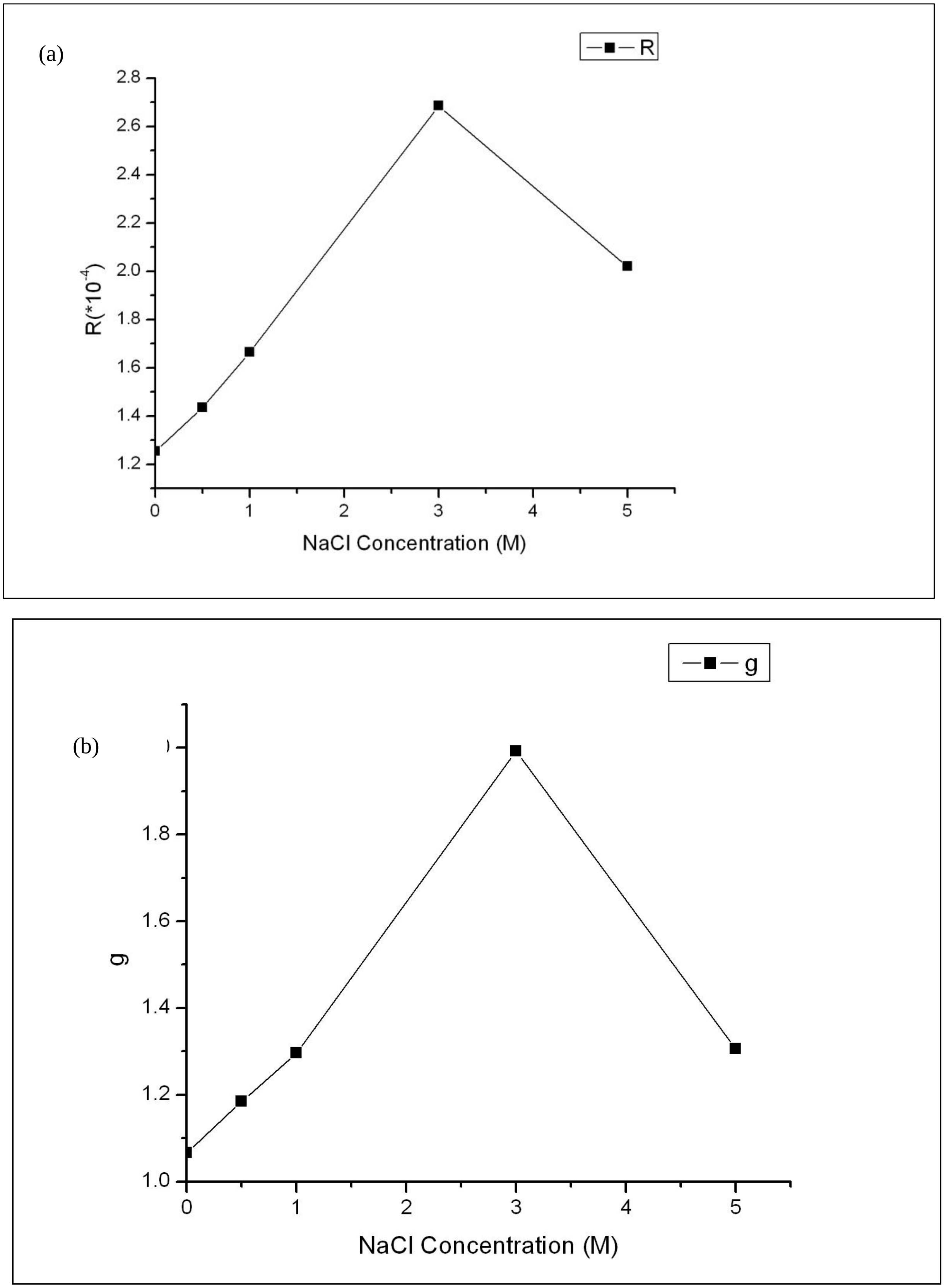

Figure 8.6: Variation of (a)responsivity and (b)gain with sample

From figure 8.6(b) it is clear that gain is maximum for S_{3M}, which was expected from the variation of sensitivity, responsivity and photodiode current.

From the above discussion it is clear that sample with 3M NaCl concentration showed best photodiode activity in terms of all the parameters, so it is anticipated to give a guideline for further utilization in practical domain.

Sample Code	Photodiode Current(*10^{-8}A)	Sensitivity (%)	Responsivity	Gain
S_{0M}	-0.76968	6.60054	1.25333	1.06601
$S_{0.5M}$	-2.22548	18.4278	1.43444	1.18428
S_{1M}	-3.79345	29.60023	1.66395	1.296
S_{3M}	-13.35919	59.1502	2.68476	1.9915
S_{5M}	4.7276	30.56095	2.0197	1.30561

Table 8.1: Parameters obtained from V-I characteristics of Photodiode

REFERENCES

1. B.E. Saleh, M.C. Teich, Semiconductor photon detectors, in: Fundamentals of Photonics, John Wiley & Sons, Inc., 1991.
2. N.K. Hassan, M.R. Hashim, N.K. Allam, Sens. Actuators A,2013, 192,124–129
3. N.H. Al-Hardan, M.J. Abdullah, N.M. Ahmed, F.K. Yam, A. Abdul Aziz, Superlat-tices Microstruct.,2012,51,765–771
4. N.K. Hassan, M.R. Hashim, N.K. Allam, Sens. Actuators A.,2013,192,124–129.]
5. N.H. Al-Hardan, M.J. Abdullah, N.M. Ahmed, F.K. Yam, A. Abdul Aziz, Superlat-tices Microstruct..,2012,51,765–771]
6. A.M.Selmana,Z.Hassana,M.Hushama,N.M.Ahmeda,Appl Surf Sci.,2014,305,445–452
7. V. Caratto, B. Aliakbarian, A.A. Casazza, L. Setti, C. Bernini, P. Perego, M. Ferretti,Mater. Res. Bull.,2013, 48 ,2095–2101.]

CHAPTER 9

CONCLUSION

From all the preceding chapters which gave an elaborate description of TiO_2 and its defect related studies and electronic applications, it can be concluded that variation of precursor gives rise to stunning properties. Its synthesis process that has been followed in this work is based on low temperature hydrothermal synthetic technique. Hence, the synthesis technique is environment friendly as no calcination is needed and as a result, it may find exceeding importance in the industries.

Firstly, hydrothermal synthesis is done with variation of NaCl precursor concentration, which gives rise to variation in product colour, which indicates its activity will be better on visible range. A detailed characterization is done in order to understand defect concentration and character. Well established hierarchical microstructure has been obtained. Moreover, effect of defect on lattice parameter has been investigated using Rietveld Refinement Technique. Lastly, photodiode has been fabricated and we tried to relate defect concentration and photodiode activity.

From defect related studies it is evident that sample with 3M NaCl concentration(S_{3M}) comprises of highest defect concentration. But from Rietveld refinement it has been observed that variation of lattice parameter is most for S_{1M} . Variation of lattice parameter is generated due to presence of internal strain inside the system, which may be governed by the presence of defect state. Defect state produces internal strain, which changes crystallite size. But as the presence of NaCl plays an important role in the formation of microstructure, it can be anticipated that at 3M NaCl concentration, formation of microstructures comprises of symmetric crystallite is more predominant, which even in the presence of large surface oxygen vacancy (Vo) is capable of retaining uniformity or structural symmetry of the crystallite.

From applications point of view, photodiode has application in optoelectronic and energy field. It is the fundamental structure of solar cell. With passing years, our energy consumption is increasing exponentially which can never be fulfilled with our present technology in hand. Si-based available solar cell is costly and have a very poor conversion efficiency. So here we have tried to fabricated photodiode, efficiency of which can be controlled by controlling defects into the system. Photodiode has a major application as a light sensor and here we were able to control sensitivity, responsivity just by varying precursor concentration, or in other words defect concentration. It has been found out that sample with maximum defect showed best photo response. Fabrication of such sensor using our technique is cost-effective and more efficient, as it needs much less time to fabricate than the conventionally available devices.

So, it can be concluded that by varying synthesis parameters defects can be incorporated into any material. Defects thus induced play a very prominent role to hint various properties of the material, and variation of defect concentration can have significant effect on optical, electronic or biological application.